INVESTIGATION OF PRESSURE DROP, ACOUSTICS AND HEAT TRANSFER IN CORRUGATED PIPES
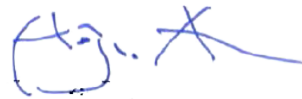
by
Ahmet Çağrı Develi

Submitted to Graduate School of Natural and Applied Sciences
in Partial Fulfillment of the Requirements
for the Degree of Master of Science in
Mechanical Engineering

Yeditepe University
2015

INVESTIGATION OF PRESSURE DROP, ACOUSTICS AND HEAT TRANSFER IN
CORRUGATED PIPES

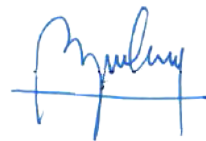APPROVED BY:

Assoc. Prof. Dr. Hojin AHN   ……………………………………
(Thesis Supervisor)

Assoc. Prof. Dr. Esra SORGÜVEN   ……………………………………

Assist. Prof. Dr. Barış YILMAZ   ……………………………………

DATE OF APPROVAL: ..../..../2015

ACKNOWLEDGEMENTS

ABSTRACT

INVESTIGATION OF PRESSURE DROP, ACOUSTICS AND HEAT TRANSFER IN CORRUGATED PIPES

Frictional loss and acoustics of air flow in stainless-steel corrugated pipes have been experimentally investigated. The diameters of corrugated pipes were 20.4, 24.5, 34.5 and 40.1 mm. Flowrates were obtained by measuring pressure drop across orifices.

Based on the behavior of the Darcy friction factor, the critical Reynolds numbers of the corrugated pipes at which flow changes from laminar to transition region are found to be 1500 to 1700, depending on the pipe diameters and corrugation sizes. Turbulent region begins at around Re = 2000 to 3000 for all corrugated pipes tested. For turbulent flow, in general, higher friction factors are observed for the larger ratio of the crest width to the pipe diameter. On the other hand, in laminar region the friction factor depends on only Reynolds number. The onset velocity is found to be independent of the pipe length. It transpires that the onset velocity corresponds to the Reynolds numbers at which turbulent region begins. The Strouhal number is observed to be almost constant over the wide range of Reynolds number, and appears to be influenced, not by the pipe length, but by corrugation sizes. The peak-whistling Strouhal number is found to be decreasing as the ratio of the diameter to the crest width increases.

Another test setup is built to investigate convection in corrugated pipes which are 20.4 and 34.5 mm in diameter. The pipe is insulated and calibrated by measuring heat loss while no air is in and out from the pipe. Energy conservation is applied to derive the local mean temperature in the corrugated pipe.

The local Nusselt number values for crest and hollow surface seem to be almost same. Average Nusselt number values for two pipes with diameters of 20.4 and 34.5 mm are observed to be close to each other in regard to Reynolds number.

ÖZET

ONDULASYONLU BORULARDA BASINÇ DÜŞÜMÜ, AKUSTİK VE ISI TRANSFERİ ANALİZİ

Paslanmaz çeliklerdeki kayıpları ve havanın akustik yapısı 20.4 mm, 25.4 mm 34.5 mm ve 40.1 mm çaplı ondulasyonlu borularda deneysel olarak incelendi. Debi ise orifis plakasındaki basınç düşümü ölçülerek hesaplandı.

Darcy sürtünme katsayı davranışı baz alınarak akışın laminardan ara geçiş bölgeye geçişi 1500 ile 1700 arasında gerçekleştiği ve ondulasyon ölçülerine bağlı olarak da değiştiği görüldü. Bütün test edilen borularda türbülanslı bölge ise 2000 ile 3000 arasında başlıyor. Türbülanslı bölge için tümsek yüzey genişliğin boru çapı oranı büyüdükçe sürtünme katsayısı büyüyor ancak laminar bölgede sürtünme katsayısı direk olarak Reynolds sayısına bağlıdır. Onset hızı boru uzunluğundan bağımsızdır. Bu onset hızının türbülanslı bölgenin başladığı Reynolds sayısına denk geldiğini gösteriyor. Strouhal sayısı geniş Reynolds sayısı aralağında sabit olup boru uzunluğunda bağımsız ancak ondulasyon ölçülerinden etkilendiği görüldü. En yüksek ıslık Strouhal sayısı boru çapının tepe yüzey genişliğine oranı arttıkça düştüğü gözlendi.

Bir diğer test düzeneği ondulasyonlu 20.4 ve 34.5 mm çaplı borulardaki ısı taşınımı için kuruldu. Boru termal olarak yalıtıldı ve ısı kaybı kalibrasyon için boru içinden hava geçmiyorken ölçüldü. Enerji korunum denklemi boru içindeki local ortalama sıcaklıklığın türetilmesi ve belirlenmesi için kullanıldı.

Lokal Nusselt sayısının tepe ve çukur yüzeyler için aynı.olduğu görüldü. 20.4 ve 34.5 mm çaplı borular için ortalama Nusselt sayısı yaklaşık olarak birbirine yakın olduğu incelendi.

TABLE OF CONTENTS

LIST OF FIGURES

LIST OF TABLES

LIST OF SYMBOLS AND ABBREVIATIONS

A_o	Area of orifice hole
$A_{p,cs}$	Cross section area of the corrugated pipe
C_d	Discharge coefficient of the orifice plate
C_{eff}	Effective speed of sound of air through the corrugated pipe
C_0	Speed of sound of free air
C_p	Heat capacity of air
d	Inner diameter of the orifice plate
D	Outer diameter of the orifice plate
D_i	Inner diameter of the corrugated pipe
D_o	Outer diameter of the corrugated pipe
D_p	Pipe diameter
f	Friction factor
F	Vortex shedding frequency
H	Cavity height of the corrugated pipe
h	Convective heat transfer coefficient
I_{avg}	Average of pressure sensor current output during the air flowing through the pipe
I_0	Average of pressure sensor current output while no air flowing through the pipe
I_{max}	Maximum pressure sensor current output
I_{min}	Minimum of pressure sensor current output
k	Conductive heat transfer coefficient, Heat capacity ratio
L	Pipe length
L_c	Characteristic length
m	Mass flow rate
Ma	Mach number
n	Acoustic mode
Nu	Nusselt number
P	Pressure (Pa or dB)

P_{supply}	Heat power supplied to corrugated pipe
P_{loss}	Heat loss power heat from the corrugated pipe
Pr	Prandtl number
P_t	Pitch length of the corrugated pipe
R	Electrical resistance of the corrugated pipe
Re	Reynolds number
St	Strouhal number
St_{pw}	Peak whistling Strouhal number
t	Thickness of corrugated pipe sheet metal
T_s	Surface temperature of the corrugated pipe
T_m	Air mean temperature in the corrugated pipe
T_∞	Air temperature at the infinite
U_∞	Air flow velocity
$\dot{V}$	Volumetric flow rate
V_{rms}	Root mean square voltage
w_N	N[th] root of unity
W_c	Crest width of the corrugated pipe
W_h	Hollow width of the corrugated pipe
x	Position of the thermocouple readings
β	The ratio of the orifice inner diameter to outer diameter
δ	Heat flux (heat load or loss per square area)
ΔP	Pressure drop
ε	Roughness height
ε^*	Roughness factor
λ	Wave length of air column
μ	Dynamic viscosity of air
ρ	Density of air
φ	Severity index
DAQ	Data acquisition

1. INTRODUCTION

Pipes with corrugations (Figure 1.1) considerably make the structure stronger as well as flexible. This unique design of characteristic structure lets the corrugated pipes available for many industrial uses. The vast majority of applications benefit from these pipes such as, vacuum cleaners, offshore natural gas production and so on. Turbulence induced by corrugated walls enhances heat transfer rate from the pipe but also yields the undesirable result of increase in pressure loss. Having said that though, at some critical conditions, the flow through the corrugated pipes lead to vibration and whistling which do not happen in the smooth ones and also affects the heat transfer rate along the pipe because of the flow behaviour inside. However, as a drawback, the noise associated with the vibration are energy losses and may cause mechanical failure for instance, fatigue in the life span dependent on what it is made of. Therefore, in order to design the desired corrugated pipes it is of the paramount importance to focus on the effect of the dimension parameter and shaped design of corrugations for enhancing flow structure to reduce energy losses due to vibrations and noise. Thus the use of corrugated pipes calls for detailed study of

(1) Characteristics of pressure loss,
(2) How to prevent possible mechanical failure due to the vibration
(3) How to reduce noise caused by the whistling.

Figure 1.1 Stainless Steel Corrugated Pipes

1.1. CHARACTERISTIC OF CORRUGATED PIPES

The whistling at corrugated pipes is an outcome caused by local vortex sheddings in the cavities and acoustic waves which travel along the pipe. The instability of the shear layer, which is the source of unsteadiness, separates the bulk flow from the rotating flow in the cavities acting as an amplifier transferring energy from the bulk flow to acoustic waves. This unsteady flow brings about an unsteady reaction by fluctuating through pipe wall which is a course of action for hydrodynamic force as well as source of sound. The vortex shedding frequency of the pipe leads to the acoustic natural frequency of the pipe, fluctuation at the structure, vibrations on the pipe and standing acoustical waves known as lock-in frequency referred to the onset velocity. The acoustic oscillations can be defined by the ratio of bulk velocity in the pipe across the cavity width at the upstream edge and oscillation frequency of acoustic field corresponding to the Strouhal number.

$$St = \frac{FL_c}{U_\infty} \tag{1.1}$$

Where f is the oscillation frequency and U is the flow velocity in the pipe. The characteristic length is taken as the width of upstream edge where the flow separation occurs as the oscillation characterizes the vortex shedding depending on the application, dimensions of the corrugation of the pipe can vary and it is well known that these parameters have a gradual effect on the whistling.

1.2. OVERVIEW OF THE LITERATURE

1.2.1. Pressure Loss in Corrugated Pipes

Losses in corrugated pipes are cause for concern for a whole host of researches. Major loss tends to be larger than smooth ones. The corrugations can be treated as roughness and dimension of the corrugations play a significant role on pressure loss. However, the region boundaries namely, laminar, transient and turbulent are different from common pipes. Accordingly, the dimensions of the corrugated pipes have a great influence on those region boundaries in terms of Reynolds number. Due to distinct velocity profile of corrugated

pipes, even it varies for each pipe with different dimensions, friction factor is higher than usual pipes and flow characteristic aspects vary with the acoustical effects involved.

The corrugated pipes with square wave [1-4] and sinusoidal wave [5-8] (d-type and k-type) geometry type of corrugations are commonly studied. Kruse et al. [1] introduced wavelength and wave amplitude of a water channel varies with changing corrugation dimensions. Nakagawa et al. [2] came up with findings of major contributions to Reynolds stresses contained in velocity structure appearing intermittently have large effects on the core flow. Breuer et al. [3] experimented on the turbulent flow for a large range of Reynolds number. They emphasized that the flow is two dimensional and steady at Re=100 based on height of the hills but, the flow changes and become three dimensional and chaotic Reynolds number above 200. Hudson et al. [4] observed turbulence production in a rectangular water channel with lower corrugated wall. They witnessed the turbulence production was mostly related to the shear layer separated from the back of the corrugation. Perry et al. [5] classified corrugated pipes in two namely, d-type and k-type. The former defines corrugated pipes with a surface of roughly square cavities and the latter defines corrugated pipes having a surface with grooves with a cavity length to height ratio higher than around 4. Djenidi et al. [6] witnessed strong momentum interactions between the core flow and the fluid inside the grooves for d-type rough wall. Jimenez et al. [7] proposed even if the vortexes in the cavities are stable; the roughness length scale of the flow would vary in terms of the cavity width and the pitch length.

The width of the cavity (W_{hollow}) has to do with how easily the vortex inside the cavity is ejected from the cavity to the bulk. Thus, corrugated pipes with groove length larger than the height should have higher pressure drop. Ejection of fluid to core flow represents enhancements of momentum transfer from the groove to the main flow. Stel at al. [8] studied pressure loss numerically in the corrugated pipes with different groove height and lengths. He suggests the vortex is less stable for higher Reynolds numbers due to consequence of vortex intensity in the cavity. A perturbation mechanism is introduced to define the intensified circulation in the cavity lets the fluid leave the cavity to the core flow which is an occasion recognised as momentum transfer between the groove and the main flow relate to increase in Reynolds number. He witnessed the groove length has a great effect on the friction factor due to enhancement in momentum transfer and increasing

Reynolds shear stress and turbulent intensity. Enhancement in momentum transfer as suggested should stem from changing of the acoustic mode. Together with the other aspects mentioned by Stel et al. [8] should explain why Strouhal number varies with different groove lengths, heights or crest lengths even for same shapes of corrugations.

Stel et al. [8] strengthen the research on corrugated pipes with experiments on d-type ones. They suggested that the friction factor increases as the groove length increases regardless of groove height. They mentioned the laminar flow as where friction factor values are close to ones for smooth pipes. However, there is no critical value signified for this. Furthermore they came up with the friction factor is higher for corrugated pipes than for smooth ones and increases as Reynolds number or cavity length elevates but cavity height has no influence. Their results also predict there is a strong interaction between fluid and the downstream corner of the cavity where momentum exchange between main flow and the groove is determined due to increase in the turbulent intensity near the corrugations.

Unal et al. [9-10] studied a corrugated pipe channel and conducted on their experiments with PIV analysis to pinpoint critical Reynolds number in terms of vortex structure in the cavities from laminar to turbulent region. They found the transition from laminar to turbulence at Reynolds number around 1500. Below that, the flow is laminar where vortexes inside the grooves are stable as well as steady and two dimensional and do not interfere the core flow. Moreover, flow is chaotic Re>2000 where vortexes in the cavities turned out to be unstable and burst to core flow intermittently.

Ahn et al. [11] investigated the characteristic of pressure drop for both straight and helically configured corrugated pipes. The friction factor is examined and found to be almost constant over a range of Reynolds number 4000 to 80000 which is identified as fully turbulent region.

Vicente et al. [12] reported the friction factor in asymmetrically corrugated pipes with various diameters from laminar to turbulent region. They proved in their results that friction factor values are higher for corrugated pipes with 5-25 % than for smooth ones. Moreover, they witnessed the cavity height to pipe diameter ratio (H/D) boosts the transition Reynolds number value from laminar to turbulent region. They also proceeded their experiments with heat transfer tests. They observed mixed convection and suggested

Nusselt number increases abruptly as Reynolds number increases when the flow is turbulent

Pressure flows are classified by instabilities caused by shear stresses. Nyarko et al [13] observed a relation between heat load and friction factor. He mentioned Reynolds number below 2000 is the transition from laminar to turbulent region. This range is where the momentum of the free stream flow beats the momentum of the fluid at cavity in the low pressure zone and makes the fluid circulate. However, he did not specify an exact location of the transition. The model with crest and trough is based on dealing with instabilities due to upward flow. He addressed this upward flow occur because of the negative pressure gradient overcoming shear stress caused by viscous forces. Furthermore, he witnessed for turbulent region a high dominating pressure zone to left on the crest and low pressure zone to the right on the crest determining force exerted by the wall to slow down the flow.

As per our results, these interactions between the core flow and circulating fluid are related for corrugated pipes in which cavity height to pipe diameter ratio differs and how lock-in frequency affects or is affected. Yet, this ratio must be related to variation friction factor for corrugated pipes with different diameters because this ratio can be treated roughness factor. As Reynolds number increases, the fluid will be ejected from the cavity more frequently that would boost increase in Reynolds shear stresses. As a consequence, the pressure loss will be higher thus friction factor recover its increase.

1.2.2. Acoustics in Corrugated Pipes

There are several experiments in the literature proceeded with air or water. Despite these numerous literature for many instances, all too many experiments are carried on short corrugated pipes with smooth segments. (Popescu et al., [14], Rudenko et al. [18], Nabikoglu et al. [13-14] and Debut et al. [19]). Only Nabikoglu et al. [15-16] and Debut et al. [19] mentioned fully corrugated pipe suggesting that acoustic losses are small compared to viscous losses.

The fluid flow in a corrugated pipe brings about acoustic pressure waves which interact with vortex shedding producing distinct noise and vibration. Popescu et al. [14] studied

bursting vortex line that travels along the pipe. They explained this as how acoustic waves and the noise happen but if the vortex is not strong, a wide acoustic field can not get in motion which supress whistling which is found to start at around 3.8 m/s. They also claim acoustic flow field sways the vortices convecting downstream. Furthermore, aerodynamic and acoustic flow fields are in an interaction leading energy transferring from the former to latter. The acoustic frequency affects the shear layer frequency and conforms to each other. Lock-in frequency appears as only one dominant frequency for a range of flow velocity when acoustic waves adapt to shear layer. Therefore, the shear layer instability elevates with the flow velocity.

Nakiboglu et al. [15] came up with cavity height to width ratio and investigated how the ratio influences the peak whistling Strouhal number, which is the value where the pressure amplitude is at maximum within the same resonant mode, and the fluctuating amplitude. They defined the flow oscillation mechanism with a feedback produced by the velocity fluctuations which stem from the coupling of the vortex sheds in an acoustic mode. In this loop, the shear layer instability over the cavity mouth and acoustic modes of the pipe can be regarded as the amplifier and the filter respectively. This is why the whistling brings about. They suggest the peak whistling Strouhal number is almost stable independent of the depth and fluctuation amplitude for deep cavities due to vortex at the bottom of the cavity being less effective. However for H/W<0.5, Strouhal number and fluctuation amplitude increase as the cavity gets deeper.

Nakiboglu et al. [16] came up with a ratio named confinement ratio (cavity height to width ratio) which is actually mentioned by Elliot et al. [17] at the first place. They studied this ratio for its influence to Strouhal number. They explained the whistling mechanism as a source of unsteadiness and caused by flow separation at the upstream edge of each groove generating a shear layer. Moreover, they also refer to Elliot et al. [17] for shear layer instability as a hydrodynamic subsystem. Longitudinal standing waves are the acoustic subsystem and synchronize in the system. That is why the whistling frequency increases stepwise at a specific flow velocity. They observed the Strouhal number regarding the sum of the cavity width and cavity upstream edge radius is not dependent on the pipe length. The peak whistling Strouhal number drops when the confinement ratio rises which is a situation explained with a change in velocity profile due to variation of confinement ratio.

As acoustic waves travel along the corrugated pipe, the fluctuation amplitude can escalate or deteriorate. Rudenko et al. [18] observed the source amplitude is proportional to the local amplitude of the flow velocity oscillation. As the amplitude rises, fluctuation of the shear layer ends up with the formation of vortices which is a nonlinear saturation mechanism. When the flow comes across this nonlinearity, a constant whistling occurs. They investigated further the fluctuation begins above a critical Mach number which corresponds to the flow velocity at 6.8 m/s. This critical velocity is inversely proportional to corrugated pipe length.

Debut et al. [19] examined the nature of aero-acoustic interaction in corrugated pipes. They suggest sharpness of corrugations should be taken into account when investigating the onset of instability. They recommend a dimensionless analysis of these kinds of data collected and flow visualization analysis that would be in a great help to understand the phenomena of sound generation process. Yet, they found Strouhal number based on pitch length is ranging from 0.4 to 0.5 for all corrugated pipes tested. Moreover, they introduced the mechanism with an acoustic feedback supressing the perturbation. The hydrodynamic oscillations based on corrugations decay to brand-noise turbulence below the critical minimum velocity. This minimum velocity corresponds to onset velocity which is determined around 5 m/s for all pipes. They also reported the fluctuation amplitude comes down to the pipe length as longer pipe being noisier for identical corrugations and pipe diameter but the frequency remains to be same for the identical values of flow velocities. They implied the Strouhal number is independent from the pipe length but they claimed that the lock in velocity ranges is wider for the shorter pipes.

As per our experimental results, the peak whistling Strouhal number is almost constant in terms of Reynolds number. However, as Reynolds number gets higher of the critical one, a leap in Strouhal number is witnessed and the acoustic mode shifts to the next. Hence, in the same acoustic mode, Strouhal number begins to fall slightly until the resonant mode changes. In the meantime, fluctuation amplitude rises till it reaches its peak which corresponds to the peak whistling frequency and Strouhal number and then drops. The amplitude behaves the same within every each acoustic mode. As mentioned above, there is an interaction between aerodynamic and acoustic flows. The energy is supplied from the former to later and as a consequence, the acoustic frequency sways the shear layer

frequency and makes the shear layer surface adapt to itself which allows the vortex at the cavity mouth bursts to core flow. During the fluid flowing through the corrugated pipe steadily, all harmonics of an acoustic natural frequency exists. Due to presence of multiple acoustic frequencies, the vortex shedding frequency locks into one of them in regard to flow velocity. The acoustic pressure pulsation amplitude hits the maximum at the velocity at which the vortex shedding frequency complies with an acoustic mode. The lock-in frequency range and fluctuation amplitude during the lock-in phase come down to the pipe length the corrugation size.

1.3. PROBLEM DEFINITION

Up to now, researches on corrugated pipes or side branches are conducted with various methods and techniques of measurements. What is not completely tested is the fully corrugated pipe with very high in length. Regarding the experiments searched the major issues stem from test set-up designs; for instance, driving flow instead of sucking sways the flow at the entrance in the settling chamber or not fully developed flow due to the pipe lacking in length or determining the characteristic length in as much as different characteristic lengths are considered for Strouhal number.

The vital issue for corrugated pipes is the oscillations causing whistling at high amplitudes. In addition, these high amplitude of sounds can bring about structural vibrations resulting in all too many mechanical failures.

In the scope of the study, severe parameters such as Darcy's friction factor, characteristic regions of the flow, acoustic and hydrodynamic characteristics of flow are to be investigated to observe the effects on the whistling phenomena defined by the peak whistling Strouhal number.

2. THEORITICAL BACKGROUND

2.1. STANDING ACOUSTIC WAVES FOR OPEN END AIR COLOUMN

Pipes are an open end air column as two ends are uncovered. The waves created by instability of the shear layer at the corrugation reach the outlet of the tube vibrate along the pipe. The wave lengths (λ) are determined by the hydrodynamic mode which is also called the harmonics of the pipe (n). The wave frequency is determined as follows (Elliot et al. [17]);

$$F_n = \frac{nC_0(1 - Ma^2)}{2L} \qquad \text{n=1,2,3 ...} \qquad (2.1)$$

where n is the acoustic mode of the wave, L is the pipe length, Ma is the Mach number and C_0 is the speed of the sound in the air which is around about 340 m/s.

Therefore, the hydrodynamic mode of the pipe can be calculated if the whistling frequency is measured experimentally. The hydrodynamic mode defines how many nodes and antinodes the sound wave has and the level of fluctuating sound wave thus, the wave length is;

$$\lambda = \frac{2L}{n} \qquad \text{n=1,2,3 ...} \qquad (2.2)$$

Theoretically, if the waves begin to oscillate in a regular pattern to comply with the hydrodynamic waves, the whistling occurs. Hence, the flow must be in turbulent region where the whistling starts due to no transition effects remain. This phenomenon can also be interpreted by investigating pressure loss regarding flow regions. We will come to that later in more detail.

Sine wave is the simplest model of sound for domain whose x axis is the time and y axis the pressure.

$$P = P_0 \sin(2\pi F t) \qquad\qquad \text{n=1,2,3 ...} \qquad\qquad (2.3)$$

Where

P: pressure, in Decibel (dB) or Pascal (Pa)

F: frequency, in Hertz (Hz)

P_o: amplitude (height of the wave) or volume, in Decibel (dB) or Pascal (Pa)

t: time, in seconds

T: period which is the duration of a wave, in seconds. (T=1/f)

Generally, sound has two characteristics namely, wave length and power of the sound. Wave length corresponds to the frequency of the wave. High notes have high frequencies, thus the pressure varies quickly. Frequencies are introduced with the unit named Hertz (Hz) which is the number of waves per second. Power of loudness corresponds to the amplitude of the pressure. Even, these pressure oscillations can be felt by body in an area with very loud sound. Pressure is generally introduced in Pascal (Pa= 1 N/m2). Decibel Scale is a logarithmic pressure scale where we can distinguish the sound whether it is quiet and loud. Unit of Pascal (Pa) can be converted to Decibel (dB) as it follows;

$$P_{dB} = 20 log \frac{P_{Pa}}{2 \times 10^{-5}} \qquad\qquad (2.4)$$

The constant 2×10^{-5} Pa is considered to be the hearing threshold which is where P_{dB} is zero due to the fact that when $P_{Pa} = 2\times10^{-5}$ Pa, $P_{dB} = 20 \times \log 1 = 0$.

The wavelength of the standing wave for any given harmonic is related to the length of coloumn. If the length of column is known, the wave length related to each of the mode and frequencies can be determined. Hence, the column length and wave length relationships and the wave equation ($C_0 = f \times \lambda$) are combined to perform calculations to predict the length of column required to produce a given natural frequency. In contrast, calculations can be performed to predict the natural frequencies produced by a known length of string. Knowing the speed of a wave in a string is required for each of these calculations. The graphic below displays the relations between crucial values for those calculations. These equations are useful for such problems related to standing waves.

First Harmonic   Second Harmonic   Third Harmonic

$L=\lambda *1/2$ $L=\lambda *2/2$ $L=\lambda *3/2$

$\lambda=2*L$ $\lambda =L$ $\lambda =2*L/3$
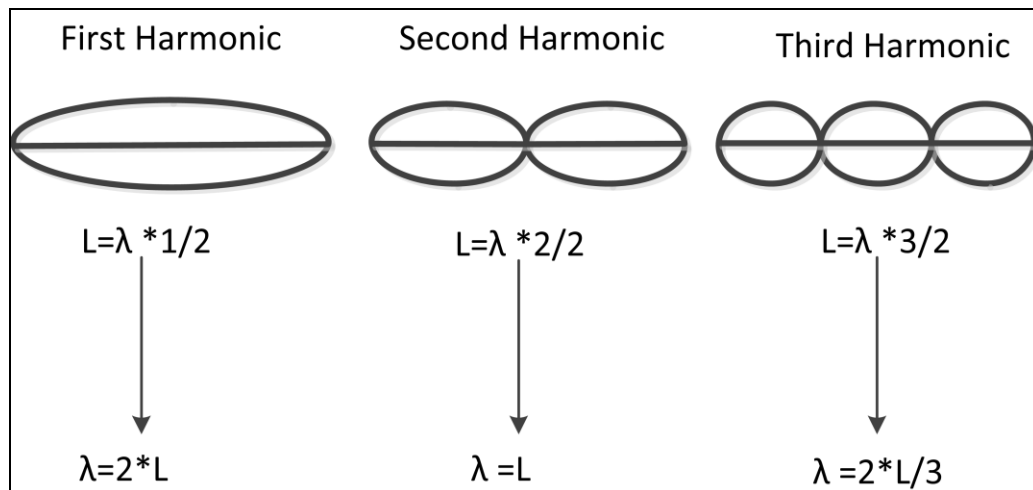
Figure 2.1. Schematic relation between wavelength and harmonics of sound wave

Many instruments consist of an air column enclosed inside of a hollow metal tube. However, if the end of the tube is open such as the air at the end of the tube freely vibrates when the sound wave reaches there. If both ends of the tube are not covered, the instruments are told to contain an open-end air column. Various instruments work based on open-end air columns.

An instrument has a set of fundamental frequencies and their harmonics where it oscillates at when a perturbation exists. These harmonics are associated with a standing wave pattern. A standing wave pattern was introduced as a fluctuating pattern when the frequency of the source is the reason of reflected waves from one end to interfere with incident waves from the source. If a sound wave is traveling along a circular tube, eventually it comes to the end of the tube which represents a boundary between the air in the tube and the expanse of air outside of the tube. For open-end air columns, the standing wave pattern which results in the interference of wave interfering with an incident wave.

The high-pressure and low-pressure regions of a sound wave interfere to produce a standing wave pattern. The high-pressure reflects as a compression. The reflection occurs for the exact moment where a rarefaction (low-pressure regions) is interpreted into the end of the tube. Since one-half of a wave comprises of a compression and a rarefaction, there is one-half of a wave in the tube. Rarefaction will consequently interfere with the compression in the center of the tube. The interference of a high pressure region and a low pressure region lead to normal pressure region. Thus, one-half of a wave is defined in the

open-end air column where a standing wave will be established in the tube. The pressure at the open ends of an open-end air column always fluctuates between a high pressure and a low pressure.

As already been mentioned, an instrument has a set of natural frequencies where it vibrates at when there is a disturbance introduced. These natural frequencies are known as the harmonics of the instrument associated with a standing wave pattern. Standing wave pattern was introduced as a vibrational pattern present when the oscillation frequency of the source brings about response waves from one end to influence incident waves from the source in as much as specific points along the wave seem to be fixed. In such case discussed earlier, wave patterns were drawn to demonstrate the amount of motion of the column at diversity of locations along its length. Such patterns indicate nodes or points of no displacement at the two fixed ends of the column. For closed end air columns, air is not free to perform motion. In stark contrast, air is free to move back and forth at longitudinal direction for the open end of an air column such that, the standing wave patterns illustrate antinodes for the open ends of air columns case.

Thus, based on the standing wave patterns for air columns, fluctuation antinodes exist at any open end and vibrational nodes are present at any closed end. If this principle is implemented to open end air columns so the pattern for the fundamental frequency have antinodes at the two open ends and a single node. Therefore, the standing wave pattern for the first harmonic for an open-end air column is illustrated in Figure 2.2.
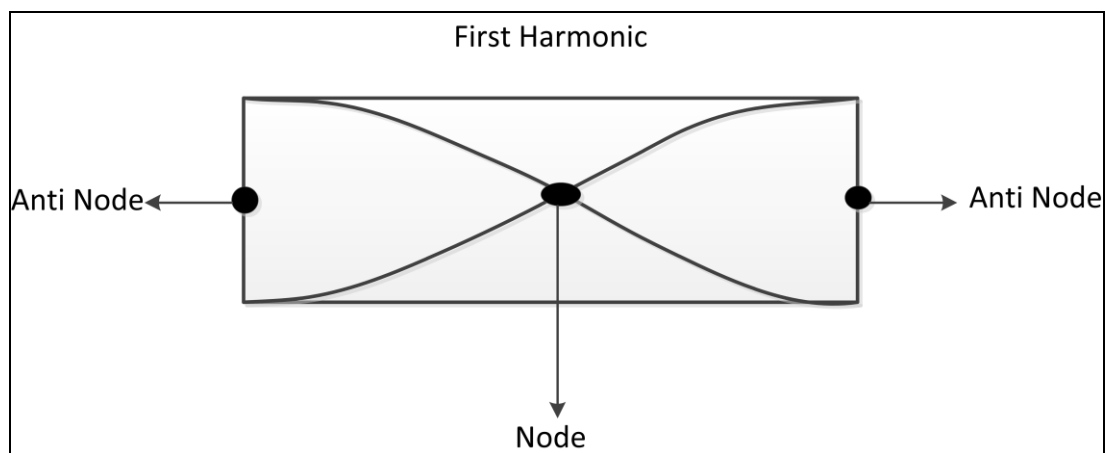
Figure 2.2. The first harmonic: one node and two antinodes

The distance between antinodes on a standing wave corresponds to one-half of a wavelength. As can be seen in the diagram above, both antinodes are positioned at the two ends of the air column. Hence, the length of the air column is equal to one-half of the wavelength for the first harmonic which is equivalent to fundamental frequency.

The standing wave for the second harmonic of an open end air column can be obtained if another antinode and node is put in the pattern. This leads to three antinodes and two nodes. This pattern is displayed in the diagram below. We can observe in the pattern that there is a full wave in the length of the air column. The full wave is twice larger in the number of waves which were in the first harmonic. Thus, the frequency of the second harmonic is twice larger than the fundamental frequency.
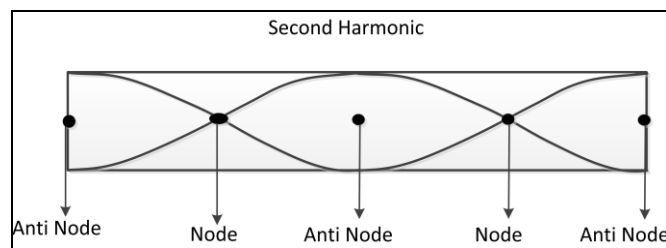
Figure 2.3. The second harmonic: two nodes and three antinodes

The standing wave pattern for the third harmonic of an open end air column exists if another antinode and node were in the pattern. This results in four antinodes and three nodes. This pattern is depicted in the schema below. As witnessed in the pattern, there are one and one-half wave in the length of the air column. One and one-half wave is three times larger than the one presented in the first harmonic. Hence, the frequency of the third harmonic is three times larger than the frequency of the first harmonic.
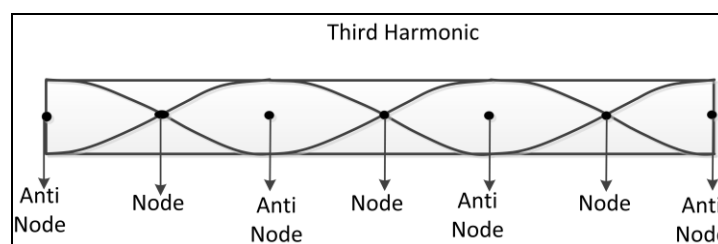
Figure 2.4. The third harmonic: three nodes and four antinodes

According to the process of adding another antinode and node to each harmonic to define the pattern and the corresponding relation of length and wavelength can be progressed. Thus, it is paramount importance to maintain antinodes on the open ends of the air column so, the results are consistent with values in the table below. The relation between the standing wave regulation for a given harmonic and the length to wavelength relation for open end air columns are presented in the table below.

Table 2.1. Classification of waves in an air column

Number Of Harmonics	Number of Waves	Number of Nodes	Number of Antinodes	Length & Wavelength
1	1/2	1	2	$\lambda = (2/1)*L$
2	1	2	3	$\lambda = (2/2)*L$
3	3/2	3	4	$\lambda = (2/3)*L$
4	2	4	5	$\lambda = (2/4)*L$
5	5/2	5	6	$\lambda = (2/5)*L$

The flow chart of mathematical relations for open end air columns is used in order to perform calculations estimating the length of air column needed to introduce a natural frequency. In contrast, calculations are done to estimate the fundamental frequency and its harmonics by knowing length of air column. Each calculation needs to be known the speed of a wave in air that is roughly 340 m/s at room temperatures. The graphic below (Figure 2.5) displays the relation between the critical variables in those calculations. These relationships are utilized to support problems for the solution involving standing waves in instruments. [20]
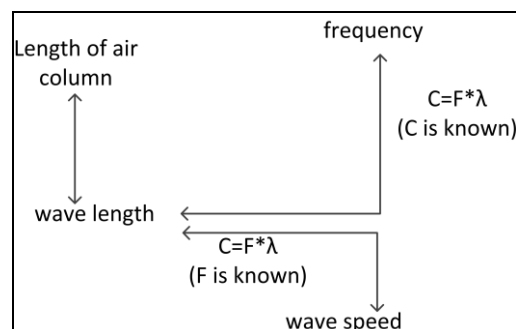
Figure 2.5. Problem solving scheme

The speed of sound (or the sonic speed) is an important parameter which is the speed where low pressure wave travels through a tube. Disturbance is the reason of the pressure wave creating a gradual increase in local pressure. In order to introduce a relation for the speed of sound, there are a great diversity of analyses or experiments to investigate speed of wave. The speed of sound can be determined for the fluid is an ideal gas as follows;

$$C_0 = \sqrt{kRT} \tag{2.5}$$

where k is the specific heat ratio, R is the gas constant and T is the free stream air temperature.

The second vital parameter is the Mach number (Ma) which is the ratio of the actual velocity to the speed of sound;

$$Ma = \frac{U_\infty}{C_0} \tag{2.6}$$

Fluid flow regimes are described in regard to Mach number. The flow is named sonic when Ma = 1, subsonic if Ma < 1, supersonic if Ma > 1, hypersonic when Ma >> 1, and transonic if Ma $\cong$ 1. In the experiments of this, flow regime is subsonic where Mach number is less than 1. [20]

2.2. VISCOUS FLOW IN PIPES

There are representative ranges varying with flow geometry, surface roughness and the level of fluctuations. The vast majority of analyses are related to laminar flow and turbulent flow.

1 < Re < 100 : Laminar, strong Reynolds number dependence
100 < Re < 1000 : Laminar, boundary layer theory useful
1000 < Re < 10000 : Transition to turbulence
10000 < Re < 10^6: Turbulent to moderate Reynolds number dependence

Firstly, Hagen (1839) reported in his experiments that the pressure drop varies linearly with the flow velocity up to roughly 1.1 ft/s (0.33 m/s) where there is instant change. Above the velocity of 2.2 ft/s (0.67 m/s), the pressure loss is nearly in quadratic form. Later Osborne Reynolds (1883) explained this in dependence of fluid properties such as, density and viscosity with the dimension of the enclosure where fluid flows through and the velocity of the flow. He came up with a dimensionless number now we call it as Reynolds number. If we examine Hagen's results in Reynolds' relation, it is found out that up to $Re_d = 2100$ (v=1.1 ft/s) inertial forces are weaker than viscous force and the flow is unstable. The flow becomes fully turbulent at $Re_d = 4200$ (2.2 ft/s). Having said though, these critical numbers for both laminar and turbulence region are not strict in as much as the inertial forces begin to deviate the viscous forces, a transition effects can be witnessed from $Re_d = 1000$ to $Re_d = 2300$. This is proved in the dye experiment, after $Re_d = 1000$, rare small fluctuations (puffs) were observed. According to Moody Chart, there is still dependence of viscous effects observed between $Re_d = 4000$ and $Re_d = 10000$. However, this influence reduces after Re=10000 which is called fully turbulent region.

Another way to distinguish, laminar transition and turbulent region are proposed by Hagen displaying pressure drop with respect to mean flow velocity. In the laminar region, pressure drop changes linearly but it changes nearly in quadratic form in turbulent region. No relation between pressure loss and mean flow velocity for transition region can be suggested but a power fit is applied to trend for turbulent region where n is told to be between 1.7 and 2. (Figure 2.6)
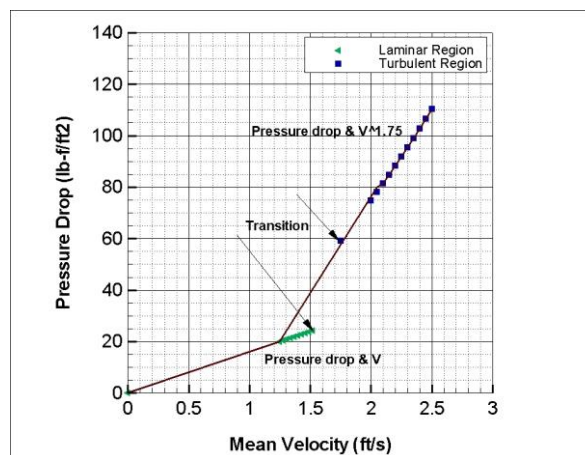
Figure 2.6. Pressure loss versus average flow velocity

The figure above demonstrates pressure loss and its relation with the mean flow velocity for a smooth pipe in turbulent region indicating n is not changing any more for fully turbulence. [21]

2.3. MOODY CHART AND FRICTION FACTOR

The main interest in the tests of pipe flow is the pressure drop directly associated with the power requirements of the fan or pump to maintain flow to be driven. Pressure drop due to viscous effects correspond to an irreversible energy loss. In practice, it is found safe to express pressure loss for all types of fully develop internal flows laminar or turbulent flows, circular or noncircular pipes, smooth or rough horizontal and inclined pipes as follows;

$$\Delta P = f \frac{L}{D_p} \frac{1}{2} \rho U_\infty{}^2 \tag{2.7}$$

where f is the Darcy's friction factor. L is length interval where the pressure loss is measured, D_p is the pipe diameter, ρ is the operating fluid density and U_∞ is the mean flow velocity through the pipe.

According to Moody Chart, for laminar flow the friction factor is a function Reynolds number only and independent from the roughness of the pipe surface.

$$f = \frac{64}{Re} \tag{2.8}$$

However, the friction factor depends on Reynolds number and the relative roughness (ε/D) which is the ratio of the height of the rough surface to the pipe diameter in turbulent region.

The functional form for this relation cannot be derived theoretically so all available equations in the literature were obtained from experiments by utilizing pipes with intentionally roughened surfaces (generally glued sand grains). Such experiments were mostly performed by Prandtl's student J. Nikuradse in. The friction factor was obtained

from the measurements of the volumetric flow rate and the pressure loss in the pipe. The experimental results measured are available in many forms namely, tabular, graphical, and functional forms derived by curve-fitting experimental data. Cyril F. Colebrook derived an equation for turbulent flow in 1939 by benefitting the available data for transition and turbulent flow in smooth as well as rough pipes as shown in the following relation known as the Colebrook equation (Equation 2.9);

$$\frac{1}{f} = -2\log\left(\frac{\varepsilon/D}{3.7} + \frac{2.51}{Re\sqrt{f}}\right) \tag{2.9}$$

An American engineer Hunter Rouse came up with a graphical plot which is for friction factor as a function of Reynolds number by verifying Colebrook's equation in 1942. Moreover, he suggested the laminar flow relation as well as a table of commercial pipe roughness. After two years, Lewis F. Moody reregulated Rouse's diagram into the form which is known as Moody Chart (Figure 2.7) and widely used today. It offers the Darcy friction factor as a function of the Reynolds number for pipe flow and e/D upon a large range. Although it is created for circular pipes, it can also be useful for noncircular pipes by manipulating the diameter by the hydraulic diameter.
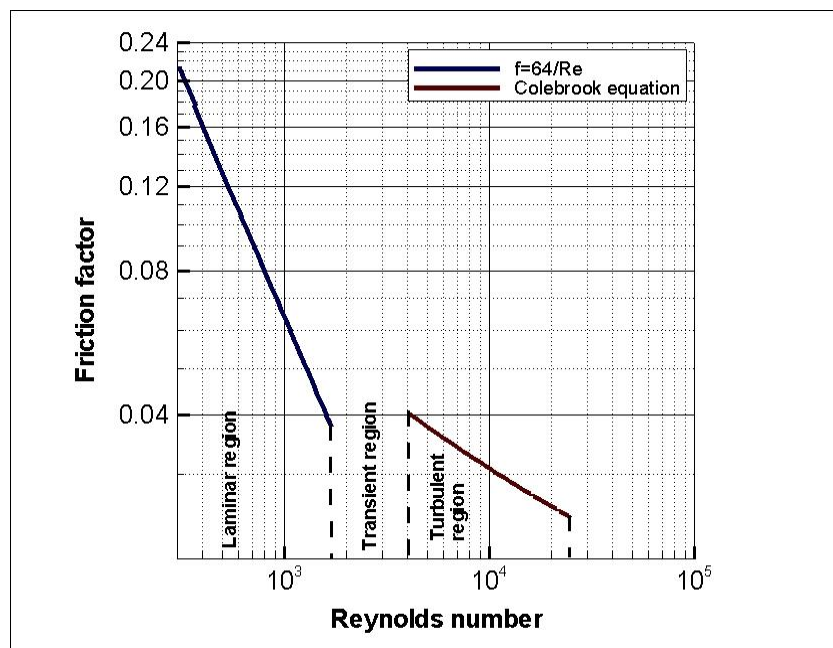
Figure 2.7. Moody Chart

In a nutshell, regarding all these well-known basics for pipe flow, it is expected to observe friction factor is inverse proportional to Reynolds number for corrugated pipe in laminar region and independence of Reynolds number at fully turbulent region as the corrugated pipe can be considered as a fully rough pipe. However, it is also expected to come across different critical Reynolds numbers for laminar region, transient region, turbulent region and fully turbulent region due to fact that the flow separations at the upstream edge of the corrugations lead to instability on shear layer causing chaotic flow in the corrugated pipe. [22]

2.4. ORIFICE DISCHARGE COEFFICIENT

Orifice plate is a planar plate with a hole generally integrated in a pipe. When there is flow through the orifice, the pressure escalates at upstream of the orifice. However, as the fluid is forced to pass through the hole, the velocity increases and the static pressure fall. The flow begins to expand at exit of the hole as a consequence velocity decreases thus, static pressure increases. Therefore, the flow rate can be determined by measuring the pressure difference in fluid across tapings of upstream and downstream of the plate. Bernoulli equation takes place in obtaining the flow rate by using coefficients established from various researches.
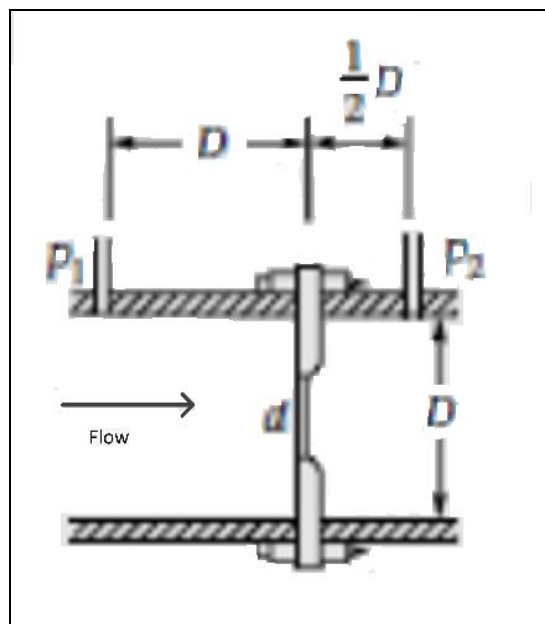
Figure 2.8. Schematic of flow through orifice plate

Mass balance;

$$\dot{V} = A_1 U_1 = A_2 U_2 \tag{2.10}$$

$$U_1 = \frac{A_2}{A_1} U_2 = \left(\frac{d}{D}\right)^2 U_2 \tag{2.11}$$

Bernoulli equation ($z_1=z_2$);

$$\frac{P_1}{\rho g} + \frac{U_1{}^2}{2g} = \frac{P_2}{\rho g} + \frac{U_2{}^2}{2g} \tag{2.12}$$

Combining Equation 2.11 and Equation 2.12;

Obstruction (with no loss);

$$U_2 = \sqrt{\frac{2(P_1 - P_2)}{\rho(1 - \beta^4)}} \tag{2.13}$$

where $\beta=d/D$ is the ratio of the converging duct diameter to total duct diameter. Once U_2 is known the flow rate can be obtained from Equation 2.10.

This basic analysis demonstrate that the flow rate through a pipe is easily obtained from the Equation 2.10 and Equation 2.13 combined by measuring the pressure difference due to the escalation in the flow velocity. The pressure loss between two points can be gauged by a pressure transducer or a manometer. A flow rate measurement device seems to be implemented by obstructing the flow. Thus, flowmeters based on this principle are named obstruction flowmeters. Those are widely utilized to gauge the flow rates of gases and liquids when the fluid is single phase and well-mixed, the flow is continuous rather than fluctuating. The flow profile is uniform and well developed. According to these occasions and when orifice plate is manufactured and applied in terms of appropriate standards, the flow rate can be calculated using formulae based on researches with national and international standards.

Orifice plates are generally produced with sharp-edged circular corners and implemented concentric with the pipe and with pressure tapings according to standard distances upstream and downstream of the plate which are in regard to ISO 5167 and other standards. The corners might be rounded, the orifice might be applied eccentric to the pipe, and the pressure tapings might be different. Those variations are in many standards and handbooks. Every combination contributes increase in coefficients of discharge.

As we design and install the orifice plate, the flow rate is usually indicated with a low uncertainty basically due to taking the square root of the differential pressure taps and using a proper constant. Even compressible flows which vary in pressure and temperature can be measured with reasonable uncertainty up to the purpose of the measurement. There are three standard positions for pressure tapings (ISO 5167), namely [23]:

- Corner taps which is placed immediately upstream and downstream of the plate. This type is appropriate when the plate is supported with a carrier incorporating tapings

- D and D/2 taps (radius taps) which is placed one pipe diameter upstream and half a pipe diameter downstream of the plate.

- Flange taps placed 25.4mm upstream and downstream of the plate,

- 2½D and 8D taps (recovery taps) which is placed 2.5 pipe diameters upstream and 8 diameters downstream, where the measured differential is equal to the unrecoverable pressure drop because of the orifice.

- Vena contracta tapings which is placed one pipe diameter upstream and at a position of 0.3 to 0.9 diameters downstream, according to the orifice type and relatively size to the pipe, minimum fluid pressure.

The differential pressure varies for each combination thus, the discharge coefficient used in flow measurements partially come down to the tapping positions.

The velocity in Equation 2.13 is calculated by assuming no loss; therefore it is the maximum velocity which occurs at the construction site. In actual fact, pressure losses due to frictions cannot be evaded thus, the velocity is lower. Besides, the fluid continues to pass the obstruction, and the vena contracta area is less than the flow area of the

obstruction. Both losses can be attributed to a correction factor named the discharge coefficient which is a value ($C_d < 1$) determined experimentally.

Discharge coefficient (also known as coefficient of discharge) is the ratio of actual flow rate to theoretical flow rate. Theoretically, the discharge coefficient can be found from the mass flow rate of a fluid flowing through a straight pipe as follows;

$$\dot{V} = C_d A_0 \sqrt{\frac{2(P_1 - P_2)}{\rho(1 - \beta^4)}} \qquad (2.14)$$

where A_o is the area of the hole of the orifice plate. ΔP is the pressure difference at tapings, ρ is the fluid density and β is the ratio of the orifice hole diameter to pipe diameter. Discharge coefficient comes down to both β and Reynolds number. There are charts and curve fitted correlations available in a whole host of papers in literature [20];
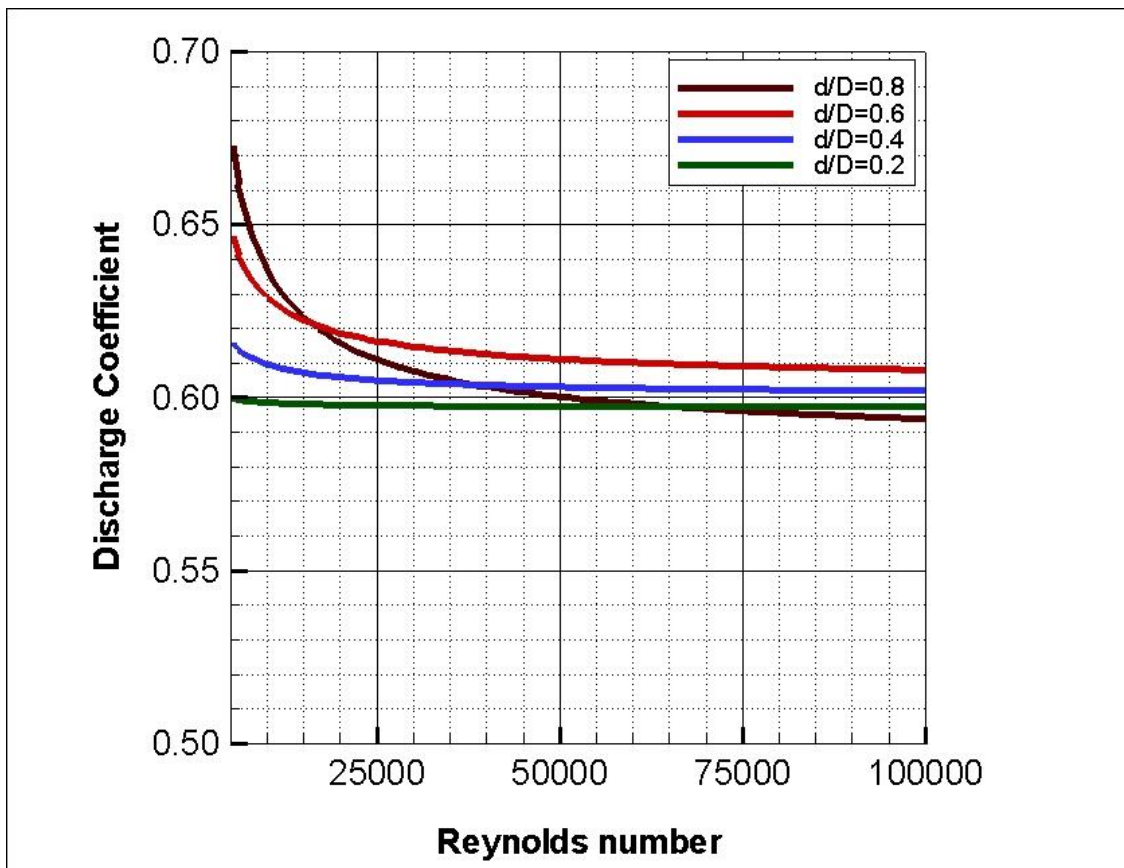
Figure 2.9. Discharge coefficient chart respect Reynolds number for Orifice Plates

$$C_d = 0.5959 + 0.0312\beta^{2.1} - 0.184\beta^8 + 0.0029\beta^{2.5}\left(\frac{10^6}{Re}\right)^{0.75} \qquad (2.15)$$

In the literature, it has been said that the correlation is valid for $0.25 < \beta < 0.75$ and $10^4 <$ Re $< 10^7$. However, it is also noted that the manufacturer's data should be consulted when it is available for a particular design. Thus, we came up with an experimental set up and the orifice plates as a particular design at the next chapter. We found that even for low β and Reynolds number, correlations in literature still work. In addition, discharge coefficient (C_d) converges to 0.6 for β (d/D) being almost zero in Figure 2.9 for wide range Reynolds number based on orifice diameter. In the next chapter, we investigate discharge coefficient by measuring friction factor and optimizing it in regard to giving best fit for measured friction factor with those in Moody's Chart (Figure 2.7).

2.5.   ACOUSTIC LOOP MECHANISM OF CORRUGATED PIPES

The mechanism behind whistling in pipes are not exactly defined. A well-known theory is the vortexes induced by the cavity bringing about a noise called whistling. On the other hand, there is an another theory underlining that the vortices in the grooves lead to vortices generated at the inlet thus, no sound would be existed without these inlet vortices. For instance, when a gas is used as an operating fluid in the process of flow, air is driven into the inlet. At this point, the flow is unstable and inlet vortexes are induced due to the inlet edge which runs into situation where a smooth pipe with corrugations at the outlet of section is not generating sound, whereas the same corrugated section at the inlet section generates sound audibly. At the inlet section of the pipe, vortexes are either stuck in the cavities or not strong enough to burst to core flow to amplify pressure oscillation to whistle.

Pipes with corrugations can be considered as comprised of cylindrical cavities all together. A great variety of resources covers sound due to cavity flow and related phenomena of vortex oscillations. Cavity fluctuations can be classified to the depth such that if H/Pt > 1 and if H/P$_t$ < 1.

Perturbations are claimed to be caused by the amplification of vorticity oscillations in the shear layer where fluid passes over the cavity due to the following loop in Figure 2.10. Pressure oscillation brings about vortex in the shear layer at the leading edge of the cavity. The vortex is convected at the roughly half speed of the free stream velocity to the core flow. Thus, a fluctuating force caused by the vortex behaves as an acoustic dipole. An acoustic resonant mode of the tube is driven by this dipole which amplifies the sound pressure oscillation. Those perturbations comply with the leading edge of the groove at which more vortexes are induced. This mechanism is almost same as which was suggested for edge tones, jet speeds which are such mechanisms involving an acoustic dipole source and causes an unsteady pressure difference across a shear layer giving an increase to vortexes that interfere mean flow. We described the mechanism between acoustic and flow field in the diagram below. (Figure 2.10)
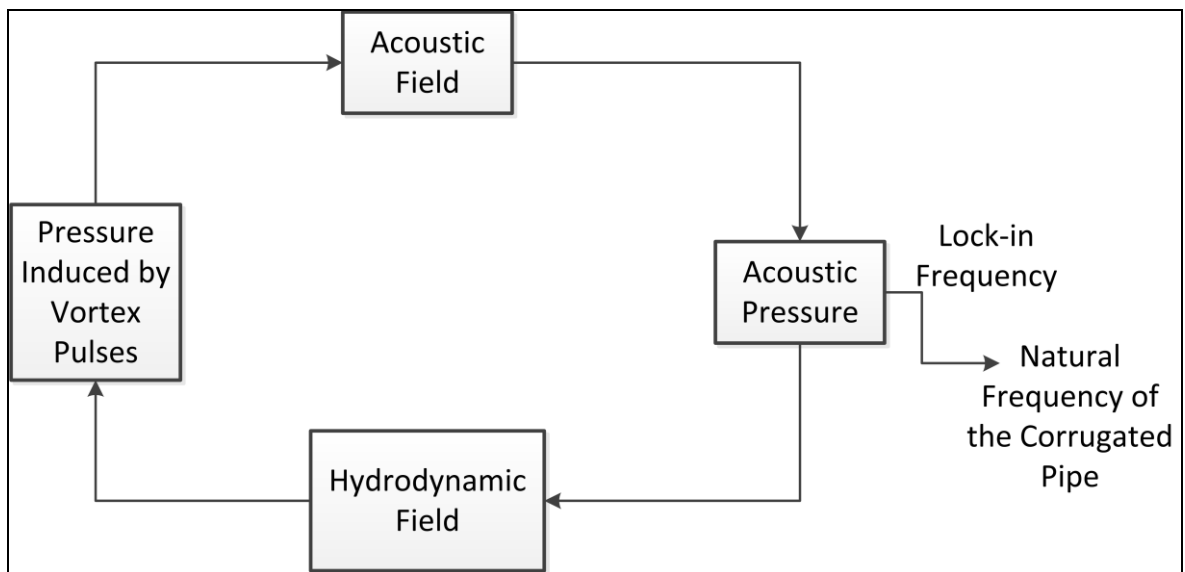
Figure 2.10. Schematic representation of acoustic mechanism

According to the coupling mechanism, the existence of acoustic regimes and variation of the fluctuation frequency for a given range of velocity are classic investigations are lock-in phenomenon of acoustics. Moreover, the existence of a dramatic escalation of the fluctuating pressure amplitude up to the flow velocity demonstrates that the acoustic mechanism is with the feedback loop which maintains the oscillation. The hydrodynamic disturbances because of the corrugations decay to brand noise turbulence below the critical

minimum velocity reaching the minimum instability velocity boundary, acoustical resonant effects resulting in strong oscillations amplify the disturbances at the shear layer.

2.6. NUSSELT NUMBER AND GNIELSKI CORRELATION

Nusselt number is the ratio of heat transfer rate based on convection and heat transfer rate based on conduction. Convection comprises of advection and diffusion. Nusselt number around 1, such that convective heat transfer rate is equal to conductive one which characterizes the flow as slug flow or laminar flow. Higher Nusselt number is equivalent to more active convection for turbulent flow.

The convective and conductive heat transfer rates are related to each other and to the surface which is normal to boundary surface.

$$Nu = \frac{convective\ heat\ transfer}{conductive\ heat\ transfer} = \frac{hL_c}{k} \tag{2.16}$$

where h is the convective heat transfer coefficient of the flow, L_c is the characteristic length (the pipe diameter is used in the case of internal flows), k is the thermal conductivity of the fluid.

Gnielinski correlation defines Nusselt number with respect to Darcy friction factor, Reynolds number and Prandtl number for circular tubes.

$$Nu_D = \frac{\left(\frac{f}{8}\right)(Re_D - 1000)Pr}{1 + 12.7\left(\frac{f}{8}\right)^{1/2}\left(Pr^{2/3} - 1\right)} \tag{2.17}$$

The correlation above is valid for constant heat flux at wall and in a range of Reynolds number between 3000 and 5×106 and Prandtl number between 0.5 and 2000. [24]

In our experiments we calculated Nusselt number in regard to Prandtl number and Reynolds number with corresponding friction factor.

3. EXPERIMENTAL SETUP

3.1. INTRODUCTION TO EXPERIMENTAL SETUP

The corrugated pipe was connected to a chamber which was built in a small scale by following ANSI/AMCA Standard 210-99, as shown in Figure 3.1. The total five settling means were placed inside the chamber to provide uniform flow. The chamber was divided into two compartments and an orifice was installed between two compartments. Each compartment had four pressure taps, and a pressure transducer connected the pressure taps of two compartments, thus measuring pressure differentials across the orifice. A fan with the shutoff pressure of approximately 800 Pa was located at the exit of the system. Flowrate was controlled by a gate at the exit of the fan and by a leak door between the chamber and the fan.
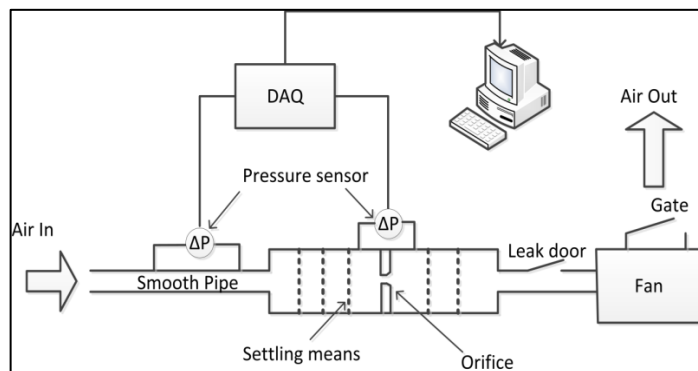
Figure 3.1. Schematic of experimental setup for calibration

Flowrates were measured by an orifice meter. Four different sizes of orifices, 9.92 ± 0.02 mm, 14.07 ± 0.03 mm, 20.17 ± 0.07 mm and 30.02 ± 0.14 mm in diameter, were employed and an appropriate one was selected and installed inside the chamber, depending on the range of flowrate. Orifices were carefully calibrated with a smooth PVC pipe, 16.28 mm $\pm$ 0.19 in diameter, by comparing friction factors for both laminar (using $f = 64/Re$) and turbulent flows (using the Colebrook equation for the smooth pipe). A PVC pipe, 4 m in length, was connected to the chamber and two pressure taps with the distance of 2 m were placed on the pipe. Care was taken to ensure fully developed flow between two pressure

taps. The Darcy friction factor was calculated from Equation 4.2 by measuring pressure loss and flow rate. In Figure 3, the test data with the discharge coefficient of 0.60 for all four orifices are compared with friction factor in the smooth pipe over laminar and turbulent regions, and their discrepancies in friction factors are 6% for the laminar zone and 7% for the turbulent zone. Therefore, the total uncertainty of measuring the friction factor in the present study may be less than an order of 10%. This uncertainty arises from various uncertainties such as the orifice sizes, the discharge coefficient, pipe diameters and the accuracy of the pressure transducers. The test setup employed several differential pressure transducers with the ranges of 25, 100, 250, 500 and 1000 Pa to measure pressure differentials across the pressure taps on the pipe and across the orifice. During the preliminary tests, the entry length was examined by measuring pressure drops at different pressure tap locations. It was found that the entry lengths of corrugated pipes for laminar flow were almost the same as those of the smooth pipe. In turbulent region, however, it was observed that flow became fully developed with a shorter entry length for corrugated pipe. A microphone was placed near the inlet of the corrugated pipe to record the whistling frequencies of the pipe. The recording duration was usually 10 s and the sampling rate of 88 kHz was selected, which is sufficiently large to satisfy Nyquist criteria. The Fast Fourier Transform (FFT) algorithm was used to determine the whistling frequency.

3.2.   TESTED CORRUGATED PIPES AND THE SMOOTH PIPE

The present study is employed the stainless-steel pipes with the corrugation of circular cross section, in diameters of 20.4, 24.5, 34.5 and 40.1 mm. There are two pipes with different lengths for each same in the diameter. As can be seen in Table 3.1, each pipe, which differs in diameter, has distinct corrugation size.
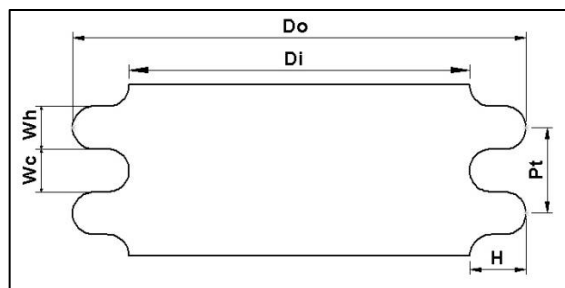
Figure 3.2. Schematic of a corrugated pipe

Table 3.1. Dimensions of the tubes tested in the present study as shown in Figure 3.2

Dimensions	Pipe 1	Pipe 2	Pipe 3	Pipe 4
D_i (mm)	20.4	25.4	34.5	40.1
D_o (mm)	26.7	31.9	41.1	49.6
W_c (mm)	2.3	2.2	1.7	2.8
W_h (mm)	2.5	3.1	3.1	3.8
P_t (mm)	4.8	5.3	4.8	6.6
H (mm)	3.1	3.2	3.3	4.7
L_1 (mm)	2000	3007	4001	5097
L_2 (mm)	1470	1490	1990	1960
W_h/D_i	0.122	0.122	0.090	0.095
W_c/D_i	0.113	0.089	0.049	0.070
H/D_i	0.154	0.128	0.096	0.118

There are pressure taps placed in equal distance on all pipes longer in lengths. That allowed us to investigate entrance length at which the flow becomes fully developed. The pressure taps are inserted at equal distance by using a sticky pasta and a strong glue to strengthen the position of the tap on the pipe. We also support the straightness of the pipe with long aluminum sheet plates to prevent any problem for assembly of the pressure taps. We also placed a plate made of plexi glass at outlet section of the pipe to insert the pipe to the flow chamber. We glued the plate to the pipe concentrically by filling the gap between the plate and the pipe with silicon which can restrain at high temperature.
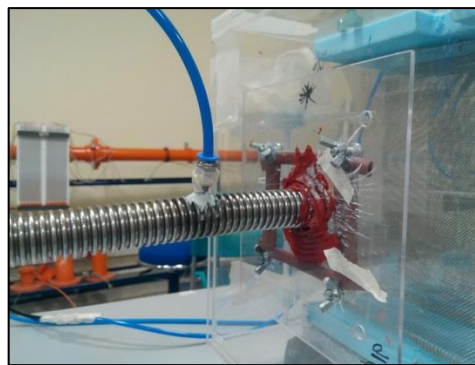
Figure 3.3. Picture of tap and plexi glass assembly to the flow chamber

We measured the pressure loss for each pipe by inserting pressure transducers to another pressure tap until the measurement result is ensured to be stable. We found that the entrance length for corrugated pipe is same as for smooth pipe in the laminar region. However, the flow becomes fully developed at shorter distance for corrugated pipe in turbulent region.

We performed the calibration with a PVC pipe as a smooth pipe having a diameter of 16.28 ± 0.19 mm and 4 m in length. We followed same procedure for placing pressure taps and the plate as described above for corrugated pipes but exceptionally we inserted two pressure taps over the pipe this time. We placed the high pressure tap 2 m away from the inlet section to ensure that the measurements are taken for fully developed flow in laminar region. We compared the results in terms of friction factor which is available in Moody chart for both laminar and turbulent region.

3.3.   ORIFICE PLATES AND FLOW CHAMBER

We manufactured many orifice plates with circular holes which are made of aluminium have different sizes in diameters but the calibrated ones have diameters of 9.92 ± 0.02 mm, 14.07 ± 0.03, 20.17 ± 0.07 and 30.02 ± 0.14 mm. It is known that discharge coefficient of orifice plates is highly sensitive to how carefully plates are produced. Thus, we mind that there was no leftover from the manufacturing process on the plate. Moreover, two of the orifice plates (9.92 and 14.07) mm were chamfered at downstream edge whereas the remaining were not. Regarding the literature available for orifice plates with different types, the discharge coefficient is influenced by shape of the hole whether it is chambered or not.

Figure 3.4. Picture of orifice plates used in the experiments

We chambered the downstream edge of the orifice holes 1 mm at the angle of $45°$ to the upstream. Three of orifice plates (9.92 mm, 14.07 mm and 20.17 mm) have thickness of 3 mm and the one with a diameter of 30.02 mm has a thickness of 4mm. We kept the thickness lower for the orifice plates with small size in diameters. Due to fact that the discharge coefficient would have been swayed otherwise.
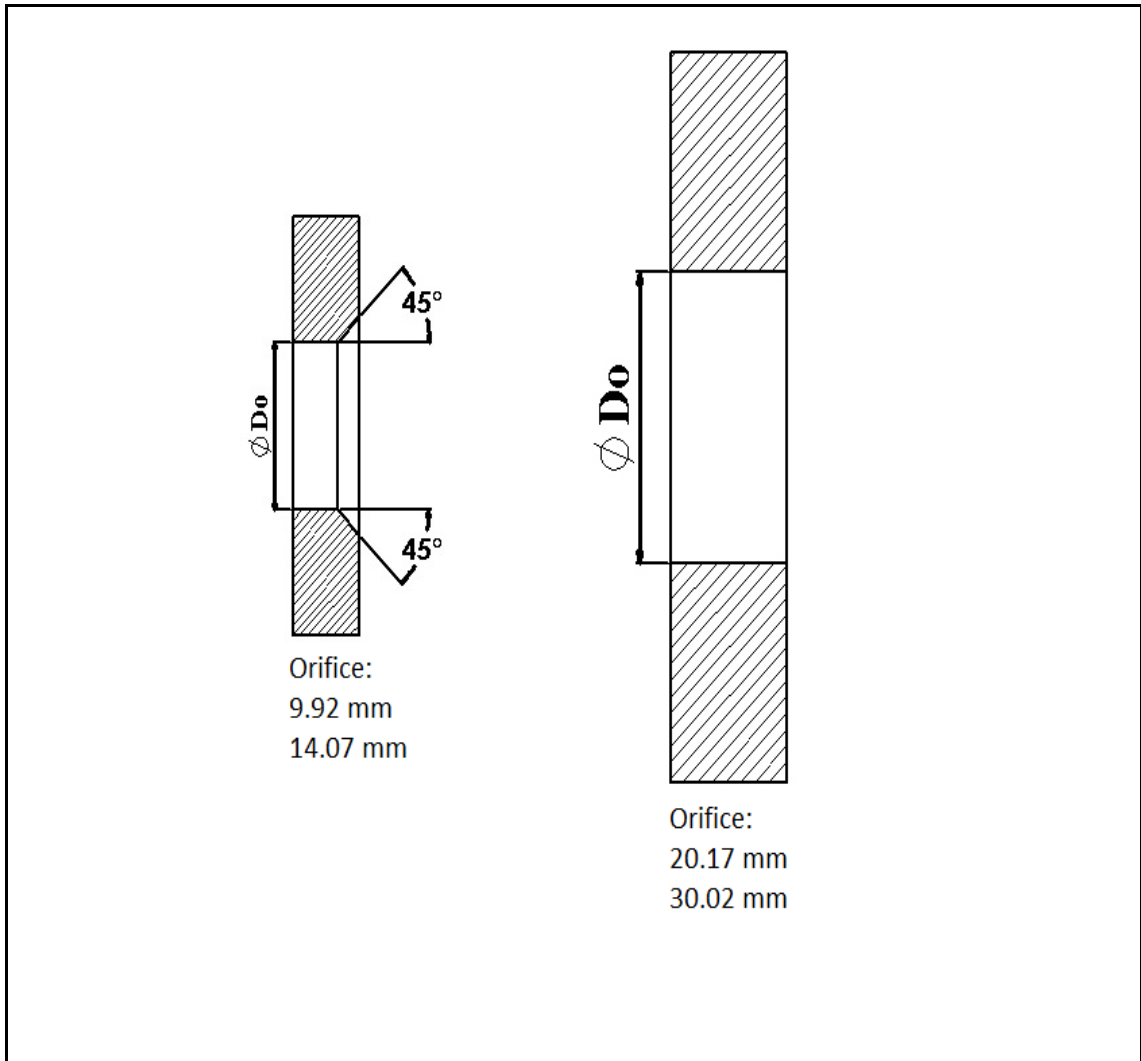
Figure 3.5. Schematic of orifice plates used in the experiments

We built the flow chamber in a small scale by referring from ANSI/AMCA Standard 210-99. Another chamber which is smaller than the former is inserted between the fan and the leak door chamber. The leak door allows us to adjust desired flow rate over a range as much as the fan allows. The fan which has the shutoff head of 70 m was located to suck the air from the pipe flow and the flow chamber as shown in Figure 3.6.

Figure 3.6. Picture of experimental setup

Flow chamber divided equally into two compartments has a height of 0.33 m and width of 0.66 m. Three pressure taps are placed at the upstream and four are placed at the downstream. All pressure taps are inserted immediately for both sides of the chamber which corresponds to corner taps. The orifice plate is inserted where the chamber is divided in two. Thus, pressure drop between the compartments is measured at these taps by a pressure transducer. Moreover, total five settling means are placed in the chamber, three are at the upstream and two are at the downstream. We provided the flow to be uniform and increase the accuracy of the pressure drop measurements between the compartments of the flow chamber with the help of settling means.
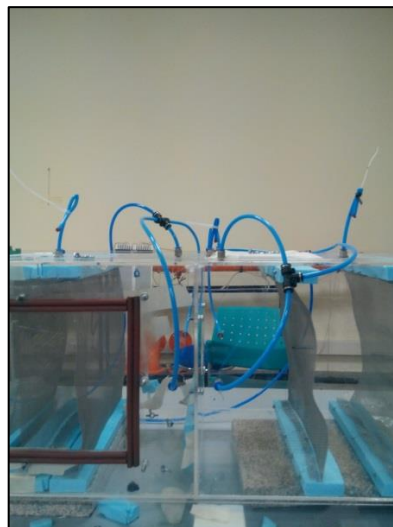
Figure 3.7. Picture of taps placements on the flow chamber

There were four critical assemblies on the flow chamber. For instance first is where the chamber and the pipe are connected. The second is where orifice plate is inserted, the third is where we put the settling means and orifice plates and the fourth is where the leak door chamber and the flow chamber are connected. They are crucial because these assembly regions are where we have undesired air leaks. In order to hinder, we placed plastic flexible stretches at the edges of the assemblies. According to calibration results, they served well for the purpose.
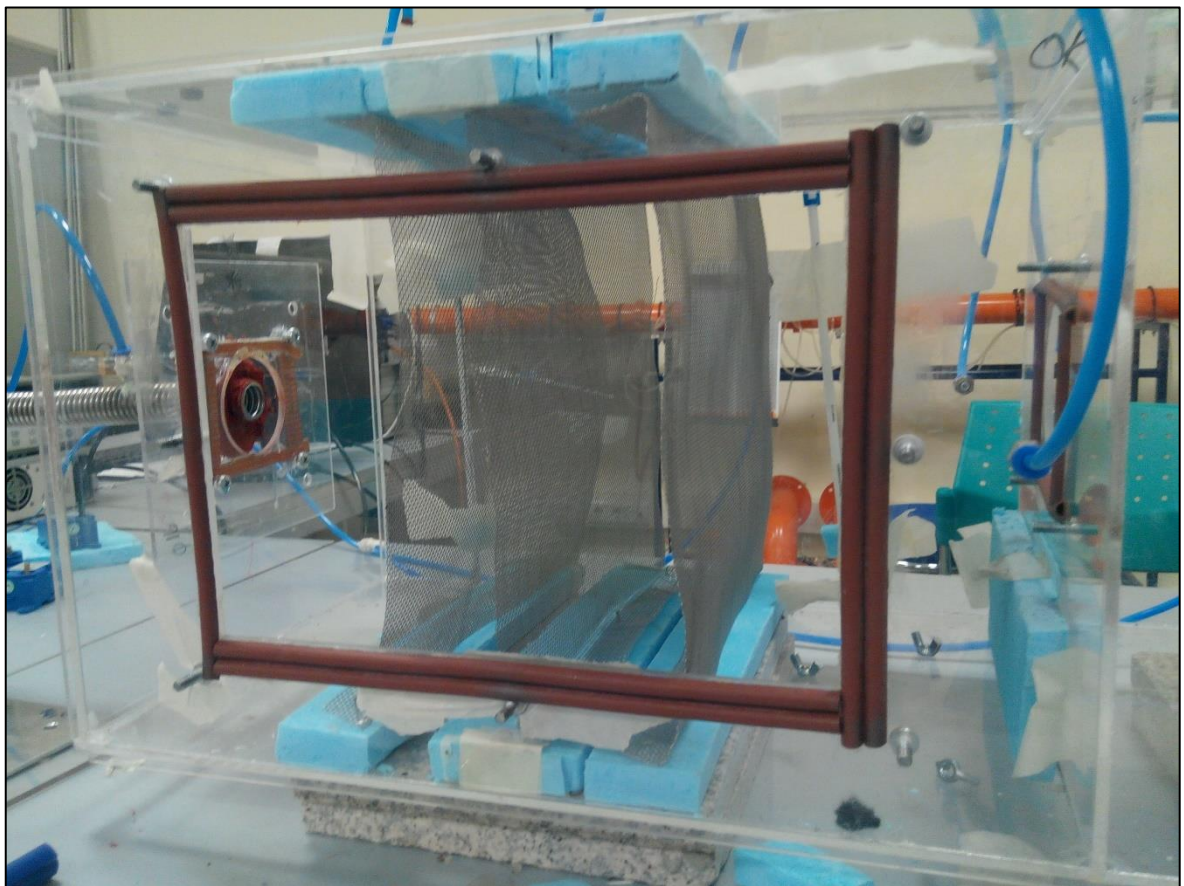
Figure 3.8. Picture of critical areas due to assembly on the flow chamber

As mentioned for the flow chamber and orifice plates above, we estimated the discharge coefficient in terms of the ratio of the orifice hole diameter to the height of the flow chamber which corresponds to β in this case by using Equation 2.15;

β is different for each orifice plate but very small for all. Variety in Reynolds number based on the orifice diameter for the equation above has a slight influence in regard to the

constant term. Therefore, the discharge coefficient must be almost 0.6 for all orifice plate tested in the calibration. For instance, C_d is for orifice plate 30.02 mm in diameter while Reynolds number based on orifice diameter is 500,

$$\beta = \frac{Orifice\ diameter}{Height\ of\ the\ flow\ chamber} = \frac{30.02\ mm}{330\ mm} = 0.091$$

$$C_d = 0.5959\ +\ 0.0312 \times 0.091^{2.1} - 0.184 \times 0.091^8 + (0.0029 \times 0.091^{2.5})$$
$$\times \left(\frac{10^6}{500}\right)^{0.75} = 0.598$$

Anyway, we conducted some experiments on the determination of discharge coefficient by measuring pressure loss for pipe and the compartments of the flow chamber and we optimized the discharge coefficient by converging to the experimental results of friction factor to the ones from Moody chart and Colebrook's correlation. In Figure 3.9, we present those discharge coefficients optimized in terms of Reynolds number and friction factor.
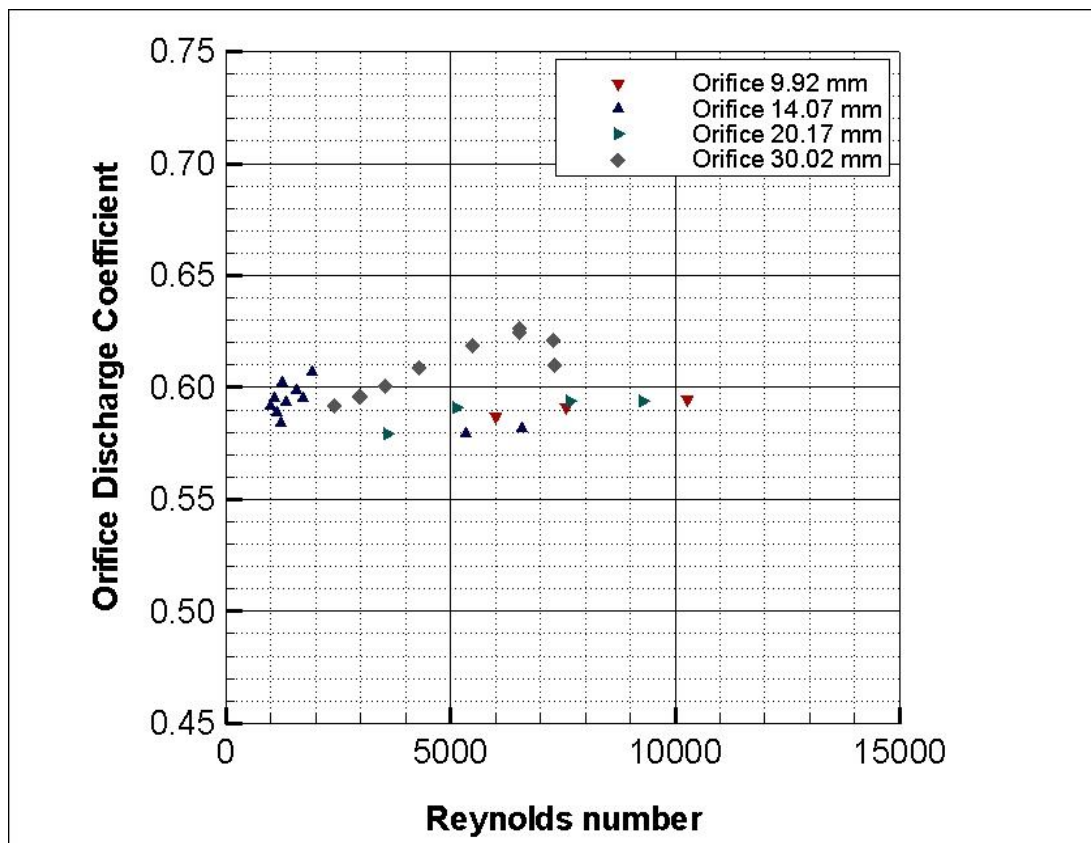
Figure 3.9. Discharge coefficients acquired from calibration of orifice plates

As can be seen in Figure 3.9, the discharge coefficient deviates slightly from 0.6 for all orifice plates but the results are reasonable when we consider the optimization regarding the friction factor because the fluid might indicate some pulses while flowing through pipe in the laminar region particularly for Reynolds number from 1500 to 2000 (transient region). Thus, we used 0.6 for discharge coefficient when we measured friction factor for corrugated pipes. Yet, we took this reasonable deviation into account for the uncertainty analysis.

3.4.   DATA ACQUISITON

The experimental setup comprises of a fan, leak door chamber, flow chamber divided in two compartments, orifice plate and the pipe to be tested for conduction of experiments; the pressure sensors, data acquisition device and the board, power supply and a microphone for data acquisition of experiments. (See Figure 3.11) We measured pressure losses for flow chamber and the pipe with six pressure transducers which are different in the range of measurements. Five of the transducers are provided by ORASS with maximum ranges of 100, 250, 500 and 1000 Pa. The one with a range of 0 to 25 Pa is provided by OMEGA which is the most sensitive.

Figure 3.10. Picture of pressure transducer used to measure pressure losses

We chose the two of them regarding how high the pressure losses are for the flow chamber and the pipe because measurement sensitivity is at paramount importance to acquire good result. For instance, OMEGA pressure transducers were mostly used for the pressure loss through pipe in laminar region. Thus, we usually mind the proper orifice plates in the first place in regard to the pressure transducer. All pressure transducers have current output from 4 mA to 20 mA and all are powered by the power supply at 24 V.
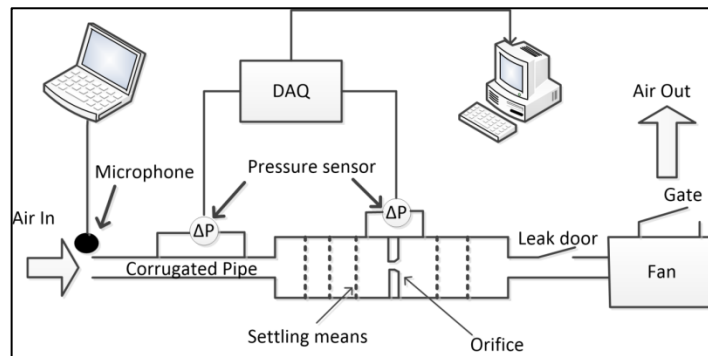
Figure 3.11. Schematic of experimental flow chart

We measured pressure losses through the pipe and the flow chamber as current outputs which are collected by a data acquisition device provided by Agilent.

Figure 3.12. Picture of Agilent's DAQ and power supply

The pressure transducers are connected on the acquisition board inserted in Agilent's Data Acquisition device as shown in Figure 3.13. The collected data by the data acquisition device are transmitted to the desktop computer. The Agilent's Data Benchlink software is utilized to display and observed current output results and save them in order to perform the analysis.
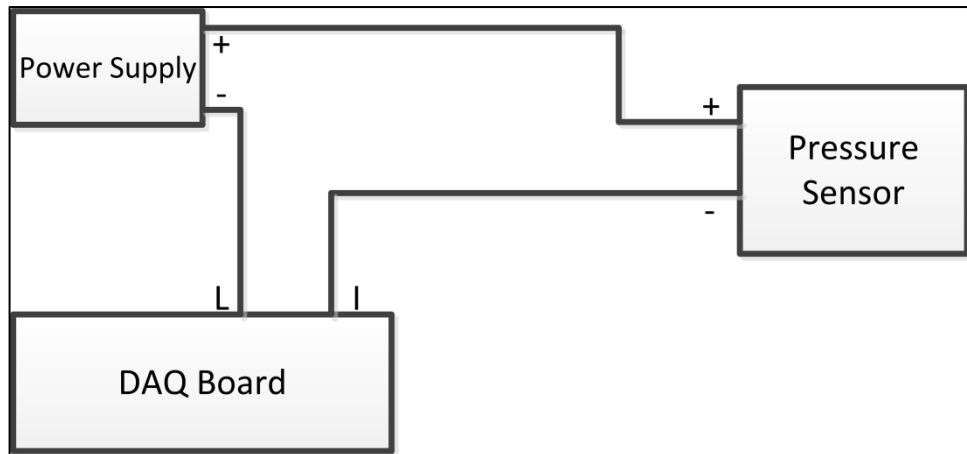
Figure 3.13. Schematic diagram of pressure transducers connection to DAQ

We obtained data for sound wave with a microphone which has a frequency range from 50 to 15000 Hz and sensitivity of -72 dB and impedance resistance of 600 ohm. We gathered data as voltage output to the laptop where we analyse by the help of commercial software named MATLAB.

Figure 3.14. Picture of the hand microphone used in the experiments

3.4.1. Acquisition of Pressure Loss

We gathered data in current output form for the pipe and the flow chamber. The use of settling means for uniform flow was seen to work out for the purpose intended. The measurement deviation significantly is killed with the help of those settling means in the flow chamber. We increased accuracy of the measurement for the pressure loss due to orifice plate dividing the chamber in two compartments. We applied the data sampling rate 5 Hz which is quite adequate for these steady state measurements. However, we have to consider the data sampling procedure because as we initiate the flow through pipe we had to wait for a few seconds until the flow settles inside both pipe and the flow chamber. Particularly, the data sampling history is observed for low flow rates when the flow settles before analysing the data because settling of the flow delays for low velocity rates. We also mind the zero output of the pressure transducers to keep the accuracy high. Especially, the fluid flowing slowly leads to low pressure loss thus, the pressure loss is measured when there is no flow inside pipe as well as the flow chamber and while the data is taken, the fan is run to initiate the flow. Even the sampling is enough; we only stopped the fan but continued to gather data to observe whether the current output comes to initial value which was taken before the fan is run. In order to keep sampling uncertainty low, we took mean value from where the flow settles, which was observed carefully, to where the fan is stopped. We also took mean value of zero gage pressure output before the fan is run and after the fan is stopped. This procedure may not be so important for measuring high Reynolds number based on pipe diameter and corresponding friction but it is at paramount importance to measure the friction factor and Reynolds number in the laminar region because of very low pressure loss through pipe. The pressure loss is calculated in terms of current output provided by the pressure transducers as the equation follows;

$$\Delta P = \frac{I_{avg} - I_0}{I_{max} - I_{min}} P_{range} \qquad (3.1)$$

where I_{avg} is the average current output while air is flowing, I_o is current output while air is not flowing, I_{max} is the maximum current available for pressure transducer (20 mA) and I_{min} is the minimum current available for pressure transducer (4 mA) and P_{range} is the maximum pressure value available for the sensor to read.

For instance, the procedure is followed and the equation is applied for an analysis of pressure loss for the smooth pipe with orifice plates having a diameter of 14.07 mm. Calculation of Reynolds number and corresponding friction factor is performed as it is below;
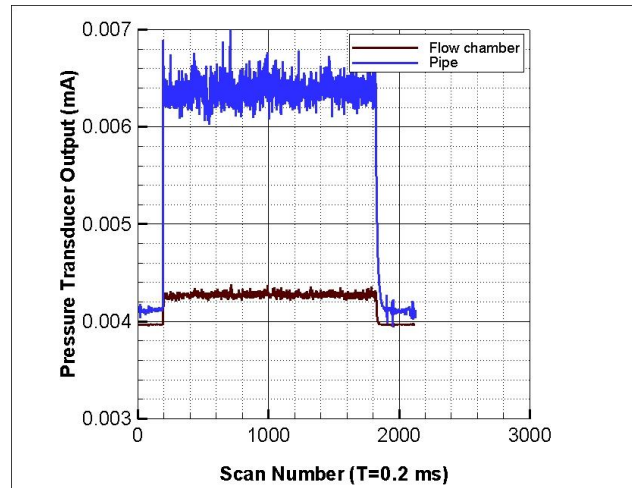
Figure 3.15. Sample data of pressure loss measurement in the pipe with a sampling rate of 0.2 ms

Table 3.2. Outputs of sample data

	Flow chamber	Pipe
Zero gage pressure average current output before fan is run (A)	3.96×10^{-3}	4.11×10^{-3}
Zero gage pressure average current output after fan is run (A)	3.96×10^{-3}	4.11×10^{-3}
Average current output (A)	4.27×10^{-3}	6.38×10^{-3}
Max pressure in the range (Pa)	100	25
Pressure loss (Pa)	1.91	3.55

The current output is taken average of 765th scanned value to 1750th which the last value taken before the fan is stopped. We observed the flow is settled before 765th value but we

dismissed the data for the safety of measurement. We used pressure transducer with a range from 0 to 100 Pa for the flow chamber and another with a range from 0 to 25 Pa. We found pressure loss 1.90 Pa for the flow chamber and the 3.54 Pa for the pipe at 2 m interval. Thus, the volumetric flow rate is found by applying Equation 2.14 at which discharge coefficient (C_d) is taken as 0.6 and β is taken as zero so subtracted from equation. Thus equation becomes even for all orifice plates as it follows;

$$\dot{V} = C_d A_0 \sqrt{\frac{2\Delta P_0}{\rho}} \qquad (3.2)$$

where ΔP_o is the pressure loss, A_o is the cross section area of the hole of the orifice plate and ρ is the air density determined in terms of temperature which was measured by a thermocouple placed in the flow chamber.

$$\dot{V} = 0.60 \times \frac{\pi \times 0.01407^2}{4} \sqrt{\frac{2 \times 1.91}{1.18}} = 1.67 \times 10^{-4} \, m^3/s$$

The mean fluid velocity in the pipe can be found by benefitting from the conservation mass to determine friction factor;

$$U_\infty = \frac{4\dot{V}}{\pi D_p{}^2} \qquad (3.3)$$

where ΔP_p is the pressure loss at the specified length interval (L). D_p is the pipe diameter and U_∞ is the flow mean velocity in the pipe. We can manipulate Equation 2.7 with Equation 3.3 as shown below;

$$f = \frac{\Delta P_p \pi^2 D_p{}^5}{8L\rho\dot{V}^2} \qquad (3.4)$$

As one can see why the measured friction factor pipe is so sensitive to the pipe diameter in the Equation 3.4 and we also consider and rewrite the Reynolds number equation as follows;

$$Re_D = \frac{\rho U_\infty D_p}{\mu} \tag{3.5}$$

$$Re_D = \frac{4\rho \dot{V}}{\pi \mu D_p} \tag{3.6}$$

where μ is the dynamic viscosity determined in terms of temperature which was measured by a thermocouple placed in the flow chamber. It can be clearly seen, the pipe diameter measurement uncertainty for the Reynolds number determination influence less than for the friction factor determination. We found that the flow through the pipe is laminar and the error rate was approximately 1 % for the friction factor compared to Equation 2.8. The result for friction factor is quite accurate even though we measured pressure difference of 2 Pa between two compartments of the flow chamber with a pressure transducer measuring in range from 0 to 100 Pa.

We noted the flow is not chaotic even for corrugated pipe in laminar region. However, in turbulent region, the flow in the corrugated pipe is fluctuating which sways the pressure loss measurements at high flow rates. If the pressure transducer is sensitive, these pulsations in the flow cause disturbance in the current output resulting instant leaps in friction factor on the trend and inconsistency between the pressure transducers. Therefore, we placed chambers to the pneumatic pipes heading to high and low pressure plugs on the pressure transducer. We killed these undesired pulsations in the current output and we observed the resulting friction factors are consistent for each pressure transducers.

3.4.2. Acquisition of Vortex Shedding Frequency and Sound Pressure Level

We used a hand microphone to record sound wave pressure as a voltage output for 10 seconds. Fast Fourier Transform (FFT) is implemented for each data set to determine resonant frequency in the pipe. Fast Fourier transform (FFT) is an algorithm which

computes the discrete Fourier transform (DFT) and its inverse and reduces the number of computations needed for N points. Fourier computation converts time to frequency.

$$X(k) = \sum_{j=1}^{N} x(j)w_N^{(j-1)(k-1)} \tag{3.7}$$

$$X(j) = \frac{1}{N}\sum_{k=1}^{N} x(k)w_N^{-(j-1)(k-1)} \tag{3.8}$$

where

$$w_N = e^{-2\pi i/N} \tag{3.9}$$

We applied the sampling frequency as 88 kHz which is more than enough to satisfy Nyquist criteria. Nyquist suggests that the anti-aliasing filter suppresses higher frequencies than the half of the sampling frequencies which is also known as folding frequency of a sampling system. In our case, hand microphone used in the experiments can read the resonant frequency within a range of 0 to 20 kHz. Thus, the sampling frequency must be higher than 40 kHz. In the figures below, we present resulting frequency and sound pressure level as voltage and decibel output at Re=12400 for corrugated pipe 20.4 mm in diameter and 2 m in length;
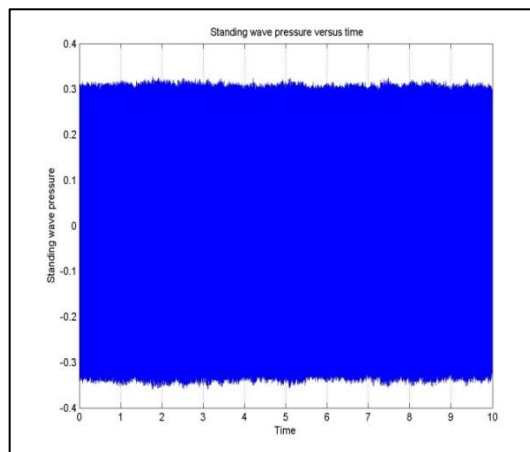
Figure 3.16. Sample data of acoustic pressure wave measurement as voltage output

As per Figure 3.16, the sound wave is oscillating within the range of around about - 0.3 to 0.3 mV. Thus, we have the data above and when we implement the FFT to these recordings, we have the frequency of the sound wave and its amplitude shown in the spectrum as in mV and dB;
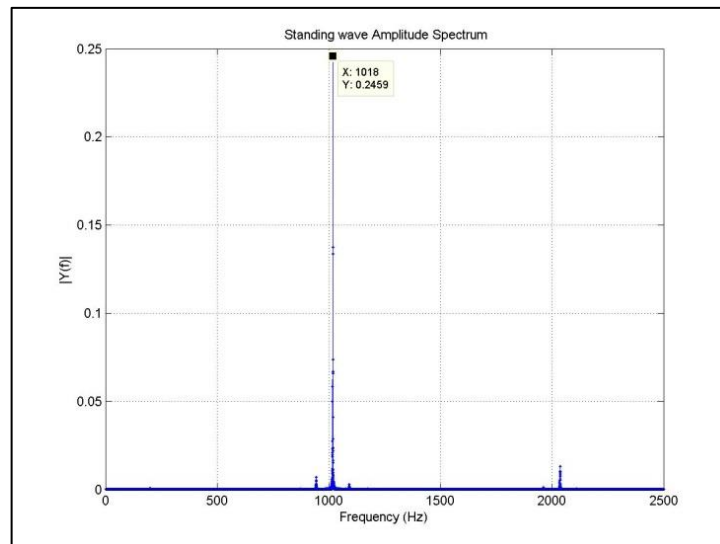
Figure 3.17. Standing wave amplitude spectrum of the sample data
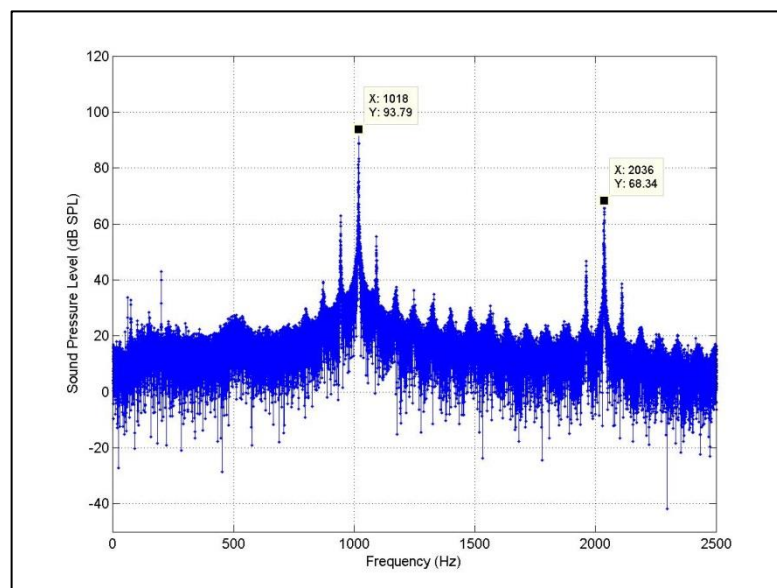
Figure 3.18. Sound pressure level versus its frequency measured by the microphone for the pipe, 20.4 mm in diameter and 2 m in length. Acoustic waves are locked in with the vortex shedding at the frequency of 1018 Hz

As can be seen in Figure 3.17 and Figure 3.18 (FFT figures), acoustic waves locked in the hydrodynamic waves at 1018 Hz which is the frequency of vortexes shedding to the core flow. The whistling power or the sound wave pressure is 0.2459 mV or 93.79 dB. Its harmonic can be also detected in the spectrum as 2036 Hz (2×1018 Hz) with the wave pressure of 68.34 dB. By knowing the fundamental frequency is around 75 Hz, the vortex sheddings lock in the acoustic pressure waves at;

$$acoustic\ mode = \frac{1018}{75} \cong 13^{th}\ mode$$

The wavelength can be determined as it follows;

$$wavelength = \frac{2}{13} \times 2 \cong 0.31$$

Thus, the air column has 13 nodes and 14 antinodes. Besides, the effective speed of sound can be also calculated;

$$C_{eff} = 1018 \times 0.31 \cong 315\ m/s$$

The effective speed of sound (speed of sound of air in the corrugated pipe) is less than the speed of sound for free stream air due to fact that the corrugations slow down the sound travelling through corrugated pipe.

3.5. EXPERIMENTAL METHODS OF HEAT TRANSFER FOR CORRUGATED PIPES

Experimental methods of heat transfer are presented in many researches. Those methods usually suggest for measuring temperature on a surface with use of thermocouples carefully soldered. In general, glue is used to place thermocouples on a surface. However, glue must be dropped carefully in order to prevent undesired thermal resistance between thermocouple and the surface thus the surface and the thermocouple must be in contact as much as possible. On the other hand, if the surface is made of metal substance which is

conductive electrically, the surface must be isolated from the thermocouple to read temperature for instance very thin coated tapes. (See Figure 3.19)

Figure 3.19. Coated tape on the pipe surface

As can be seen in the picture below (Figure 3.20), we put together two terminal of the thermocouple with very thin solder. As it is known that the corrugated pipes comprise of hollows and crests. Therefore, thermocouples which are placed on crest and hollow surfaces of corrugated pipes must be soldered very thin.
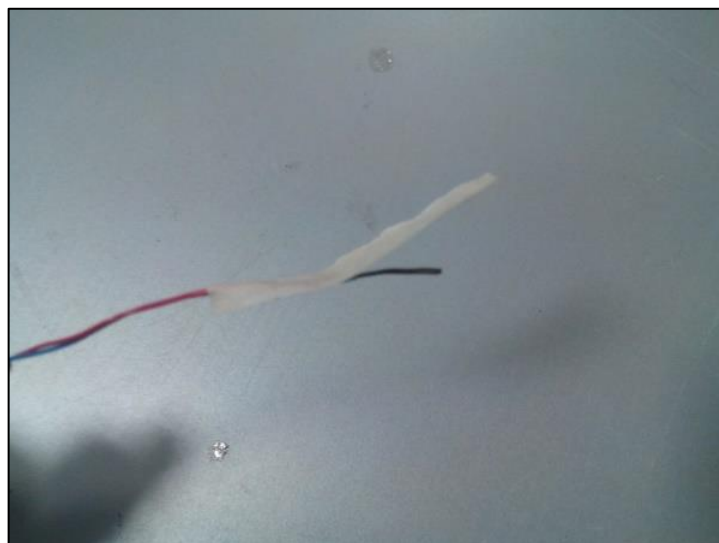
Figure 3.20. Well Soldered Thermocouple with tape ready to be inserted on the pipe surface

However, our experiments for heat loss indicated the surface temperature measurements are unstable and inconsistent along pipe which we will come to in the results section for corrugated pipe with a diameter of 20.4 mm. Therefore, we enhance placement of thermocouple on the corrugated pipe surface and tested this method on the corrugated pipe with diameter of 34.5 mm. For the pipe with diameter of 20.4 mm, we used tape to isolate the thermocouple then put diameter on the surface very carefully in order to provide fully contact with the surface, drop very little glue and cover the whole with the paper tape. However for the corrugated pipe with diameter of 34.5 mm, we followed the same method without glue. We used the paper tape cut as thin as the thermocouple and covered the hollow surface by ensuring the thermocouple is in contact with the surface. We also covered each hollow surface with sewing rope in order to ensure the thermocouple well placed.

Figure 3.21. Thermocouple placed on the coated tape

In heat transfer experiments, the perfect thermal isolation has always been food for thought. Thermal resistance of the isolation substance is at paramount importance to prevent heat dissipation to environment. Thus, we tested the corrugated pipe firstly letting no air through but heating the pipe only. We measured temperatures on the surface of the

pipe and desired them to be same value at each thermocouples placed along pipe surface. However, we discovered the temperature readings increasing as we insulated pipe further. Additionally, we placed small pieces of insulation substance on which thermocouples are placed to keep the each temperature reading stable and consistent before we fully insulated the corrugated pipe. Moreover, we measured the heat loss through pipe with respect to temperature readings subtracted from the infinite temperature value (temperature test room which is kept around 21℃). We fit these obtained data in the use of calculating net heat flux (which is obtained by subtracting supplied heat flux from the heat dissipated for each thermocouple) for the forced convection test in corrugated pipe. As mentioned before, the fitted heat loss data is a function of temperature readings and each reading of forced convection differs from each other, we regulated those dissipated heat values as a function of local placement of temperature readings (thermocouples). We used this function to calculate the mean temperature in corrugated pipe derived for non-constant heat flux case. We will come to that in more detail in Section 4.5.
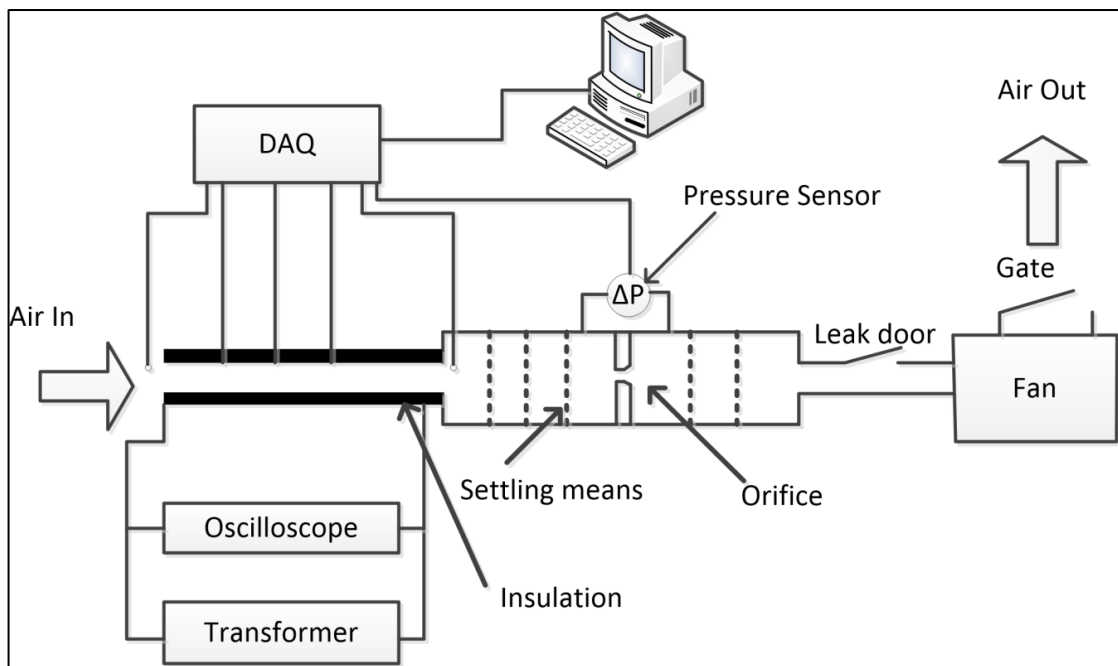
Figure 3.22. Schematic of experimental setup for heat transfer tests

In other words, undesired heat dissipation in the forced convection test has been taken into account while calculating local heat transfer coefficient and Nusselt number. This procedure stem from the heat dissipation being locally along corrugated pipe surface which

corresponds to non-heat flux case. Moreover, we calculated net flux accurately enough by calibrating test setup in terms of heat loss but we had issues on the power supply used in test setup.

Figure 3.23. Transformer used in forced convection heat transfer tests

The transformer in the picture above is used to supply current to corrugated pipe. However, the transformer supply pulsating current rather than alternating. Therefore, we used an oscilloscope to measure the square root voltage difference on the corrugated pipe to calculate power supplied. Anyway, we measured the power supplied with reasonable accuracy when we compared it with the result of convected heat by air through corrugated pipe. As we increase the supplied power further, we noticed that this accuracy deteriorates but still remains in the reasonable range such as around 0-15 % regarding the corresponding result of convected heat through pipe.
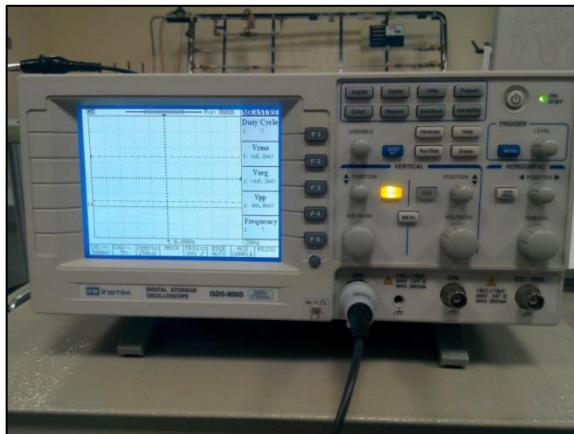
Figure 3.24. Oscilloscope used in forced convection heat transfer tests

Heat loss measurement thus, the net heat flux through pipe is crucial due to determination of heat transfer coefficient and Nusselt number. Hence, we considered electrical resistance of the pipe because we lack a well calibrated ampermeter to measure very high current values. Therefore, we prepared a test set up that includes a DC power supply, Agilent's Multimeter which measures low currents and another Multimeter measuring the voltage value through pipe to determine electrical resistance of the pipe. We illustrated the circuit schematically in Figure 3.25.
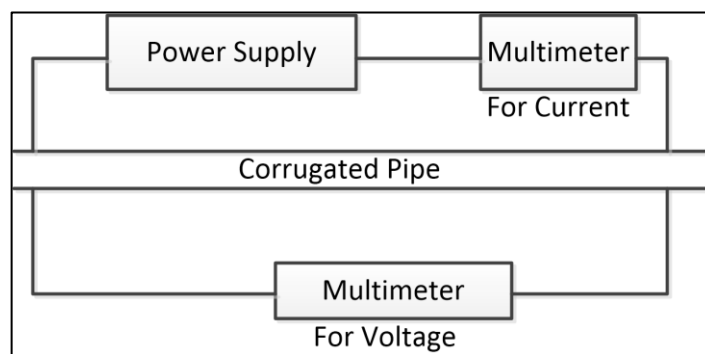
Figure 3.25. Schematic of pipe resistance determination tests

In test set up built per the schematic above, we applied low current by DC power supply (Figure 3.27.) through corrugated pipe which is measured by one of the multimeter (Figure 3.26.) and the another gauges the voltage difference on the corrugated pipe due to current supply. As a result, we determine the pipe resistance for a specified wall temperature of the pipe.

Figure 3.26. Multimeter used in pipe resistance tests

Figure 3.27. DC power supply used in pipe resistance tests

We followed a test procedure to measure electrical resistance of the pipe as a function of wall temperature of the pipe. First we heated the pipe to desired temperature with transformer. Then, we activated DC power supply (Figure 3.27.) instead of transformer to supply low DC current. As we regulated the test set up defined in Figure 3.25., we read and recorded the instantaneous current and voltage values on multimeter as the temperature decreases. Thus, we were able to obtain electrical resistance of the corrugated pipe (obtained by dividing the voltage to current readings) as function of surface temperature of corrugated pipe. (See Figure 3.28.)
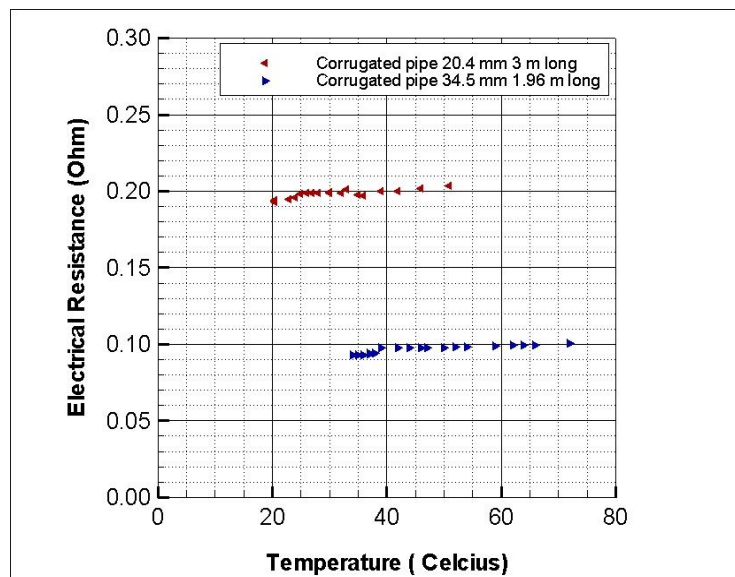
Figure 3.28. Pipe resistance values changing with respect to surface temperature for the pipes 20.4 mm and 34.5 mm

We already knew the local temperature of corrugated pipe differs along the surface; we derived the local supplied heat in terms of local electrical resistance of the pipe;

$$P_{supply}(x) = \frac{V_{rms}^2}{R(x)} \qquad (3.10)$$

However, we acquired almost same temperature values in the test of heat loss determination, so the supplied power is independent of local configuration readings thus, supplied heat flux and heat loss is assumed to be constant along the pipe for the case of corrugated pipe with perfect thickness. The supplied power for heat loss determination case is derived as function of temperature readings subtracted from the infinite temperature value due to electrical resistance of the corrugated pipe being function of surface temperature.

$$P_{loss}(T) = \frac{V_{rms}^2}{R(T)} \qquad (3.11)$$

The derivation of equations for local observation of heat transfer coefficient and Nusselt number is displayed in Section 4.5.

4. RESULTS

4.1. CALIBRATION

A smooth PVC pipe with a diameter of 16.28 mm ± 0.19 mm is tested over a range of Reynolds number from 800 to 13300. The flowrate is calculated from pressure difference measurement on the settling chamber which is 0.33×1×0.33 m. Discharge coefficient (C_d) is taken 0.60 as mentioned in 3.3. The flowrate is determined from Equation 3.2.

The orifice plates have diameters of 9.92 ± 0.02 mm, 14.07 ± 0.03 mm, 20.17 ± 0.07 mm and 30.02 ± 0.14 mm. The discharge coefficient for laminar region may change between 0.6 and 0.61 and for turbulent region it remains in a shorter range such as 0.6 − 0.605. These rate intervals are the tops and the least so those bring less than 2 % uncertainty for turbulent region and less than 4 % uncertainty for laminar region to whole system. However, the uncertainty rate for the pipe diameter has the most effect on the system with almost 6 %. The least uncertainty is from the orifices of 9.92 mm and 14.07 mm in diameter with less than 1 % but the other orifices are with almost 2 % uncertainty. Briefly, calibration test system has a total uncertainty of around about 6 % for turbulent region and 7 % for laminar region. We calibrated test setup due to Darcy friction factor formulae for laminar flow and Colebrook correlation for turbulent flow. Therefore, the uncertainty analysis covers friction factor and Reynolds number. We neglected temperature measurement uncertainty because it does not sway significantly. The measured friction factor differs around 1 to 3 % for the orifice of 14.07 mm in diameter and nearly 5 % for the orifice of 9.92 mm in diameter from the calculated from Darcy's formulae (Equation 2.8).

We already mentioned the uncertainty of the system for laminar region was 7 % and that covers the error % for both orifices. We measured the friction factor for the orifices of 20.17 mm and 30.02 mm in diameter in turbulent region due to Colebrook correlation (Equation 2.9) as around 1 % for both the former and later. We also obtained and calibrated the friction factor in turbulent region for the orifices 9.92 mm and 20.17 mm. We found the friction factor deviates from the calculated one at almost 2 % for the former

and 5 % for the later at low Reynolds number in the turbulent region. The uncertainty rate for the turbulent region covers the deviations with around 6 % and 7 % for laminar which means the measurements are in the safe zone for both laminar and turbulent region.

We calculated the friction factor from Darcy-Weisbach Equation (Equation 2.7) by measuring pressure loss and flow rate that corresponds to mean velocity in the pipe. We plotted the calibration results of friction factor and Reynolds number in a log scale and fitted them with respect to Equation 2.8 and Equation 2.9. As one can see in Figure 4.1, the results for all orifices satisfy both equations very well. The measured friction factors in the laminar zone begin to deviate slightly from the Darcy formulae from 1600 to 2000 because of the transient effect can be observed here clearly. We already know from dye trace experiments that the flow begin to pulse even if it is rare. Therefore, we expected the results to slide out of the trend.

The mean velocity through the pipe can be estimated from the measured flow rate in Equation 3.3. When we substituted the Equation 3.3 in to Equation 2.7, we rewrote equation shown in Equation 3.4;

As one can see why the measured friction factor pipe is so sensitive to the pipe diameter in Equation 3.4 and we also considered and rewrote the Reynolds number equation as it was in Equation 3.6

It can be clearly seen in Equation 3.6 and Equation 3.6, the pipe diameter measurement uncertainty for the Reynolds number determination influence less than for the friction factor determination. We already found that the uncertainty was approximately 2 % for the former whereas; it was around 6 % for the later. We observed friction factor as a function of Reynolds number found quite satisfying with results available in Moody Chart. (See Figure 4.1)
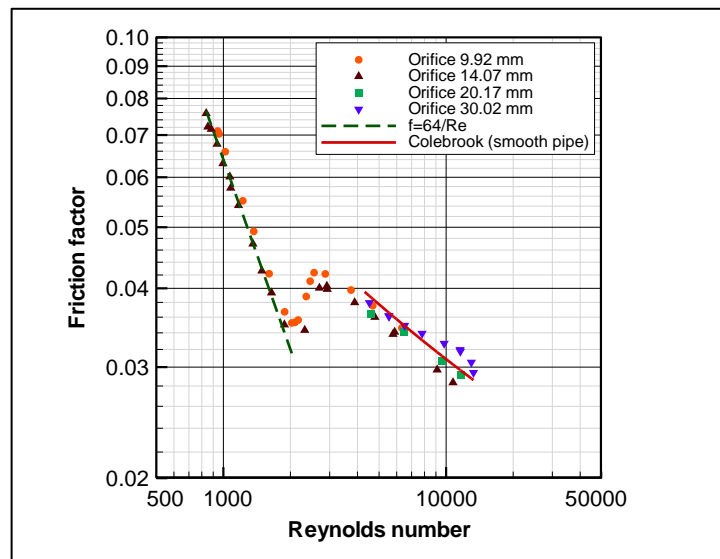
Figure 4.1. Calibration results of experimental results in regard to friction factor in smooth pipe and Reynolds number

We further checked the test setup with another aspect whether it worked right. We plotted the pressure loss along the pipe via mean velocity. Theoretically, the pressure loss increases linearly in the laminar zone. The power indices on the velocity must lie between 1.7 and 2. Our results satisfied that theory by Hagen successfully with the power index found 1.77 as appears in Figure 4.2.
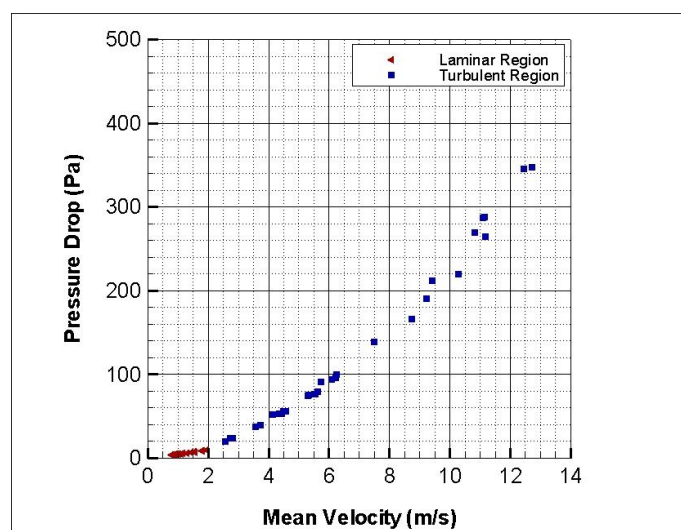
Figure 4.2. Calibration results of experimental results in regard to pressure loss with respect to mean velocity in smooth pipe

As per Figure 4.1 and Figure 4.2, we validated whatever it is inserted to the experimental set up works correctly with 6-7 % error rate due to determination of C_d and dimensions of orifices and the pipe.

4.2. FRICTION FACTOR IN CORRUGATED PIPES

We conducted our experiments with four corrugated pipes different in diameters and corrugation sizes. Our results showed the friction factor is much higher than the smooth pipe for turbulent region whereas; they are same as for the smooth pipe in the laminar zone. At the first glance, the friction factor is higher in the turbulent zone because of high pressure fluctuations due to corrugation. However, the corrugations have no effect on the friction factor in the laminar zone. Interestingly, the critical transition Reynolds number from laminar to turbulence varies for each pipe. We observed the corrugation size affects this critical Reynolds number. We specified the crest width must be the reason which would play a role of roughness. We define the crest width to corrugated pipe inner diameter and named it as "roughness factor". Ahn et al. [11] approached this in the similar way with the dimensionless corrugation size which basically involves the cavity height (H/D). As per Figure 4.3, the friction factor is higher for a pipe with higher roughness factor (the ratio of the crest width to pipe diameter).
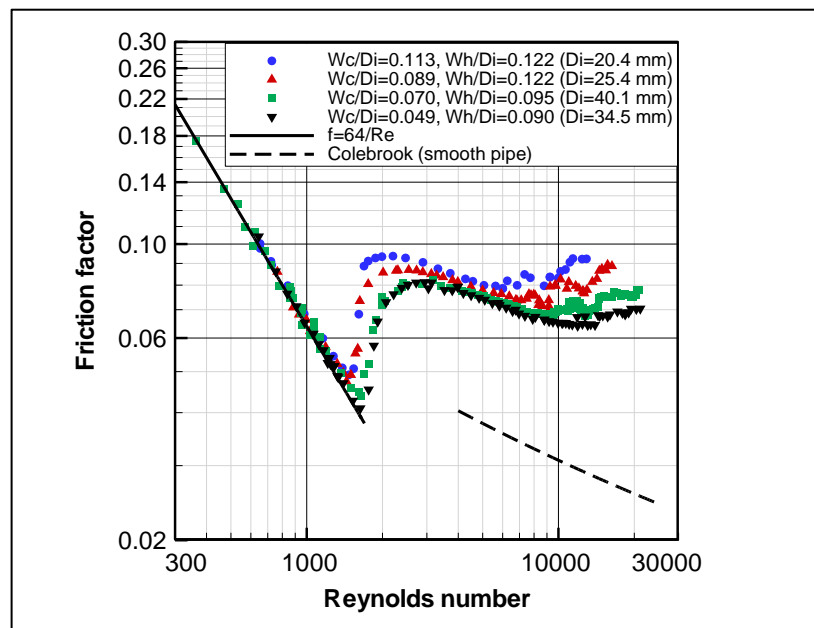
Figure 4.3. Experimental results of friction factor with respect to Reynolds number

Although the roughness factor is not formulated as same as what Ahn et al. [11] introduced, it corresponds to their dimensionless number. We found that as the roughness factor increases, the friction factor increases too. This satisfies the same theory for rough ordinary pipes with compared to smooth ones. Ahn et al. [11] presented the dimensionless corrugation size equation as it follows below;

$$\varepsilon^* = \frac{(D_o - 2t - D_i)}{2D_i} \tag{4.1}$$

We plotted our results by classifying with the dimensionless corrugation size (ε^*) in Figure 4.4 as Ahn et al. [11] suggested. We witnessed the friction factor can be compared well with the dimensionless corrugation size which they fail. The dimensionless corrugation size can be also regarded as the surface roughness because it simply involves the cavity height and pipe diameter within.
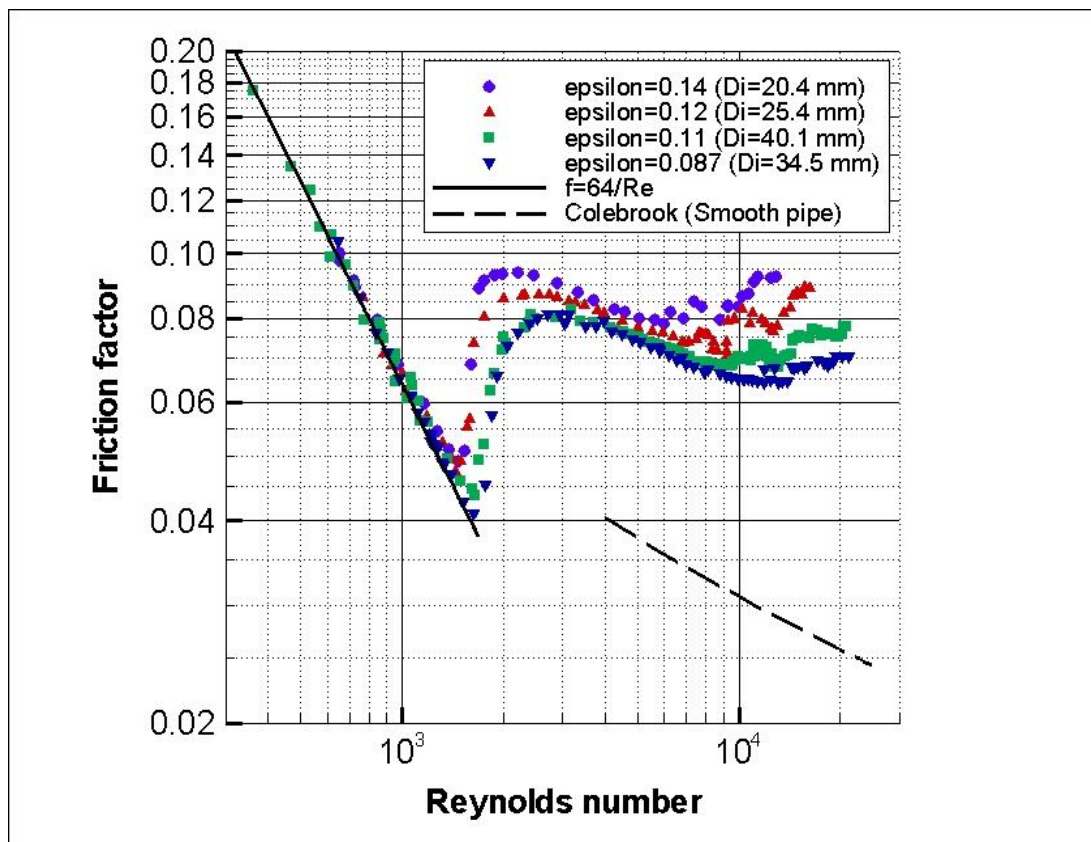
Figure 4.4. Experimental results of friction factor with respect to Reynolds number
in corrugated pipes classified with dimensionless corrugation size

We also demonstrate the friction factor in the fully turbulent region with respect to dimensionless corrugation size with results available from our experiments in Figure 4.5. We observed the friction factor is directly proportional to the dimensionless corrugation size (ε^*). Thus, it is safe to say, increase in the dimensionless corrugation size roughens the inner surface of corrugated pipe.
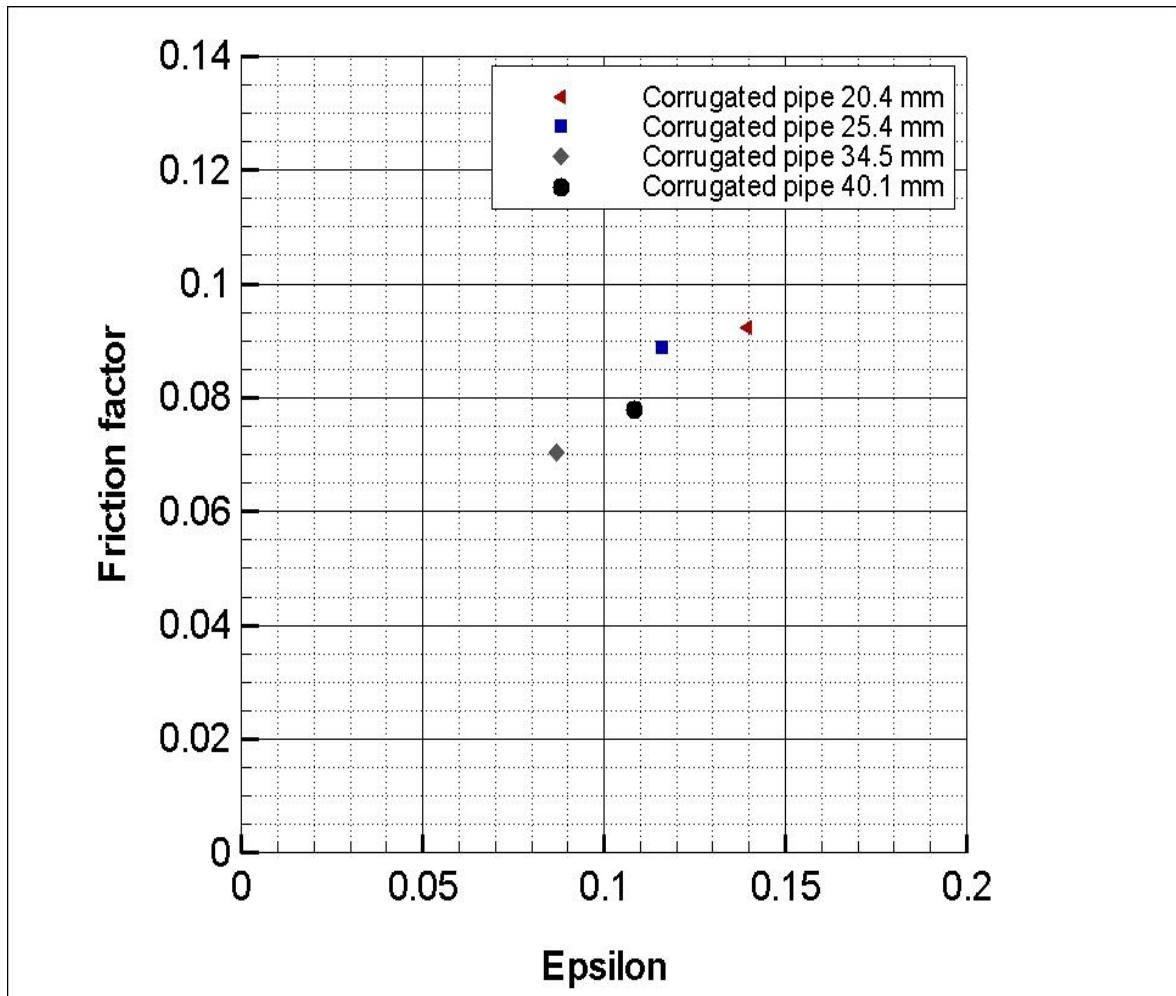
Figure 4.5. Experimental results of friction factor with respect to dimensionless corrugational size in corrugated pipes tested (Re=19000)

Vicente et al. [12] also came up with a dimensionless parameter for roughness which they name as the severity index (Equation 4.2). Their dimensionless value mainly comes down to the cavity height. We also investigate our findings with the severity index suggested by Vicente et al. [12]. They claimed the friction factor increases as the severity index increases. We witnessed pipes with 25.4 and 40.1 mm in diameters do not fit the

observation. The reason would be either pitch length having no influence on pressure losses thus friction factor or the axisymmetric corrugated pipe they used in their experiments.

$$\varphi = \frac{H^2}{P_t D_i} \tag{4.2}$$

Breuer et. al. [3], Vicente et al. [12] and Unal et. al [9-10] tried to investigate the critical transition Reynolds number where flow leaves the laminar region. Nyarko et al. [13] and Stel et al. [8] also mentioned that transition Reynolds number is below 2000 but it was not localized exactly. Vicente et al. [12], who investigated spirally corrugated pipes, reported the cavity height to diameter ratio accelerates the transition from laminar to turbulent region. However, we witnessed from the experiments on friction factor with corresponding Reynolds number, corrugated pipes with 20.4 and 25.4 mm in diameter have the same ratio of hollow width to pipe diameter and leave the laminar zone at almost same Reynolds number. As can be seen in Figure 4.6, our results indicates the friction as function of Reynolds number in this critical region classified with the ratio of the hollow width to pipe diameter where transition from laminar to transient region occurs . We attributed this occasion to the vortex instability. If the cavity width gets larger, vortexes in the cavities eject to bulk flow easily creating more instability in the pipe.
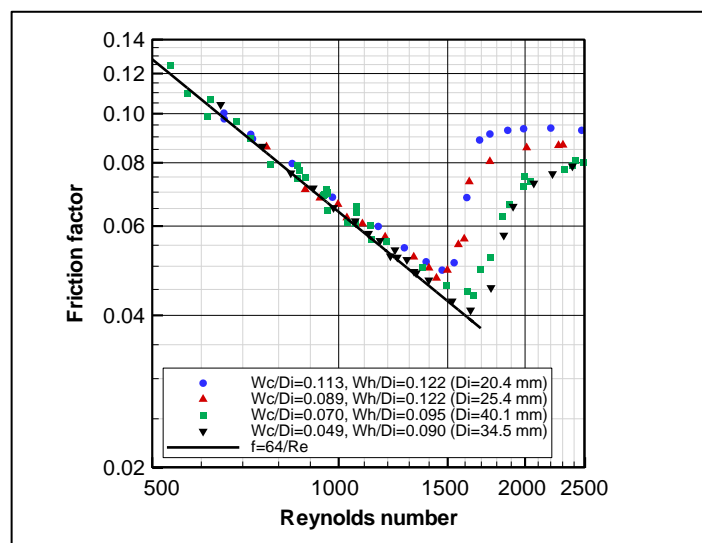
Figure 4.6. Determination of critical transition Reynolds number based on pipe diameter

We observed that flow leaves the laminar region more quickly for the pipes with higher the ratio of hollow width to pipe diameter. As mentioned before, flow in the pipes with diameter of 20.4 and 25 mm leave almost at same Reynolds number. This would indicate increase in the ratio of hollow width to pipe diameter accelerates the transition from laminar to transient region. Moreover, we found the critical Reynolds number based on cavity height as 220, 180, 150 and 190 for the pipes with diameter of 20.4, 25.4, 34.5 and 40.5 mm respectively. Breuer et al. [3] confirms that by saying the flow becomes turbulent $Re_{cr} > 200$. We plotted the friction factor against the Reynolds number based on cavity height in Figure 4.7;
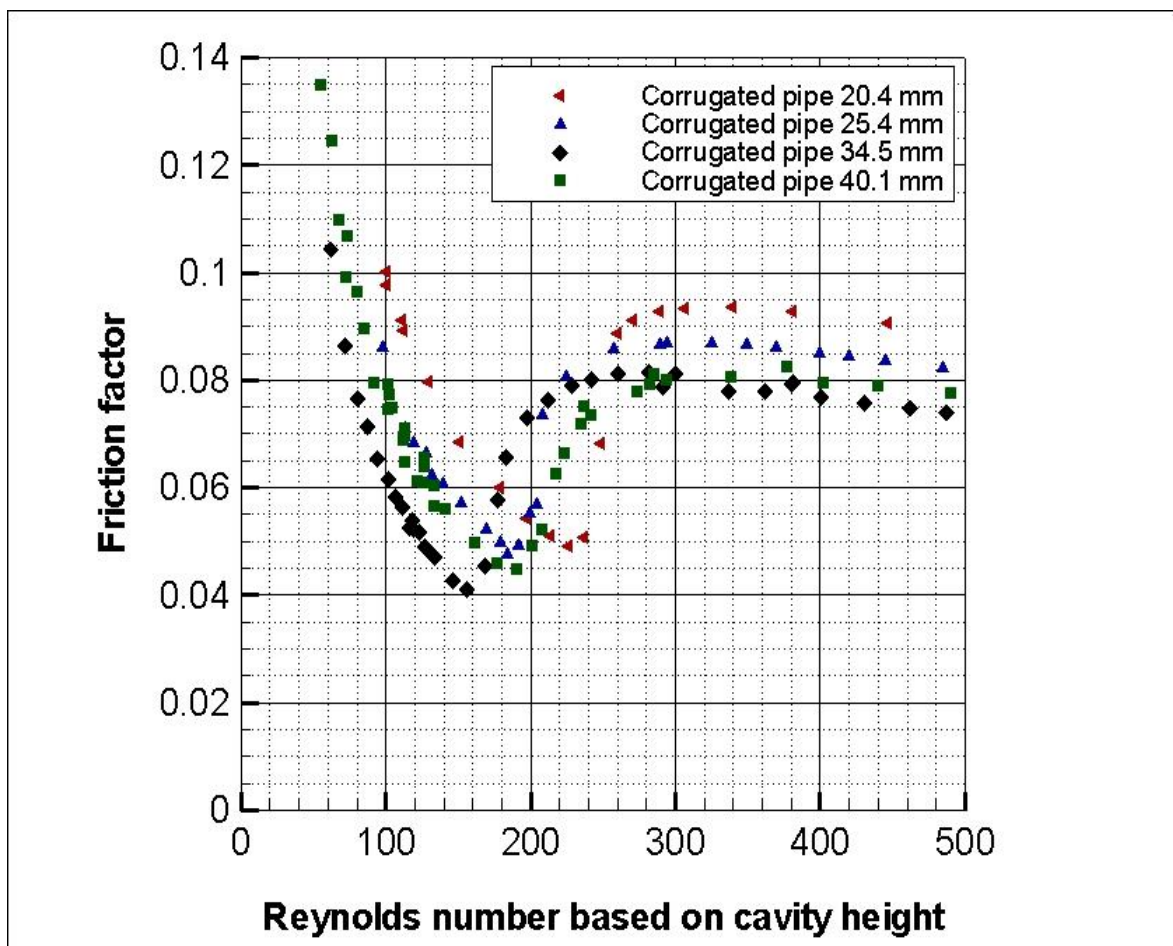
Figure 4.7. Determination of critical transition Reynolds number based on cavity height

Unal et al. [9-10] proved in their experiments that the flow is stable, steady and two dimensional at Reynolds number below 1500. They reported there are rare pulses of vortexes inside grooves beyond Re=1200. These rare pulses become more frequent when

Re >1500. We see these pulse effects resulting in deviation from Darcy's formulae trend, particularly for the pipes 20.4 and 25.4 mm, in Figure 4.6. We also deduce these vortexes escaping from the groove and ejecting to the core flow are the reason why the pressure loss due to turbulence intensity higher than for smooth pipes thus, the friction factor is much higher than usual pipes. Regarding Figure 4.8, we observed these high pressure fluctuations in a regular pattern in Reynolds number 20500 for the pipe 40.1 mm and compared it to data taken in laminar region by using with same pressure transducer. (ORASS 100 Pa)
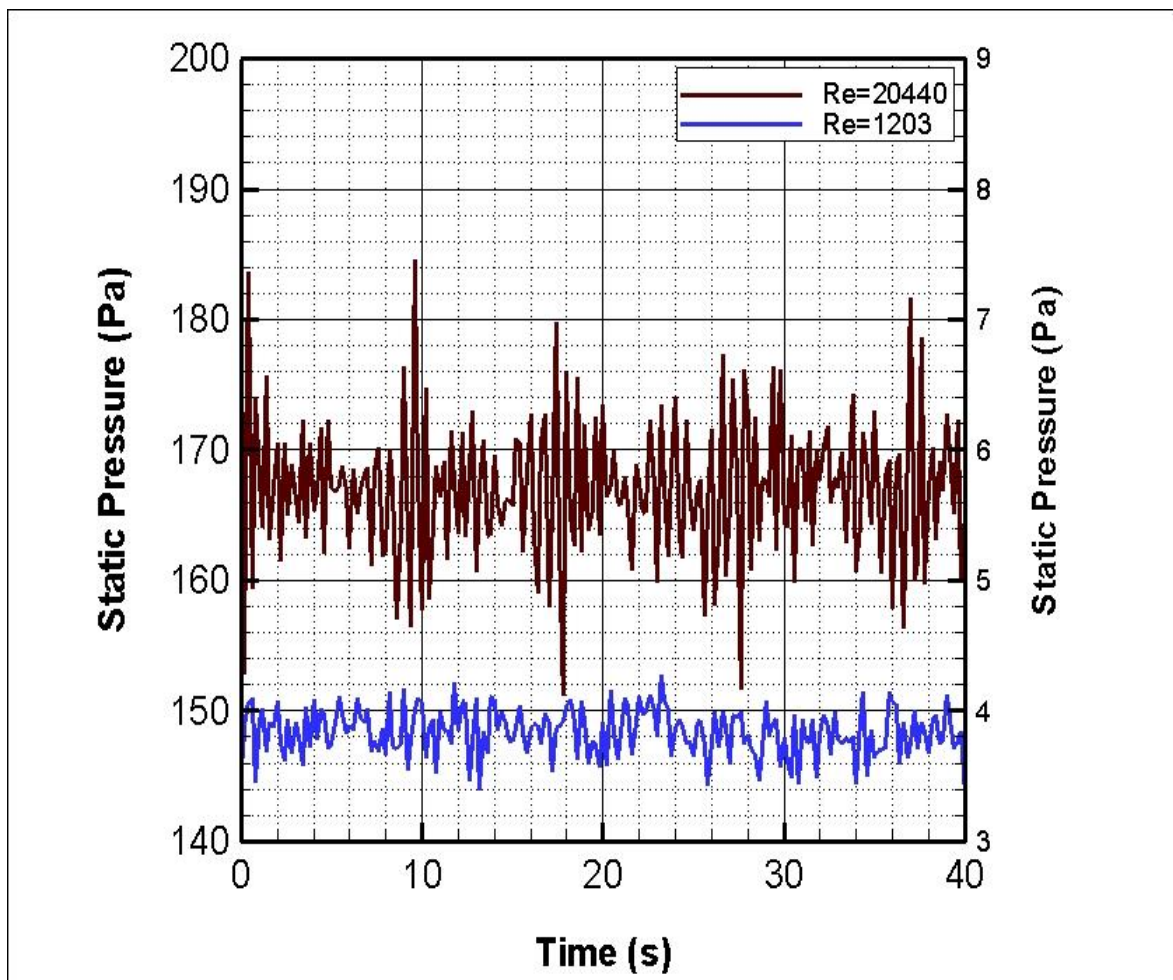
Figure 4.8. Pressure loss measurement via time for corrugated pipe 40.1 mm in diameter

Unal et al. [9-10] also reported that below the critical Reynolds number, the vortexes in the cavities are stable and does not influence the bulk flow which results in laminar flow. As expected, no high fluctuation is observed for a measurement in laminar zone in Figure 4.8.

Stel et al. [8] suggested that the friction factor increases as the groove length increases regardless of groove height. Our findings cannot answer this because each corrugated pipe used in the experiments has different cavity height and width. Thus, increase in friction would be caused by either groove width or height. However, we came across the cavity width to pipe diameter ratio are almost same at 0.12 for the corrugated pipes 20.4 mm and 25.4 mm. As mentioned for the Figure 4.6, we observed the flow in these pipes leave the laminar zone at almost same Reynolds number. This would explain the reason. Figure 4.9 demonstrates this critical transition from laminar to turbulent Reynolds number based on pipe diameter with respect to cavity width to pipe diameter ratio for each pipe.
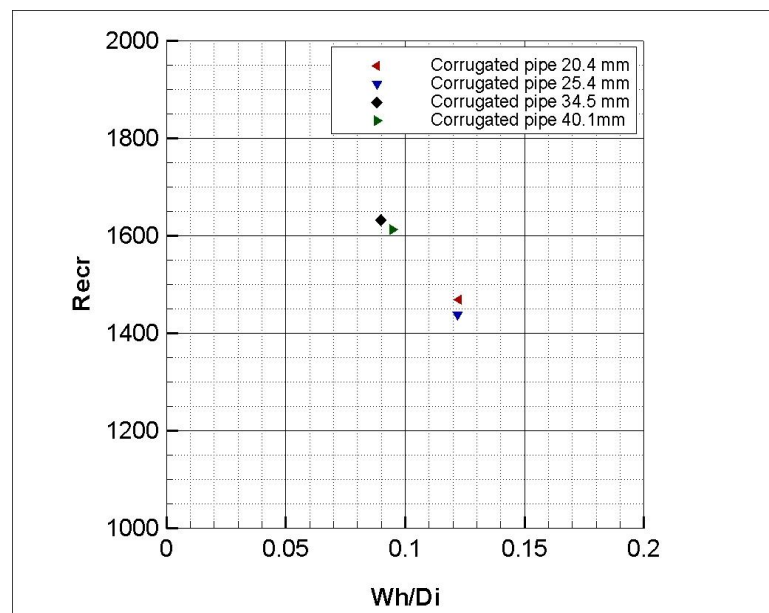
Figure 4.9. Critical transition Reynolds number with respect to W_h/D_i

Although Figure 4.9 is not precise, one can say that the transition Reynolds number depend on the cavity width. Stel et al. [8] explained that if the cavity width increases, vortexes in the cavities become less stable therefore more influence on the core occurs. This would reveal why pressure loss increases that results in higher friction factor. Accordingly, Nabikoglu and Manders et al. [15] introduced the cavity height to width ratio (H/W_{hollow}) determines whether the cavity height affects the flow or not. They suggested that if this ratio is above 0.5, the flow characteristic is independent from the cavity depth. We will come to this next section in more detail. As long as our cavity height to width ratio for each pipe is above 0.5, the cavity depth is out of consideration.

4.3. VORTEX SHEDDING FREQUENCY AND STROUHAL NUMBER

We observed in our experiments that the Strouhal number is almost constant in a narrow range in regard to Reynolds number. However, Strouhal number seems to be decreasing in a short range increasing Reynolds number till the vortex shedding frequency shifts to the next acoustic mode. As shown in Figure 4.10, we found the Strouhal numbers based on crest width are 0.25, 0.22, 0.17 and 0.19 for the corrugated pipes with diameter of 20.4, 25.4, 34.5 and 40.1 mm respectively.

$$St = \frac{FW_c}{U_\infty} \tag{4.3}$$

Where f is the vortex shedding frequency, W_c is the crest width and U_∞ is the mean flow velocity.

The Strouhal number is related to the characteristic of the pressure waves which is an outcome of how fast the vortices in cavities are convected to the bulk flow. In other words, the vortex shedding is coupled with the pressure oscillation. Therefore, the frequency of the pressure oscillation and thus the Strouhal number are dependent on the bulk flow and the shape of the corrugation which affect the vortex shedding. In the present study the crest width is used for the characteristic length of the Strouhal number. As can be seen in Figure 4.10, Strouhal number is higher for the pipes with larger ratio of crest width to pipe diameter.
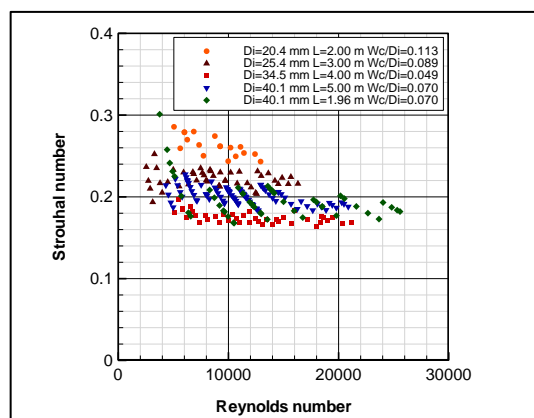
Figure 4.10. Strouhal number via Reynolds number for the pipes 20.4, 25.4, 34.5 and 40.1 mm.

The Strouhal number is plotted against the Reynolds number in Figure 4.10. In general, all Strouhal numbers for corrugated pipes with different dimensions lie within the narrow band of 0.16 to 0.3 over the wide range of Reynolds number. The average Strouhal numbers for the corrugated pipes with the diameters of 20.4, 25.4, 34.5 and 40.1 mm are approximately 0.25, 0.22, 0.17 and 0.19, respectively. This is consistent with what is known in the literature: That is, the low frequency attributed to the instability of the wake behind the corrugation is independent of Reynolds number, and in this case the Strouhal number related to the frequency is approximately equal to 0.2.

When only the peak-whistling Strouhal number is examined in Figure 4.11 instead of all Strouhal number data in Figure 4.10, it is easier to see that the peak-whistling Strouhal number is a slightly decreasing function of Reynolds number for a given corrugation geometry. More importantly, it transpires that the larger ratio of the crest width to pipe diameter, the higher Strouhal number. This observation leads to the next discussion in Figure 4.12.
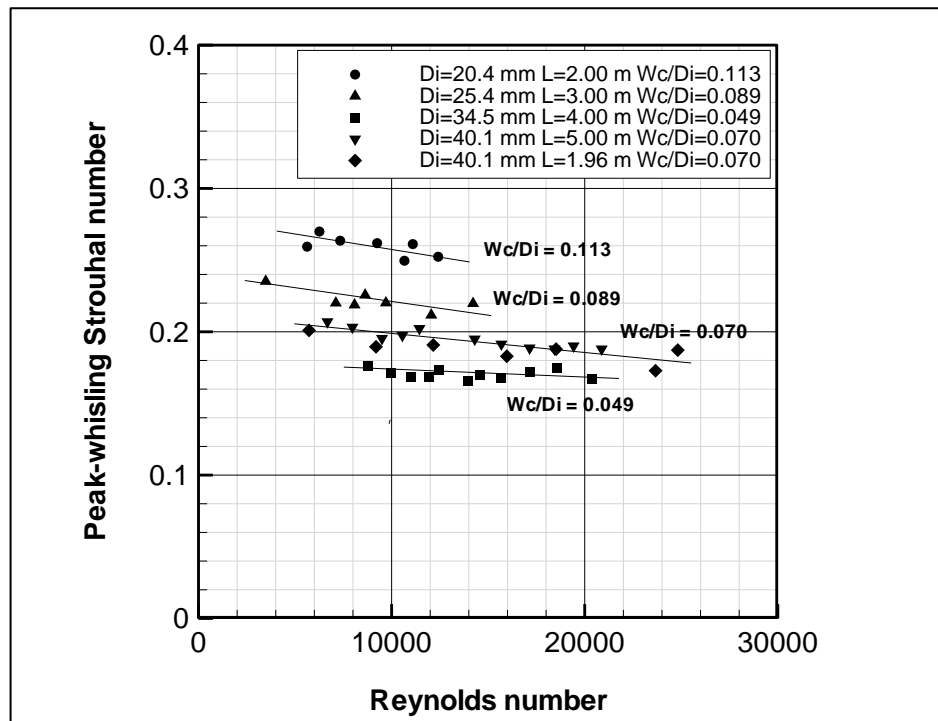
Figure 4.11. The peak-whistling Strouhal number (based on the crest width) as a function of Reynolds number. The peak-whisling Strouhal number appears to depend on the ratio of the crest width to the pipe diameter.

Popescu et al. [14] reported that according to their simulations, the Strouhal number based on the pitch length is almost constant and 0.61 which corresponds to 0.25 for Strouhal number based on crest width for 25.4 mm pipe diameter. In Figure 4.13, we can see our result for the same pipe diameter and corrugation sizes almost agrees with their result. They witnessed that a corrugated pipe with a longer pitch has lower frequency and Strouhal number. They related this to the characteristic of the pressure wave is an outcome of how fast the vortexes convect to the core flow. It is the flow and shape of the corrugations which determine the characteristic of the pressure waves. When we analysed our Strouhal number based on pitch length and pitch length to pipe diameter ratio, no clear relation is observed. However, we witnessed a clear correlation with the crest width used as characteristic length. Nakiboglu et al. [15] introduced confinement ratio which is pipe diameter divided by cavity width ratio. This ratio is actually suggested by Elliot et al. [17] but they restored it. They attributed the alteration of the confinement ratio to change in the velocity profile. They reported and correlated increase in the Strouhal number to decrease in the confinement ratio. Unfortunately, it did not also conform to our results with the hollow width taken as characteristic length. As mentioned above, we came across the crest width to pipe diameter ratio makes sense with the Strouhal number. Therefore, we restored the confinement ratio assigned to the pipe diameter to hollow width ratio and correlated it with Strouhal number in Figure 4.12.
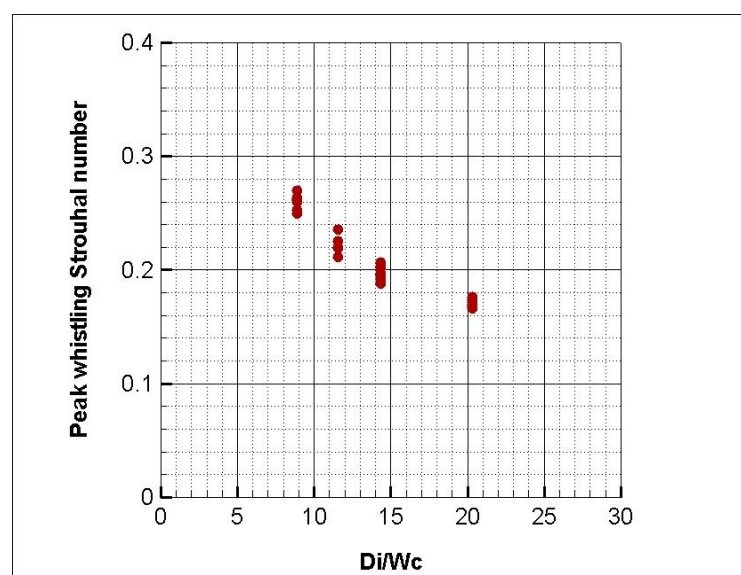
Figure 4.12. The peak whistling Strouhal number in terms of D/W_c

We also investigated our results with the result in the literature available. We observed that our results for peak whistling Strouhal number satisfy with the results presented by Popescu et. al. [14], Debut et al. [19] and Nakiboglu et.al. [15] in Figure 4.13. We propagated their results for Strouhal numbers to the Strouhal numbers based on the crest width to compare with our results. (It may be noted that Nakiboglu et al. [15-16] uses the sum of the hollow width (W_h) and a half of the crest width (W_c) as the characteristics length in their publication).
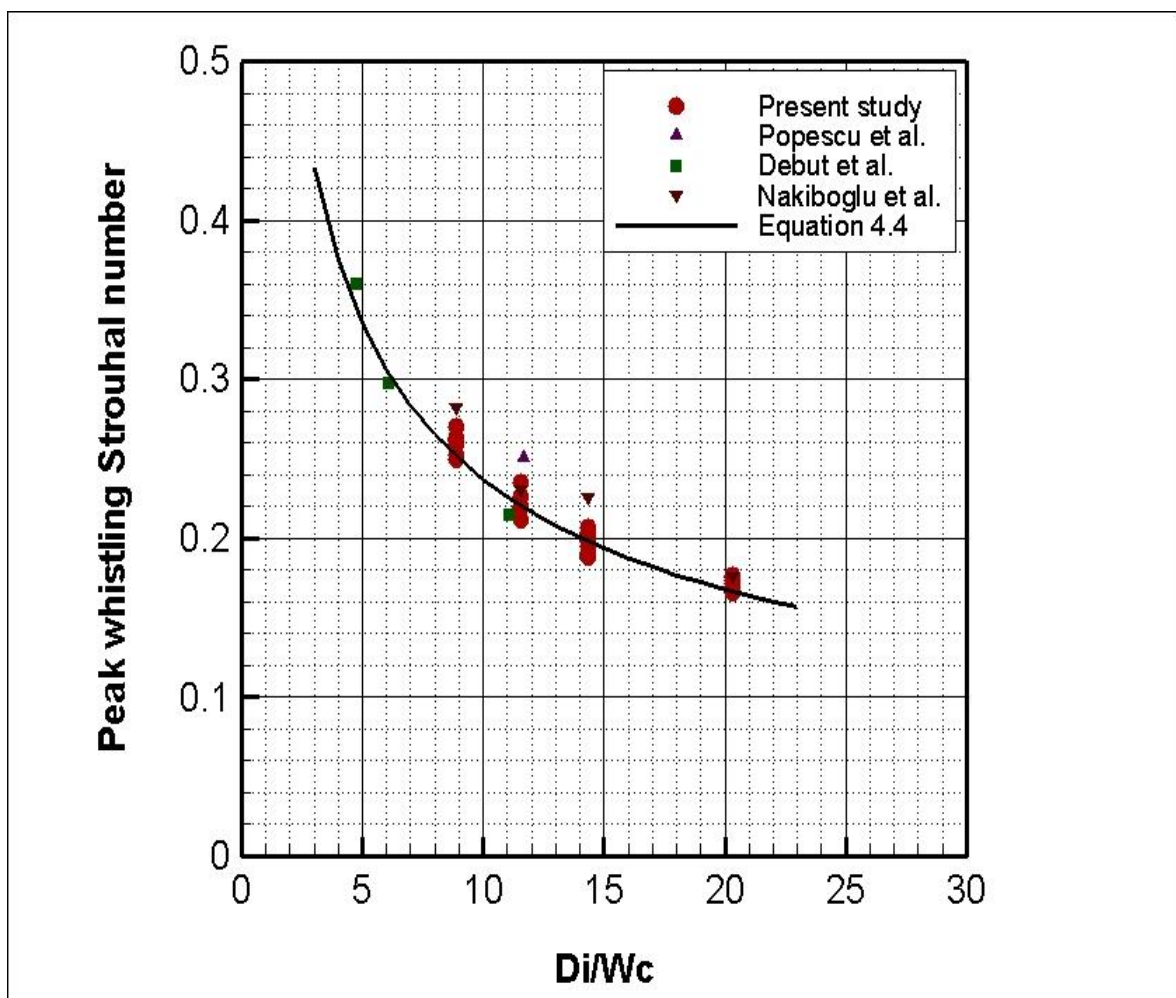
Figure 4.13. The peak whistling Strouhal number in terms of D/W_c with comparison of Popescu et. al. [14], Debut et. al. [19] and Nakiboğlu et al. [15]

The peak whistling Strouhal number (St_{pw}) is the value at which the fluctuation amplitude is the maximum in the same resonant mode. As mentioned at beginning of this section, the Strouhal number decreases in an acoustic mode in which range the vortex shedding

frequency is almost constant. The peak whistling Strouhal number corresponds to the middle values in this range. As can be seen in Figure 4.10, this range is large for low Reynolds numbers.

Figure 4.13 presents the peak-whistling Strouhal numbers as a function of the ratio of the pipe diameter to the crest width. Note that the crest width (W_c) is used for the characteristic length for the Strouhal number for all data in Figure 4.13. It is apparent that the peak-whistling Strouhal number decreases as the ratio of the pipe diameter to the crest width increases. The data of the present study are well compared with Popescu et. al. [14], Debut et. al. [19] and Nakiboğlu et al. [15]. Here in Figure 4.12 and Figure 4.13, we attempt to correlate the peak-whistling Strouhal number with the ratio of pipe diameter to the crest width within the scattering of 5% as follows.

$$St = (0.76 \pm 0.05) \left(\frac{D_i}{W_c}\right)^{-(0.5 \pm 0.01)} \tag{4.4}$$

Nakiboglu et al. [15] are the only who mentioned hill width must involve in the characteristic length and the correlation. They referred to Elliot et al. [17] and claimed that half of the crest width must be taken into account due to its determination over a distance of the velocity fluctuations. They took characteristic length for the Strouhal number definition as sum of the cavity width and half of the crest width. However, we took solely the crest width because we were only able to correlate the peak whistling Strouhal number based on crest width (Equation 4.4). Besides, we must recall the Popescu et al. [14] suggested longer pitch length brings about lower frequency thus Strouhal number. As far as the pitch length is sum of the hollow and crest width, we have two options which sway the Strouhal number. For the first time, Nakiboglu et al. [15] reported that the crest width determines the travel time of perturbation which leads to the vortex shedding frequency. However, they defined the characteristic length by just adding the half of the crest width to hollow width. More importantly, Nakiboglu et al. [16] claimed if the cavity height to the width ratio is larger than 0.5, the oscillation amplitude and Strouhal number is independent from the cavity depth. As our cavity height to width ratio for each pipe is above 0.5, we assume there is no of cavity depth. Moreover, we found Strouhal numbers based on hollow width for each pipe are almost same for the pipes with same cavity width such as for the

pipes 25.4 and 34.5 mm at $St_{pw}=0.3$. However, these are different for pipes 20.4 and 40.1 mm and there is no significant and enough data that we were unable to observe. Furthermore, we observed the vortex shedding frequency follows the same trend for the pipes 25.4 and 34.5 mm as can be seen in Figure 4.14.
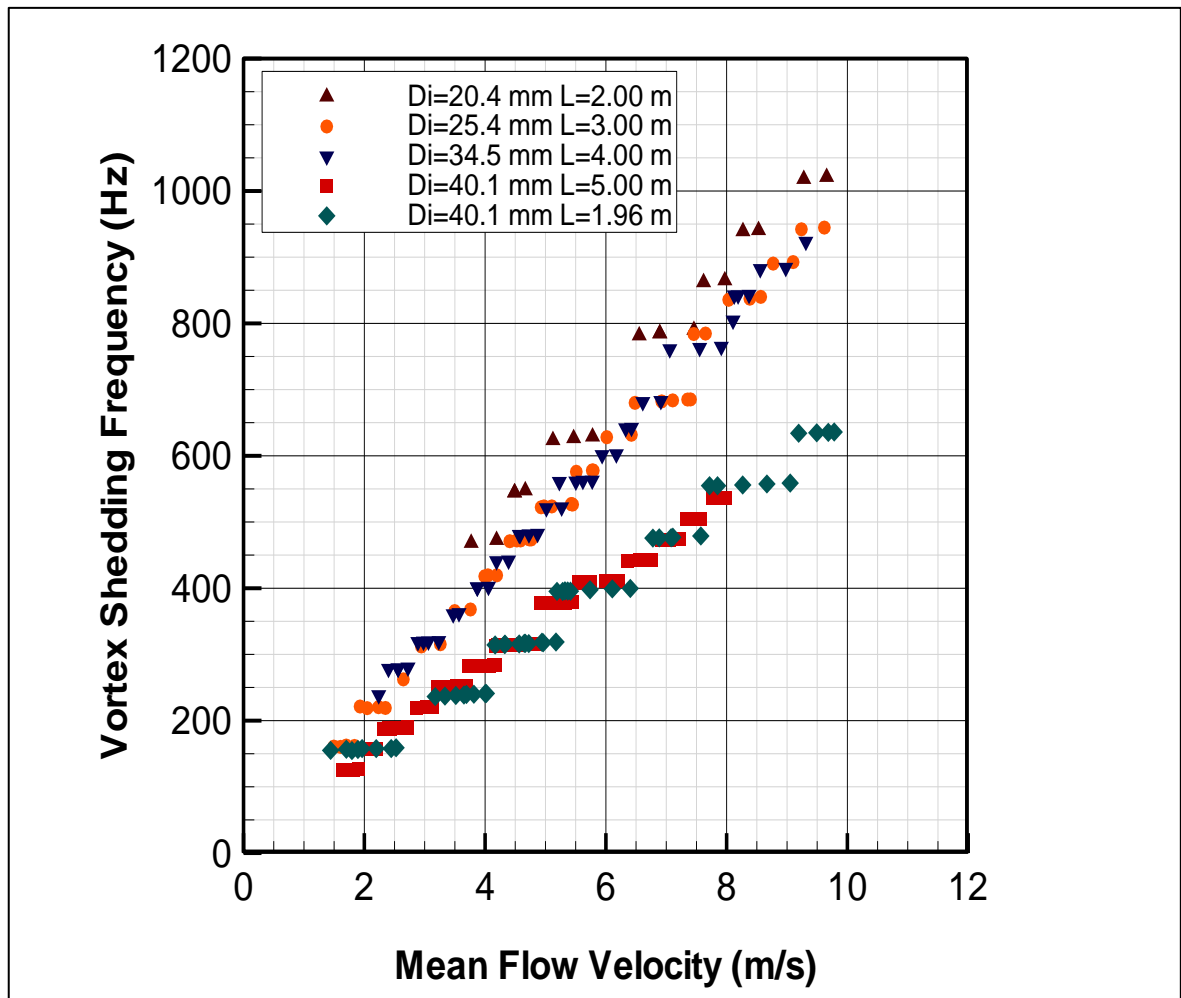
Figure 4.14. The vortex shedding frequency as a function of the mean velocity

The vortex shedding frequency which is obtained by measuring the whistling frequency of the pipe is plotted against the mean flow velocity in Figure 4.14. In general, the vortex shedding frequency increases with the mean flow velocity. More detailed examination shows that the vortex shedding frequency increases stepwise with the mean velocity as an acoustic mode shifts upward in a stepwise manner with the increasing mean velocity. The onset velocity that is defined as the minimum fluid velocity at which the whistling occurs is also examined in Figure 4.14. The onset velocities of the pipes, 20.4, 25.4, 34.5 and 40.1

mm in diameters, are measured to be approximately 3.8, 1.5, 2.24 and 1.5 m/s, respectively, which correspond to the Reynolds numbers of 5100, 2600, 4000 and 5100, respectively. Those Reynolds numbers appear to represent the beginning of turbulent region in the corrugated pipes as shown in Figure 4.3. According to Unal et al. [9-10], in laminar flow, the vortex inside the cavity is stable and has no interaction with the bulk flow, but it starts being ejected from the cavity to the bulk flow as the flow enters transition region. For turbulent flow, there is vigorous interaction between vortices in the cavities and the bulk flow. In other words, it is not possible to have the whistling in laminar flow because no vortex is ejected from the cavity to the bulk flow. For turbulent flow, however, the whistling occurs as the resonance between vortex shedding and acoustic wave in the pipe takes place. Therefore, it is obvious that the onset velocity must correspond to a Reynolds number which represents the beginning of turbulent flow. In the present study, due to the limited quality of the microphone used to measure the whistling frequency, the onset velocity might not have been determined accurately but it still explains the connection between the onset velocity and turbulence.

Figure 4.14 also shows the effect of the pipe length on the onset velocity. Two different lengths, 1.96 m and 5 m in length, of the pipe with the same diameter of 40.1 mm are employed in the test. Both pipes have the same onset velocity as shown in Figure 4.14. Therefore, it is evident that the pipe length has no effect on the onset velocity.

Furthermore, we validated our experimental results for vortex shedding frequencies with correlations suggested by Elliot et al. [17] and Nakiboğlu et. al. [16]. We presented the comparison in terms of Equation 4.6 and Equation 4.5 for each pipe in Figure 4.15, Figure 4.16, Figure 4.17 and Figure 4.18. We observed in those charts in regard to our experimental results for vortex shedding frequency, the correlation by Nakiboğlu et. al. [16] predicts more accurately than by Elliot et al. [17].

$$F = \frac{nC_0}{2L\sqrt{1 + \frac{4HW_c}{D_iP_t}}} \qquad \text{n=1, 2, 3, …} \qquad (4.5)$$

$$F = \frac{nC_0(1 - Ma^2)}{2L\sqrt{1 + \frac{2HW_h}{D_i P_t}\left(1 + \frac{H}{D_i}\right)}} \qquad \text{n=1, 2, 3, ...} \qquad (4.6)$$

Figure 4.15. The vortex shedding frequency in terms of Reynolds number for the corrugated pipes 20.4 mm in diameter with comparison of Nakiboglu et. al. and Elliot 2005

Figure 4.16. The vortex shedding frequency in terms of Reynolds number for the corrugated pipes 25.4 mm in diameter with comparison of Nakiboglu et. al. [16] and Elliot et al. [17]
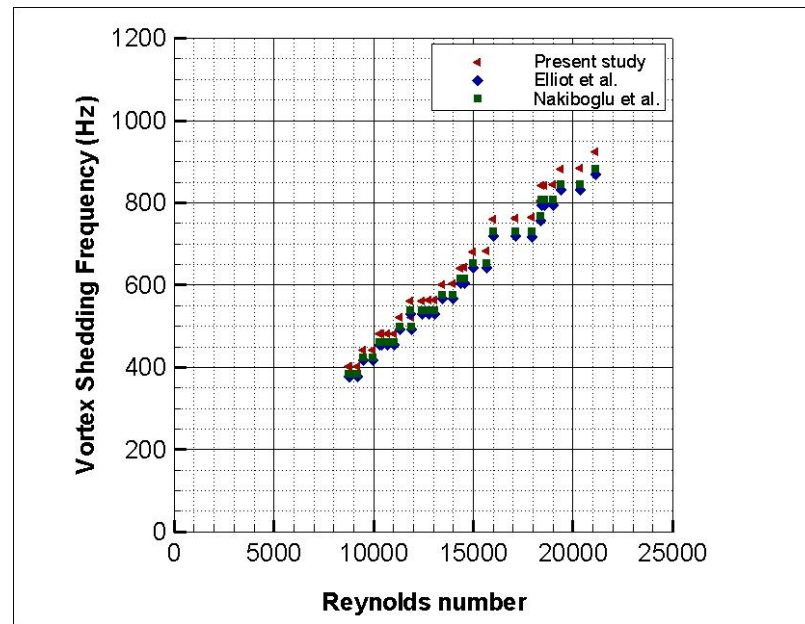
Figure 4.17. The vortex shedding frequency in terms of Reynolds number for the corrugated pipes 34.5 mm in diameter with comparison of Nakiboglu et. al. [16] and Elliot et al. [17]
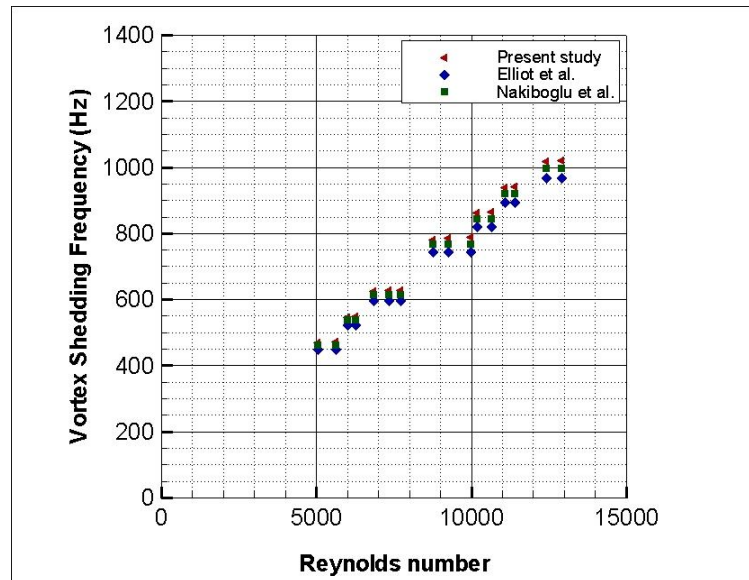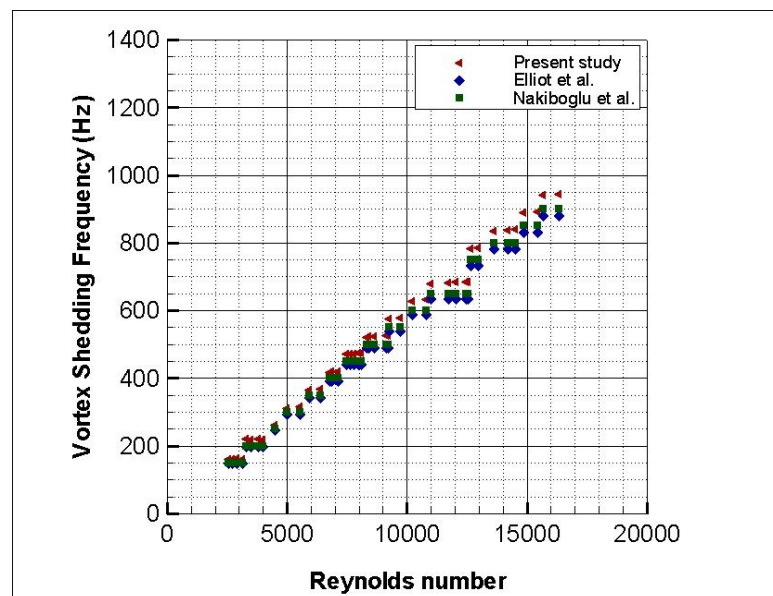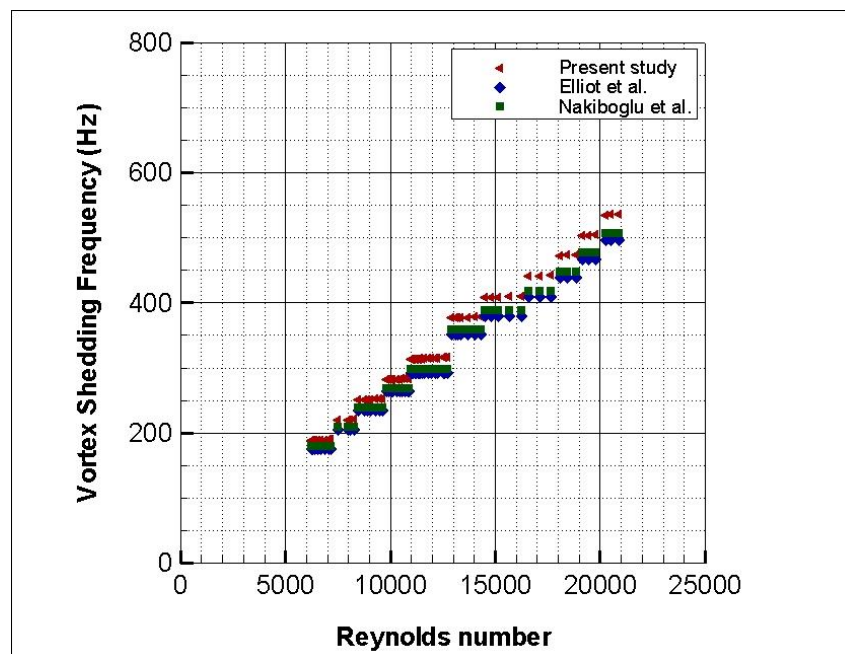

Figure 4.18. The vortex shedding frequency in terms of Reynolds number for the corrugated pipes 40.1 mm in diameter with comparison of Nakiboglu et. al. [16] and Elliot et al. [17]

4.3.1. Fundamental Frequencies and Effective Speed of Sound

According to Figure 4.19, we determine the fundamental frequency and the speed of sound for all pipes in Table 4.1. As it is known, fundamental frequency changes due to pipe length even the pipe diameter and the corrugation sizes remain the same. We found that the fundamental frequency comes down to solely the pipe length regardless the corrugation size and the pipe diameter. We witnessed in Figure 4.19 that the fundamental frequency drops with increasing pipe length. We correlated the frequency in Equation 4.7 that seems to be inverse proportional to the pipe length.

Table 4.1. Effective speed of sound for each pipe tested

Parameters	Pipe 1		Pipe 2		Pipe 3		Pipe 4	
D_i (mm)	20.4		25.4		34.5		40.1	
L (mm)	2007	1490	3007	1470	4001	1980	5097	1960
F_1 (Hz)	78.5	105.9	52.4	104.9	40.1	79.3	31.5	79.2
C_{eff} (m/s)	314.9	315.6	315.4	308.5	320.8	313.9	320.6	310.6

Figure 4.19. The fundamental frequency correlated due to pipe length

$$F_1 = 149.6 L_p{}^{-0.983} \tag{4.7}$$

The speed of sound for each pipe has been found more or less 300 m/s which is smaller than universal speed of sound of air (C_0 = 340 m/s). We assumed that the corrugations slow down the sound wave which was also reported by Elliot et al. [17]. We determined the speed of sound in the corrugated pipe from Equation 4.8 for all pipes.

$$F_n = \frac{n C_{eff}}{2L} \tag{4.8}$$

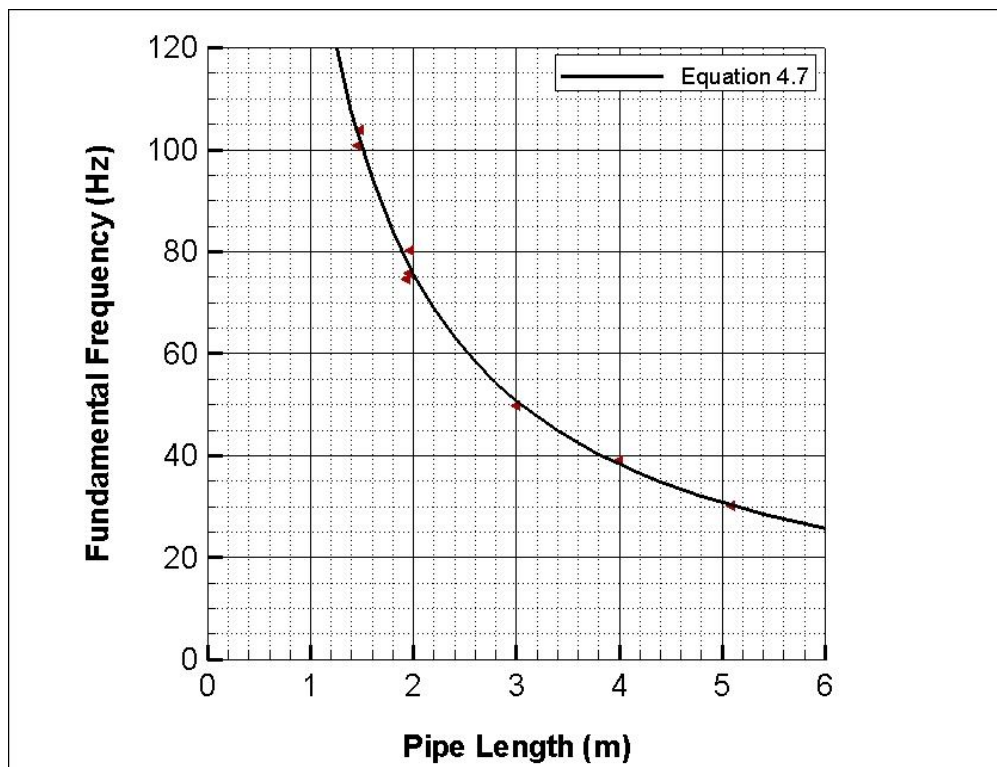Where n is the acoustic mode which equals to 1 for the first mode, C_{eff} (effective speed of sound) is the speed of sound in the corrugated pipe, L is the pipe length and f_n is the acoustic wave frequency at the nth mode. These are also how we found out modes of the vortex shedding frequency. As mentioned before, there is an interaction between aerodynamic and acoustic resonance. The energy is transferred from the hydrodynamic energy to the acoustic one thus as a consequence, the acoustic frequency influences the shear layer frequency and makes the shear layer surface adapt to itself. During this unsteady process, all harmonics of an acoustic natural frequency exists. Due to this presence of multiple acoustic frequencies, the vortex shedding frequency locks into one of the acoustic modes in terms of changing flow velocity. Therefore, we can determine at which mode vortex shedding is from Equation 4.8. Furthermore, we were able to use Equation 4.8 by multiplying it to both sides of Equation 4.7 to derive an expression for effective speed of sound as follows;

$$2 \times L_P \times F_1 = 149.6 \times (L_p)^{-(0.983)} \times 2 \times L_P \tag{4.9}$$

$$C_{eff} = 299.1 L_p{}^{-0.017} \tag{4.10}$$

Equation 4.10 predicts the experimental speed of sound within 2 %. This predicts the effective speed of sound worst for the pipe 34.5 mm with shorter length at 4 %. Equation 4.5 and Equation 4.6 spring from the effective speed of sound indicating that speed of sound in a corrugated pipe strictly depends on the corrugation sizes. However, we found the effective speed of sound is 300 ± 10 m/s. Equation 4.5 and Equation 4.6 estimate

effective speed of sound is around 300 m/s, no significant change in the effective speed of sound predicted in terms of corrugations sizes of corrugated pipe tested in the experiments. According to Equation 4.10, the effective speed of sound appears to be simply dependent of pipe length but a dramatic increase in the effective speed of sound only occurs if a very long pipe is implemented in the experiments.

4.3.2. Effect of Pipe Length

We investigated the effect of the pipe length on the Strouhal number and the vortex shedding frequency. We already know that the fundamental frequency increases as the pipe length increases. Therefore, we expect the vortex shedding frequency and Strouhal number would not change in terms of the pipe length with same diameter and corrugation size. What is only affected by the pipe length is the fundamental frequency. Nakiboglu et al [16] implied that Strouhal number is independent from the pipe length. We observed the effectiveness of the pipe length over Strouhal number and the vortex shedding frequency in Figure 4.20 and Figure 4.21 respectively.
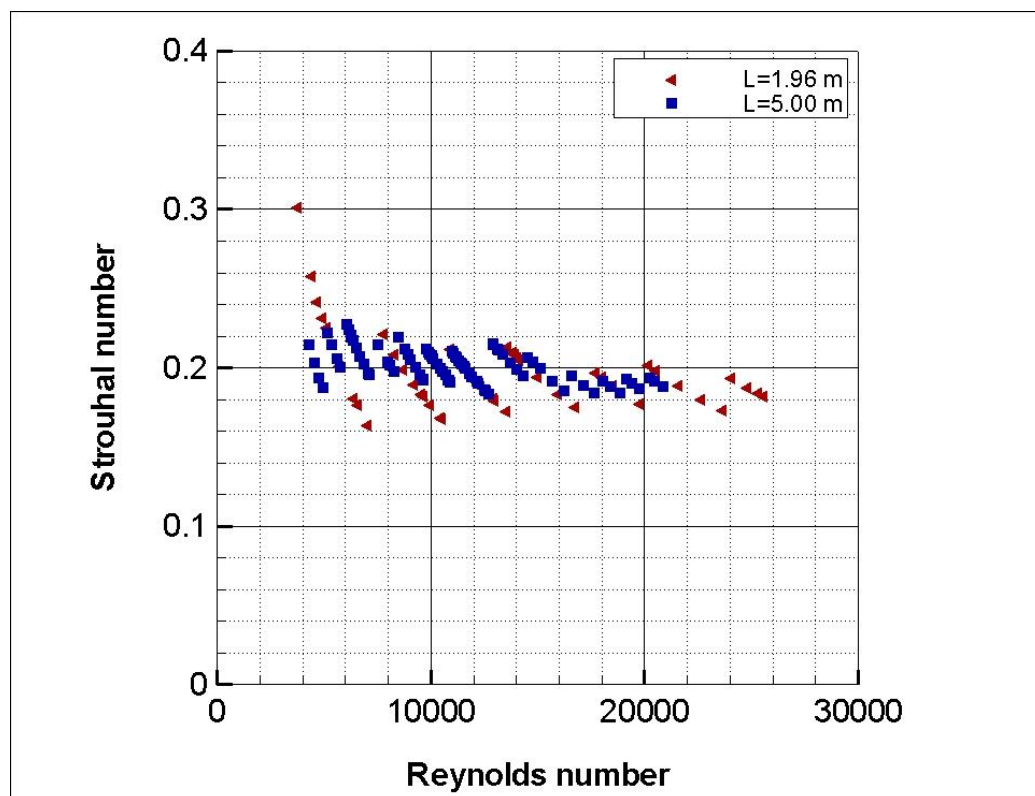
Figure 4.20. Strouhal number versus Reynolds number for the pipe D=40.1 mm
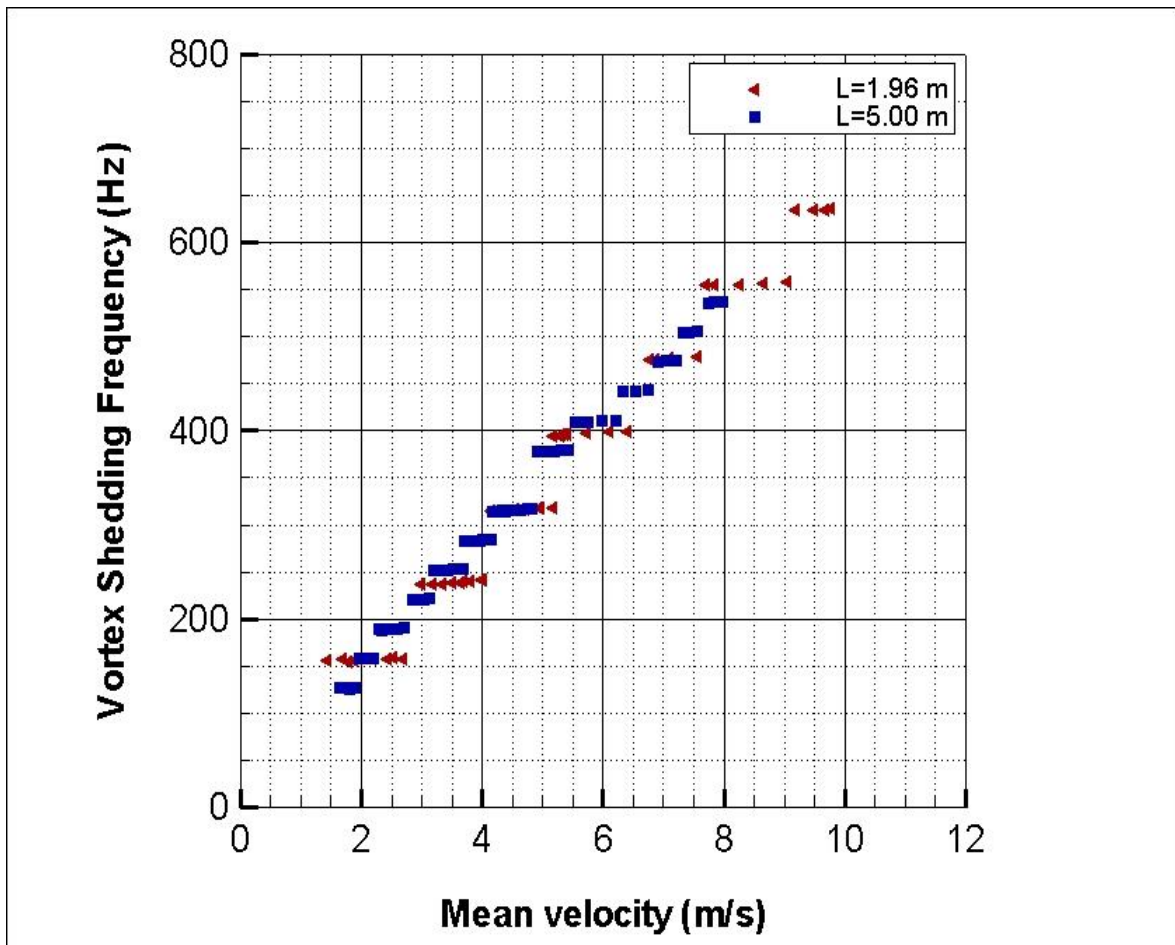
Figure 4.21. The vortex shedding frequency versus Mean velocity for the pipe D=40.1 mm

As per Figure 4.20, Strouhal number remains same for the two pipes with different lengths. However, the range of Strouhal number for each resonant mode seem to be larger for the shorter pipe because the vortex shedding frequency maintains longer for each mode whereas, it shifts to the next mode more quickly. As it appears in Figure 4.21, increase in the pipe length accelerates the shed frequency shift. Besides, the fundamental frequency is higher for the shorter pipe as expected. The onset velocity seems to be same for both pipes suggesting that the pipe length has no effect on the onset velocity whereas, Rudenko et al. [18] claimed the onset velocity is inversely proportional to the pipe length. Moreover, when we analyse the frequencies carefully, we noticed that there is a jump from the 10th mode to 12th mode for the longer pipe when mean velocity is at around 5 m/s (Re = 12600). We have 11th missing as seen in Figure 4.21. Rudenko et al. [18] mentioned this as some acoustic modes escaping from the detection due to narrow whistling ranges with low amplitudes. They explained this situation there would be one mode dominating

neighbouring modes. One can also notice missing modes for other pipes in Figure 4.14 which are the 9th mode (v=6.0 m/s, Re=7700), 14th mode (v=7.4 m/s, Re=12600) and 18th mode (v=7.0 m/s, Re=15800) for the corrugated pipes with diameter of 20.4 mm, 25.4 mm and 34.5 mm respectively. As we mentioned before, we have common pipe with same diameter (25.4 mm) and corrugations as Popescu et al. [14] does. Their pipe is much smaller than ours so their fundamental frequency is higher. They reported the onset velocity as 3.8 m/s (Re=6600) at 2nd mode where we found it as 1.5 m/s (Re=2500) at the 3rd mode. Therefore, it would be expected that the onset velocity they found is less than 3.8 m/s. However, when we take into account their result is in the 2nd mode, the onset velocity would be less at the 1st if it whistled there.

4.4. SOUND PRESSURE LEVEL IN CORRUGATED PIPES

In regard to the experimental analysis on pressure fluctuations, as Reynolds number gets higher of specific one, a leap in Strouhal number is witnessed and the acoustic mode shifts to the next. Hence, in the same acoustic mode at which the vortex shedding frequency is almost constant, Strouhal number begins to fall slightly until the resonant mode changes. In the meantime, fluctuation amplitude rises till it reaches its peak which corresponds to the peak whistling frequency and Strouhal number and then begins to drop. The amplitude behaves the same within every each acoustic mode. Due to the interaction between hydrodynamic and acoustic field, the energy is supplied from the former to later and as a consequence, the acoustic frequency sways the shear layer frequency and makes the shear layer surface adapt to itself which allows the vortex at the cavity mouth bursts to core flow. During the fluid flowing through the corrugated pipe steadily, all harmonics of an acoustic natural frequency exists. Due to presence of multiple acoustic frequencies, the vortex shedding frequency locks into one of them in regard to flow velocity. The acoustic pressure pulsation amplitude hits the maximum at the velocity at which the vortex shedding frequency conforms to an acoustic mode. We illustrated this lock in phase in Figure 4.22.
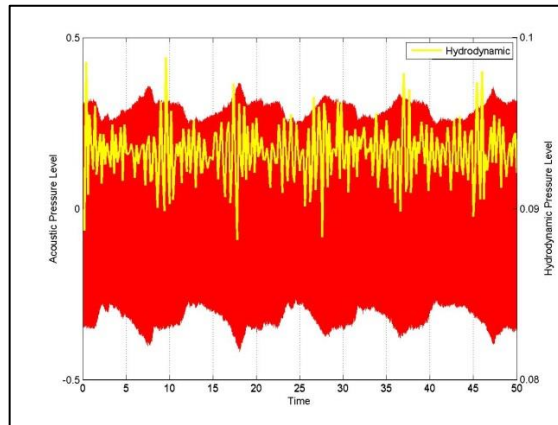
Figure 4.22. Hydrodynamic pressure signals coupled with the acoustic signals for D=40.1 mm, Re=20500

As it can be witnessed apparently, the acoustic waves cooperates with the acoustic waves which are measured oscillations caused by vortexes bursting to the core flow. We interpret this as the vortex shedding frequency conform to the acoustic flow field (red zone in Figure 4.22), the whistling brings about.

Popescu et al. [14] explained this mechanism that the shear layer instability caused by vortex sheddings drive the acoustic pressure perturbation in the pipe. When the shear layer frequency complies with natural frequency of the pipe, whistling is audible. The sound pressure is affected by the length of the pipe, if the pipe length increases, the pressure level increases as it is demonstrated in Figure 4.23.
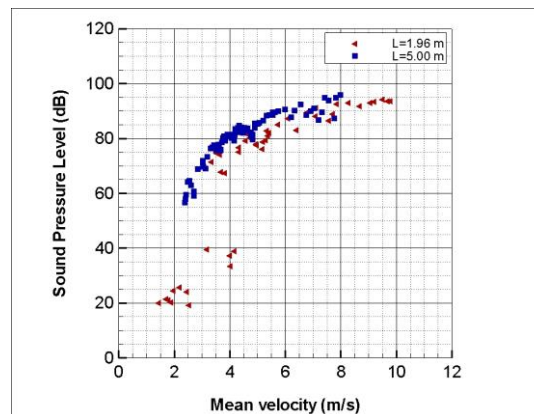
Figure 4.23. Sound pressure level versus Mean velocity for D=40.1 mm

We agreed Debut et al. [19] that the pressure amplitude and the lock-in frequency range elevate if the pipe length increases for an identical corrugation sizes and diameter. According to Figure 4.23 and Figure 4.21, the lock-in frequency range and sound pressure level get larger with increasing pipe length as they suggested.

We can clearly see in Figure 4.23 that the sound pressure level gets higher with higher flow velocity for all pipes and the corrugations influence the sound power. Popescu et al. [14] and Debut et al. [19] noticed the pressure amplitude drops before the lock-in frequency shifts where they also captured more than one with high amplitude peaks. We demonstrate these frequencies captured in the same flow velocity as below in Figure 4.24
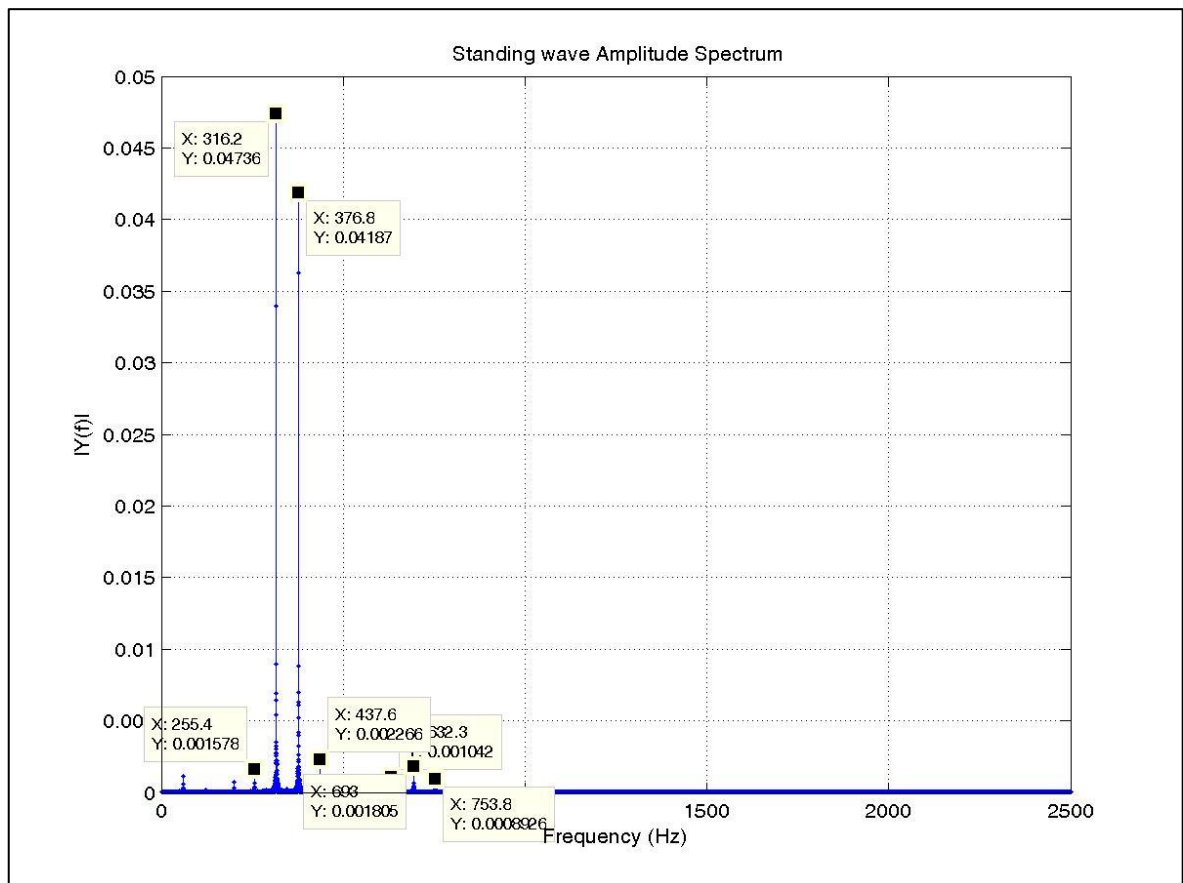
Figure 4.24. The Fluctuation amplitude spectrum at Re=12800 for D=40.1 mm L=5 m

As mentioned before, all harmonics of a natural exist during the flow. When the vortex shedding frequency locks into one of them, the whistling occurs and the resulting frequency such as in Figure 4.24 becomes the frequency of vortex bursting the core flow.

In the case of Figure 4.24, the vortex shedding frequency is shifting to the next mode or harmonic. It is about to lock into 12th mode from 10th mode. We reported before one mode is skipped during shifting modes which is 11th here. In the meantime, the Strouhal number and fluctuation amplitude are decreasing in this resonant mode. Nakiboglu et al. [16] suggested the same. They reported that the amplitude of pressure oscillations rise until it approaches the peak with increasing flow velocity within an acoustic mode. Further increase in the flow velocity decreases this fluctuation amplitude. We also demonstrated this trend in Figure 4.25.
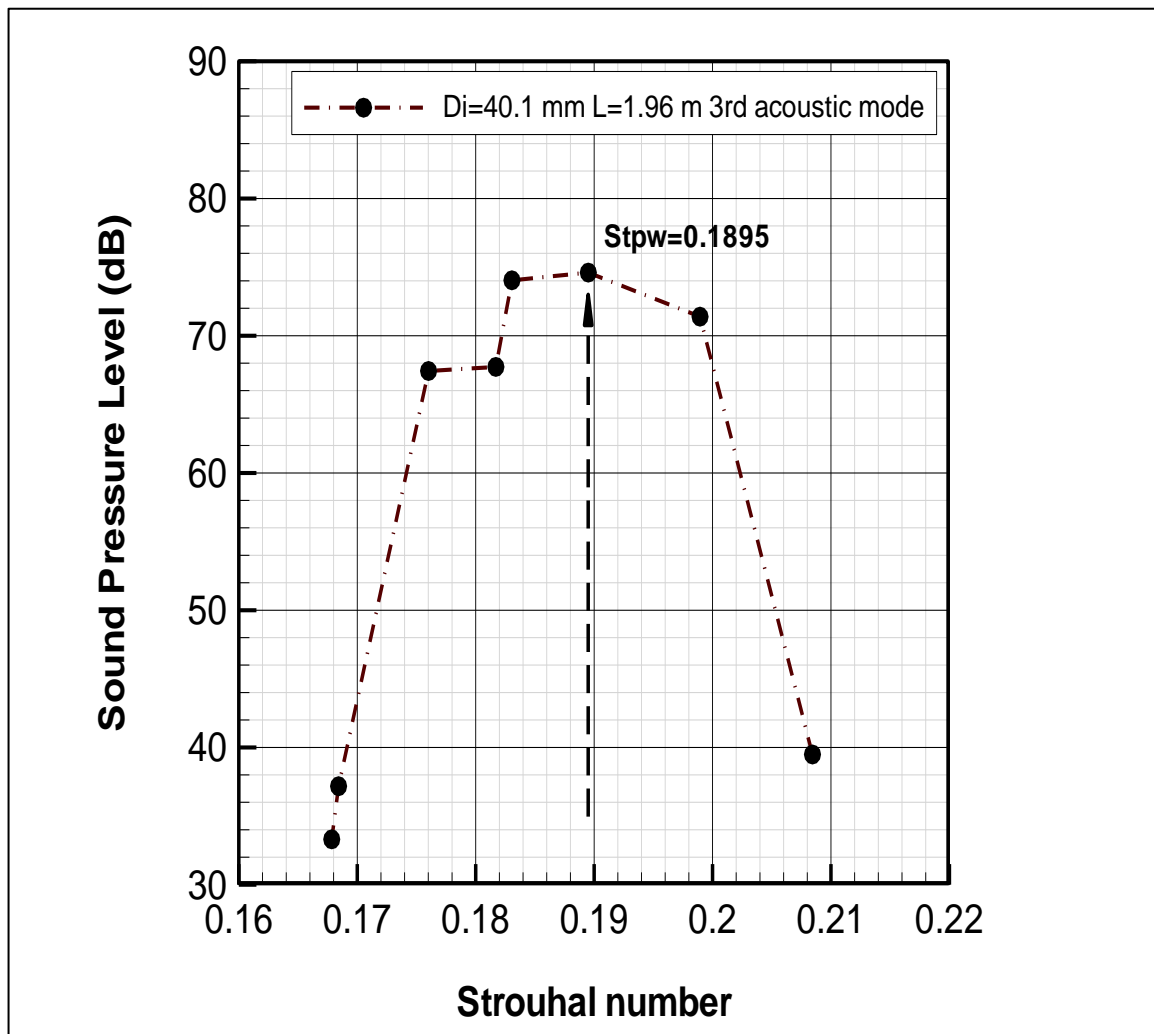
Figure 4.25. Sound pressure level versus Strouhal number for the third acoustic mode of the corrugated pipe, 40.1 mm in diameter and 1.96 m in length. The peak-whistling Strouhal number (St_{pw}) is determined as the value at which the amplitude of pressure fluctuation is the maximum for a resonant mode.

We illustrated in Figure 4.26, the peak whistling Strouhal number over sound pressure level in terms of the vortex shedding frequency for the pipe 40.1 mm in diameter and 1.96 m in length. Nakiboglu et al. [16] suggested, the peak whistling Strouhal number is almost stable in spite of increase in either sound pressure or vortex shedding frequency. Figure 4.26 illustrates these oscillation pressure values in the each resonant mode over corresponding vortex shedding frequency does not also influence the peak whistling Strouhal number. Moreover, Figure 4.26 and Figure 4.11 emphasize this stability of the peak whistling Strouhal number over sound pressure level for all corrugated pipes tested.
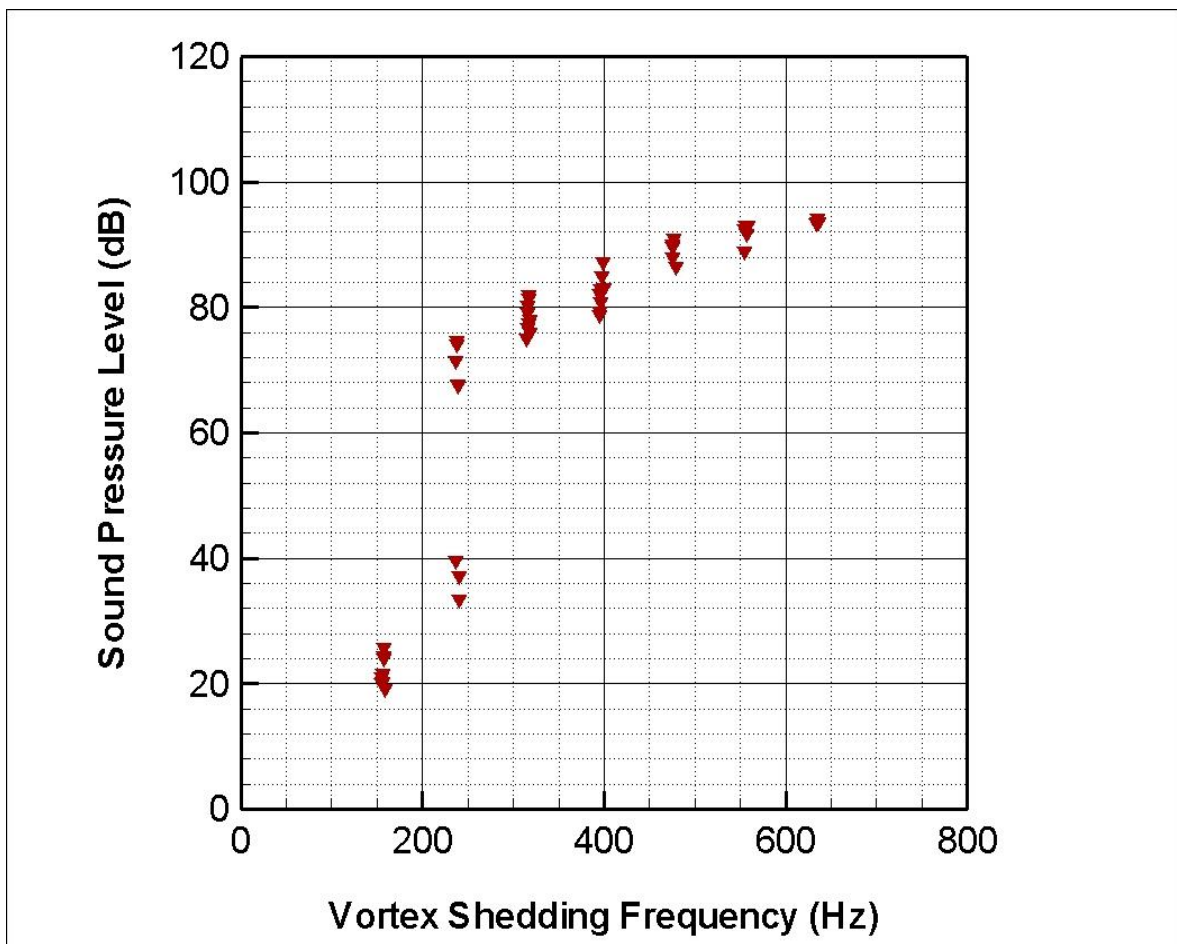
Figure 4.26. Sound pressure level versus lock-in frequencies for the pipe 40.1 mm in diameter and 1.96 m in length

Finally the friction factor is examined as a function of the peak-whistling Strouhal number in Figure 4.27. The friction factor appears to increase with the increasing peak-whistling Strouhal number. As discussed in Figure 4.3, Figure 4.27 also shows that the higher ratio

of the crest width to pipe diameter results in the higher friction factor. Therefore, combining the results of Figure 4.3, Figure 4.13 (or Figure 4.12) and Figure 4.27, we draw a conclusion that the higher ratio of the crest width to pipe diameter, the higher peak-whistling Strouhal number, the higher friction factor.
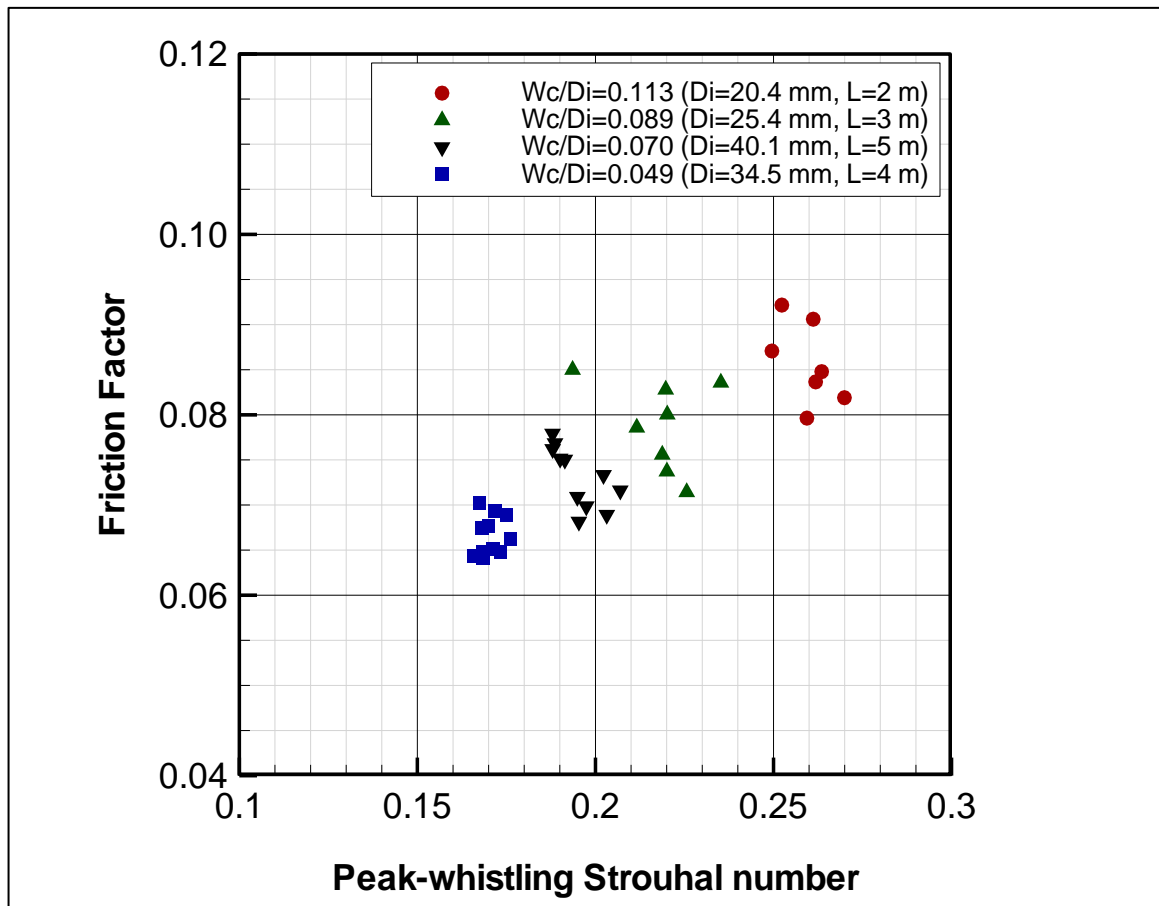
Figure 4.27. The friction factor as a function of the peak whistling Strouhal number.

4.5. INVESTIGATION OF HEAT TRANSFER OVER CORRUGATED PIPES

4.5.1. Corrugated Pipe with The Diameter of 20.4 mm and 3 m Long

As mentioned in Section 3.5, we placed thermocouples on the pipe which is 20.4 mm in diameter for crest and hollow surface and insulated the pipe twice. However, before we tested the forced convection for the corrugated pipe, we have to ensure whether thermocouples are inconsistent or not and we tried to observe heat dissipation with respect to pipe wall temperature. Thus, we let no air through pipe during the experiment and we

also insulated two open sides of pipe. Figure 4.28 illustrates results of temperature for those thermocouples as regards position of thermocouples on the pipe over range of heat loss.
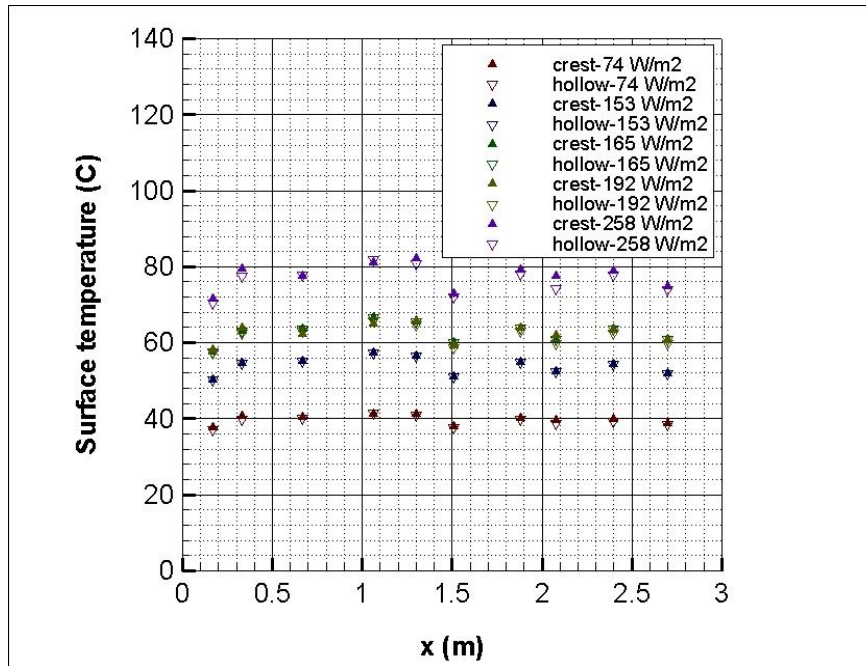
Figure 4.28. Local hollow and crest surface temperature for heat loss values for corrugated pipe 20.4 mm in diameter

We noticed in Figure 4.28 that inconsistency of thermocouples escalates as we heated the pipe. This would be caused by the glue holding the thermocouples on surface of the pipe. As the pipe is heated, temperature of surface increases and glue may indicate some thermal resistance. For instance, thermocouples placed on the position of 0.17, 1.51 and 2.7 may have some glue escaped underneath of thermocouples where they are in contact with the surface of the pipe. Therefore, those thermocouples may rather display lower temperature than others. Having said that though, we knew that those thermocouples would indicate lower temperature in the forced convection test so the resulting heat transfer coefficient thus, Nusselt number would be higher than usual for those local surfaces.

We proceeded to estimate the heat loss respect to pipe wall temperature subtracted from infinite temperature. In Figure 4.29, we fitted data for the heat loss in regard to wall temperature relative to environment temperature (infinite temperature).
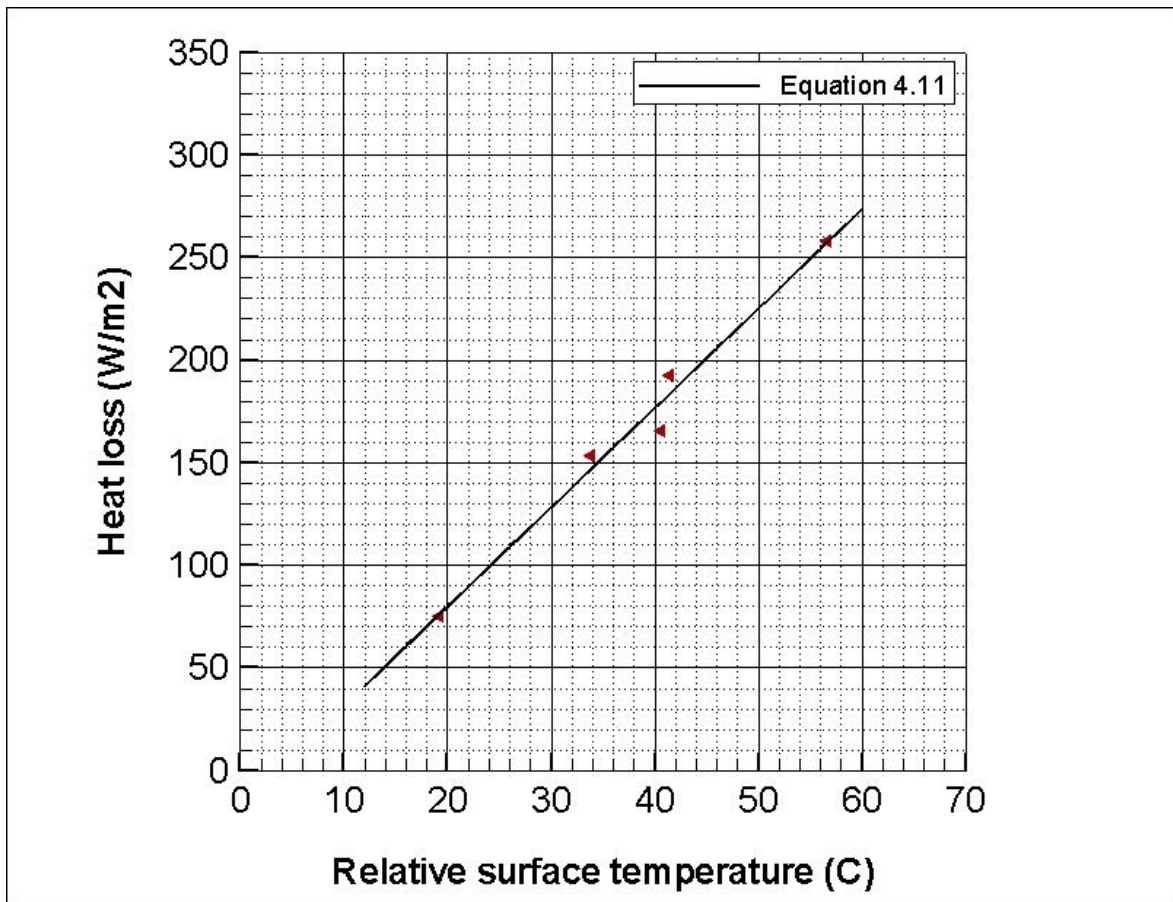
Figure 4.29. Heat loss fitted with respect to surface temperature relative to infinite

temperature for corrugated pipe 20.4 mm in diameter

The linear fitted data above express that higher temperature, more heat loss.

$$\delta_{loss}(T_s) = \frac{P_{loss}(T_s)}{A_{p,cs}} = 4.8\Delta T_S - 16.6 \tag{4.11}$$

where $\Delta T_S = T_s - T_\infty$

We implemented Equation 4.11 to determine net heat flux through the corrugated pipe for the test results of forced convection. As mentioned in Section 3.5, we derived equation in order to determine net heat flux and local mean temperature through the corrugated pipe. We derived Equation 3.10 for local supplied heat due to variation of electrical resistance. First of all we plotted the local wall surface temperature as it follows;
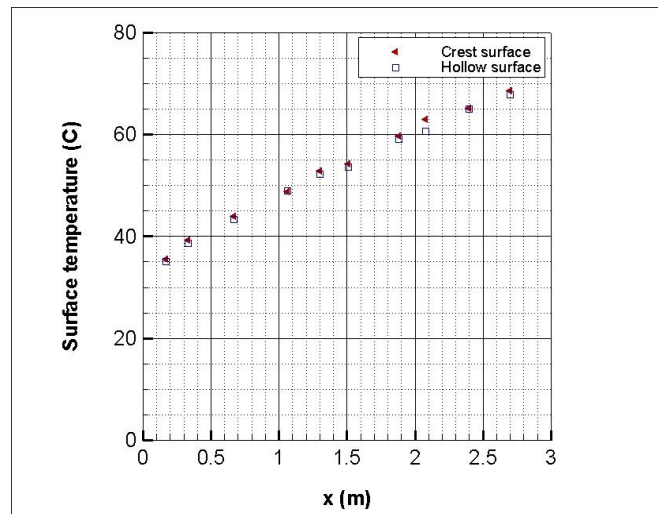
Figure 4.30. Local hollow and crest surface temperature for forced convection heat transfer test for corrugated pipe 20.4 mm in diameter

As per Figure 4.30, we witness temperature at crest and hollow surface are locally identical at Re=6500. Local surface temperature is different for each position of x and increases as air flows through the pipe. Hence, we estimated the local heat loss by the help of Equation 3.11 and we manipulated Equation 4.11 to become the function of position (x) as displayed in Table 4.2;

Table 4.2. Local temperature and heat loss for crest and hollow surfaces for corrugated pipe 20.4 mm in diameter

x (m)	$T_{s,crest}$	$T_{s,hollow}$	$\delta_{loss,crest}$	$\delta_{loss,hollow}$
0.17	35.47	35.14	53.3	51.6
0.33	39.31	38.72	71.8	68.9
0.67	43.94	43.39	94.2	91.5
1.06	48.85	49.03	117.9	118.8
1.30	52.89	52.23	137.5	134.3
1.51	54.28	53.71	144.2	141.5
1.88	59.66	59.06	170.3	167.4
2.08	63.00	60.62	186.4	174.9
2.40	65.25	64.96	197.3	195.9
2.70	68.67	67.85	213.9	209.9

Regarding Table 4.2, the heat loss can be written as a function of x. Due to identical temperature results for hollow and crest surface, the local heat loss is almost same (maximum difference 4 Watt/m^2 corresponds to 2 % except x=2.08) for both locally identical surfaces so we took average of heat loss for each position Accordingly, we predicted the net heat flux through pipe by taking Equation 4.12 into account;

$$\delta_{net}(x) = \delta_{supply}(x) - \delta_{loss}(x) \qquad (4.12)$$

Net heat flux is plotted in Figure 4.31 and we witnessed the heat flux is not constant so we are not able to assume mean temperature increases linearly between the temperature values of inlet and outlet section. Thus, we have to come up with an expression for mean temperature.
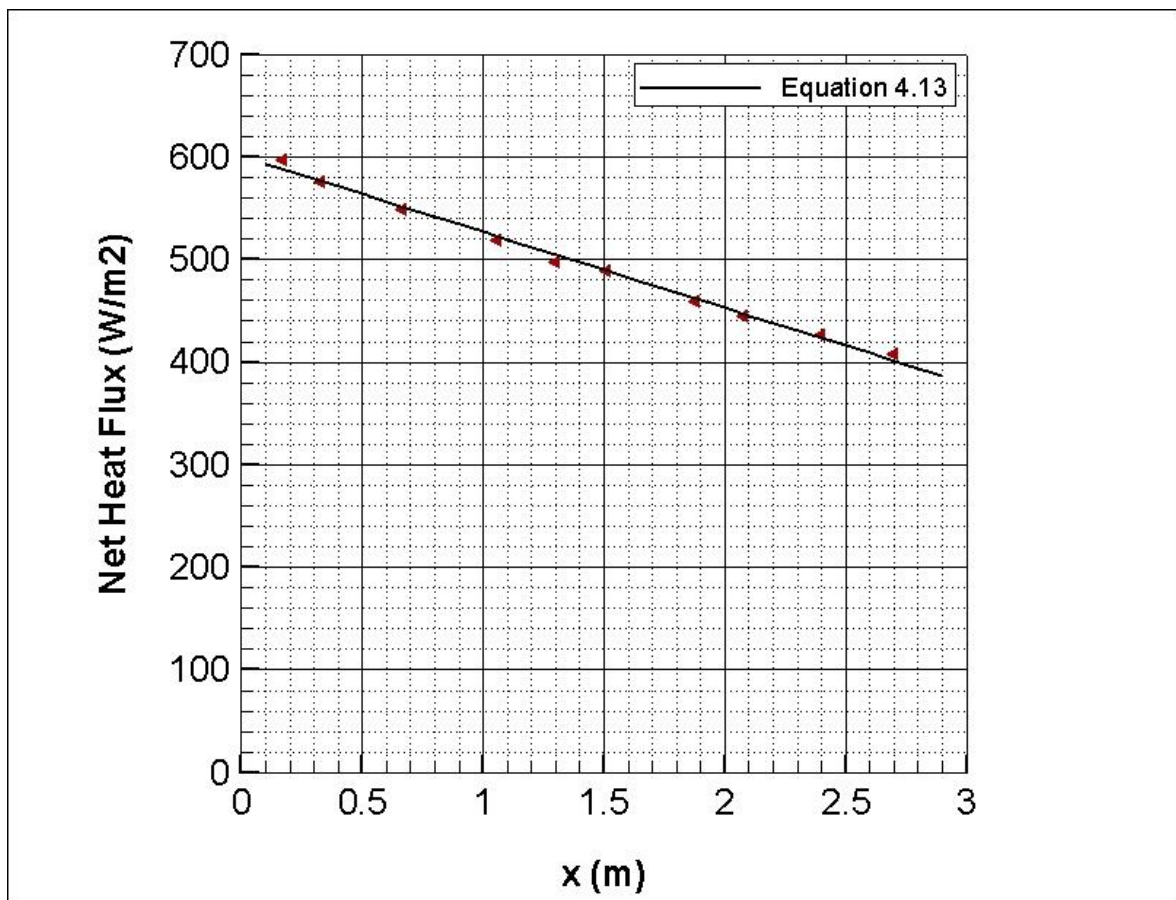

Figure 4.31. Local Heat flux at Re=6400 for corrugated pipe 20.4 mm in diameter

According to Figure 4.31, the net heat flux is a function of x and decreases linearly as x increases. Linear fitting is used to derive the equation below;

$$\delta_{net}(x) = -73.8x - 600.7 \qquad (4.13)$$

We benefit conservation of energy to estimate the local mean temperature through the corrugated pipe and displayed the resulting local mean temperature values with local surface temperature values in Table 4.3.

$$\delta_{net}(x)\pi D_i dx = mC_p dT \qquad (4.14)$$

$$dT = \frac{\pi D_i}{mC_p}\delta_{net}(x)dx \qquad (4.15)$$

$$\int_{T_0}^{T} dT = \frac{\pi D_i}{mC_p}\int_{0}^{2.99}\delta_{net}(x)dx \qquad (4.16)$$

$$T_m(x) = T_0 + \frac{\pi D_i}{mC_p}(-36.9x^2 + 600.7x) \qquad (4.17)$$

Table 4.3. Local hollow and crest surface and mean temperature for corrugated pipe 20.4 mm in diameter

	Surface Temperature			Mean Temperature
	x	crest	hollow	
inlet	0	21.01		21.01
Pipe Surface	0.17	35.47	24.14	24.14
	0.33	39.31	27.03	27.03
	0.67	43.94	32.96	32.96
	1.06	48.85	39.45	39.45
	1.30	52.89	43.26	43.26
	1.51	54.28	46.50	46.50
	1.88	59.66	51.95	51.95
	2.08	63.00	54.76	54.76
	2.40	65.25	59.08	59.08
	2.70	68.67	62.91	62.91
outlet	3.12	66.65		67.98

As regards Table 4.3, we estimate the outlet temperature with derived equation (Equation 4.17) 2 % deviating from the measured one. We justify the accuracy of Equation 4.17 in this way.

We plotted the local surface temperature and local mean temperature together to observe whether the temperature difference between each local surface temperature and mean temperature is constant in the fully developed region in the figure below.
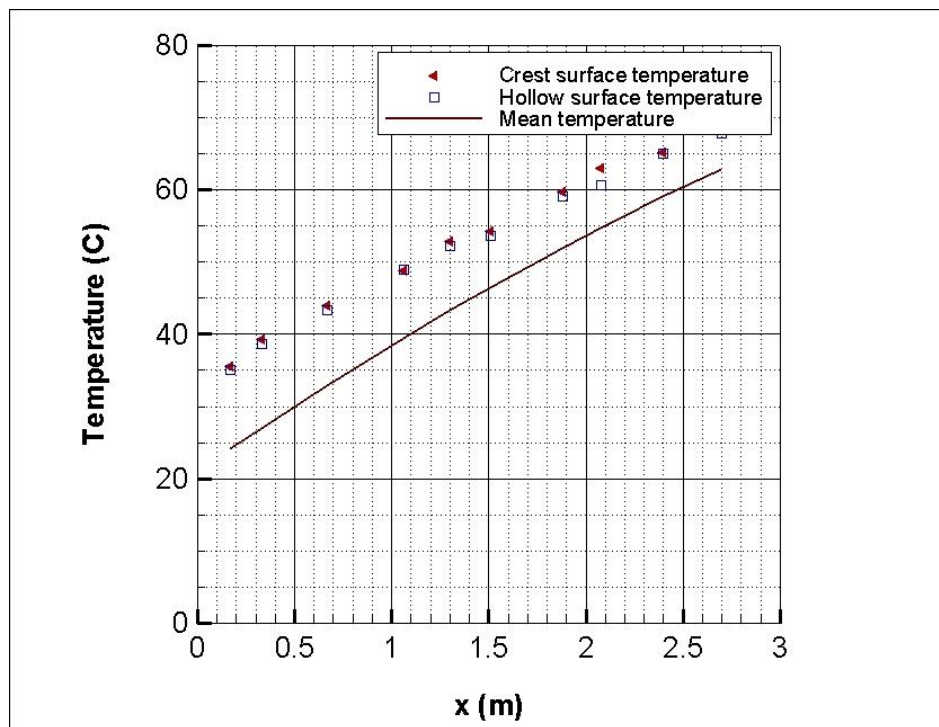
Figure 4.32. Local crest and hollow surface and mean temperature values at Re=6400 for corrugated pipe 20.4 mm in diameter

As can be seen in Figure 4.32, the flow becomes fully developed in 1 m for the test result of Re=6400. However, the temperature difference deteriorates as we come near the outlet of the pipe. Due to the fact that, the heat loss is not constant for forced convection test because of relative temperature decreasing along the pipe. However, we did take the heat loss into consideration in Equation 4.17 but we noticed in Figure 4.32, thermocouples at x=2.4 and x=2.7 read temperature lower than most, relatively. Therefore, we regarded that inevitable because thermocouples are also placed inconsistently due to some issues caused by glue. Anyway, we calculated local heat transfer coefficient and local Nusselt number.

$$h_{crest}(x) = \frac{\delta_{supply} - \delta_{loss,crest}}{(T_{s,crest} - T_m)} \tag{4.18}$$

$$h_{hollow}(x) = \frac{\delta_{supply} - \delta_{loss,hollow}}{(T_{s,hollow} - T_m)} \tag{4.19}$$

$$Nu_{crest}(x) = \frac{h_{crest}(x)D_i}{k} \tag{4.20}$$

$$Nu_{hollow}(x) = \frac{h_{hollow}(x)D_i}{k} \tag{4.21}$$

According to Equation 4.18 and Equation 4.19 and Figure 4.32, we expect local heat transfer coefficient for the last two local points (x=2.4 and x=2.7) will be higher than other values. We plotted the local heat transfer coefficient and observed the our prediction is true in Figure 4.33;
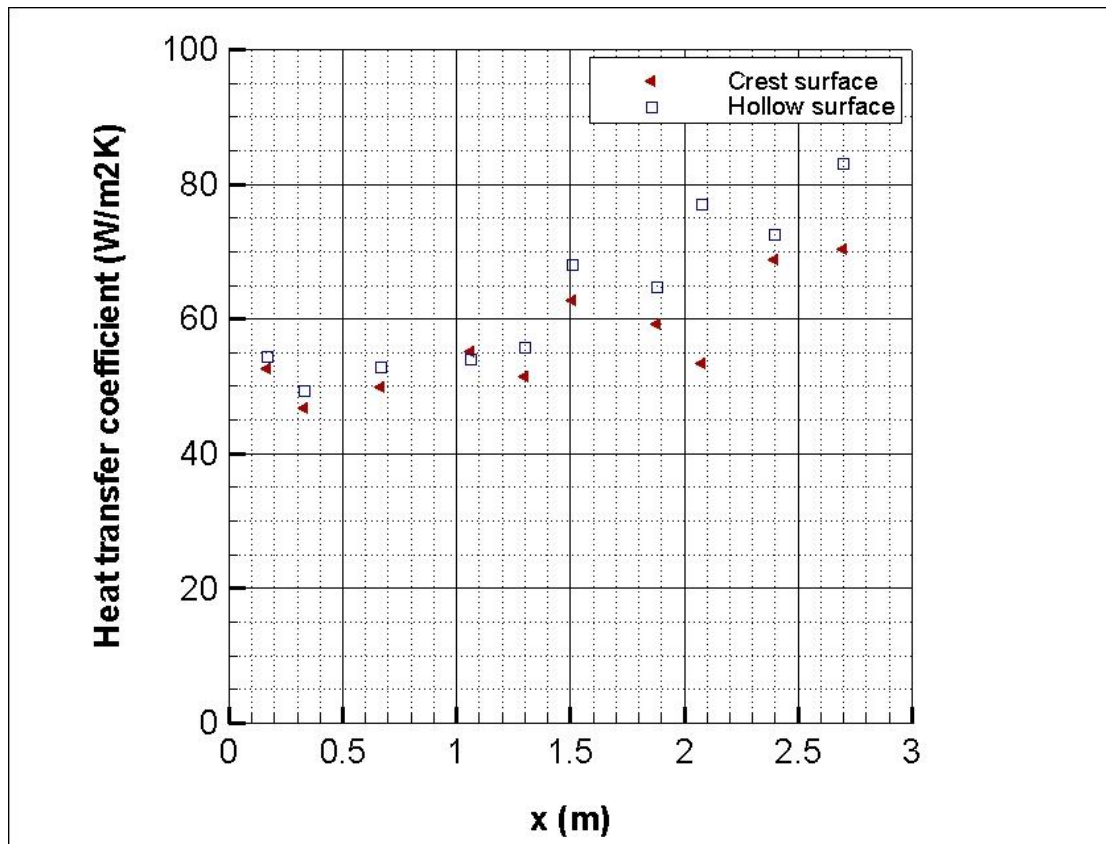

Figure 4.33. Local heat transfer coefficient at Re=6400 for crest and hollow surface for corrugated pipe 20.4 mm in diameter

According to Equation 4.20 and Equation 4.21, local Nusselt number trend corresponds to one in Figure 4.34;
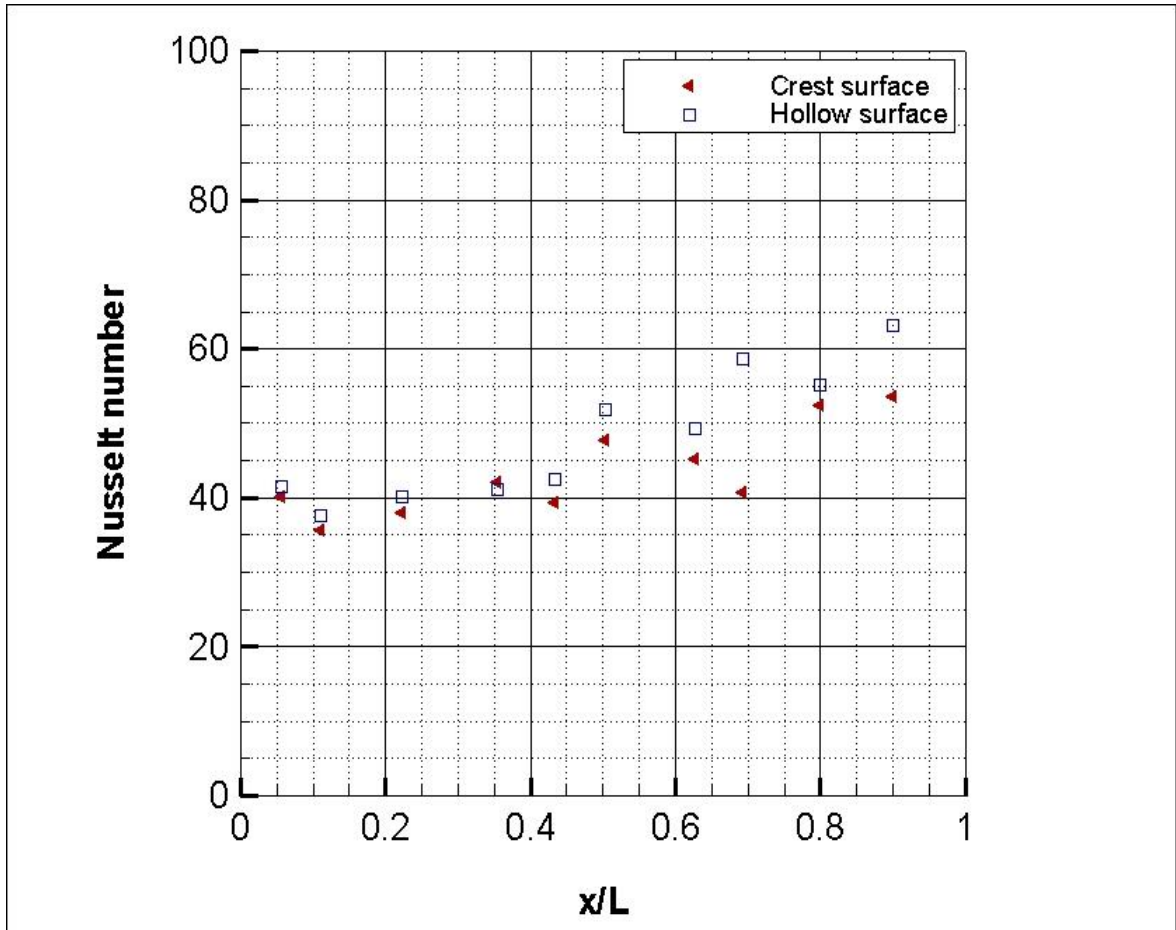
Figure 4.34. Local Nusselt number at Re=6400 for crest and hollow surface for corrugated pipe 20.4 mm in diameter

As per Figure 4.34., Nusselt number should be around about 40. As expected, local Nusselt number is high near inlet section and decreases along the corrugated pipe with diameter of 20.4 mm at Re=6400. The local Nusselt number converges to approximately 40 which is average Nusselt number when the local length is around 1 m. This indicates the fully developed region is reached around 1 m from inlet section of the corrugated pipe. As we mentioned before we also expected the local heat transfer coefficients thus, Nusselt numbers at x=1.51, x=1.88, x=2.4 (for only crest surface) and x=2.7 would increase due to heat loss and the procedure for the placement of thermocouples. Having said though, we can say average Nussselt number is roughly 40 at Re=6400.

We followed the same procedure for the determination of average Nusselt number for various Reynolds number defined Equation 4.11 to Equation 4.21. We displayed average Nusselt number with respect to Reynolds number in Figure 4.35.
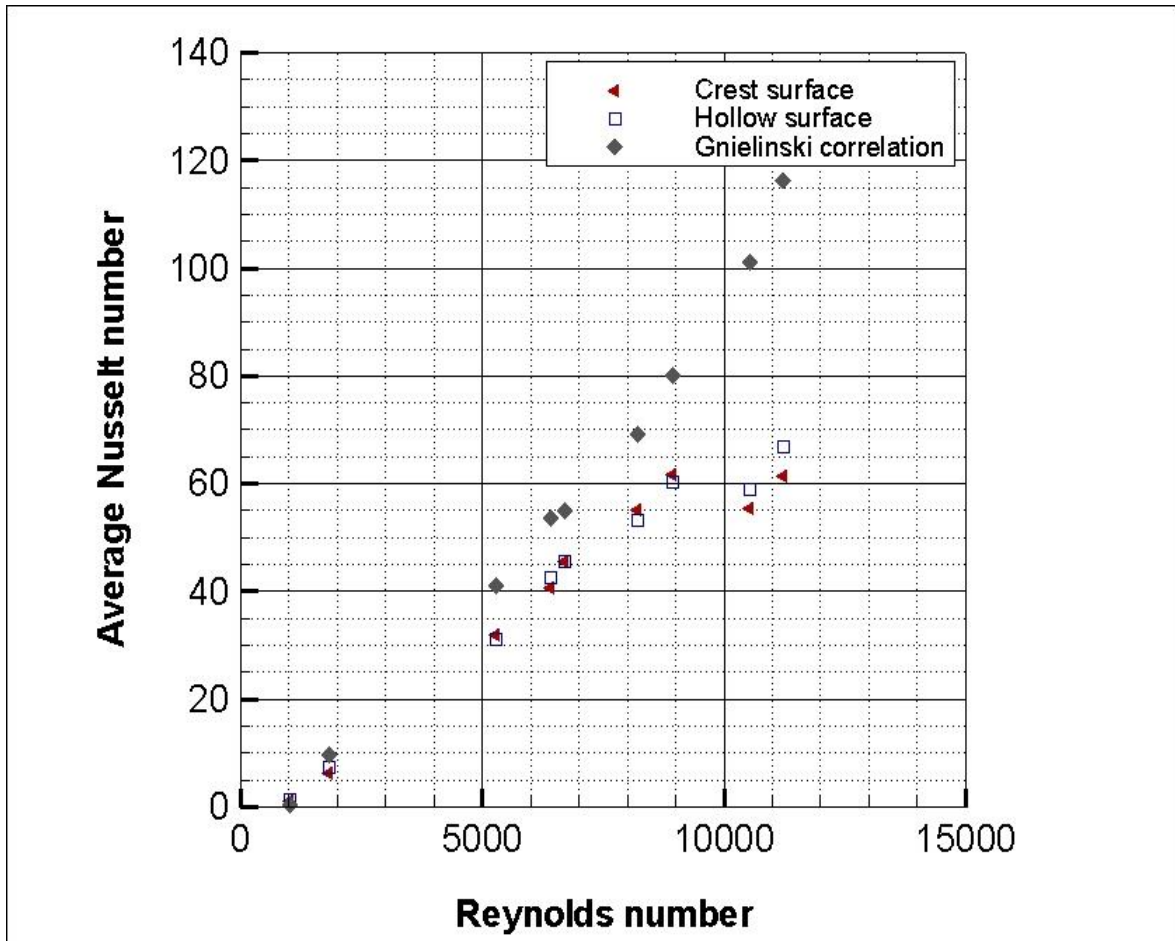
Figure 4.35. Nusselt number for crest and hollow surface with respect to Reynolds number for corrugated pipe 20.4 mm in diameter

According to Gnileski's correlation, Nusselt number continues to increase whereas our test results of Nusselt number seem to rise until Reynolds number is around 11200 at the Nusselt number around 60. Another observation in Figure 4.35 is Nusselt number for crest and hollow surface are almost the same for a wide range of Reynolds number 2000 – 12000 for the corrugated pipe tested. Back to our experiments on friction, we recall that range is turbulent region. In this region flow in the pipe is chaotic and pulsating. Mechanism of flow in cavities is the circulating fluid in those cavities bursts to the core flow and join the core flow at when the new fluid drags into cavities. Therefore the fluid is

always mixing which explains the temperatures for both surfaces such as hollows and crests are very close to each other. That is why we obtain almost identical Nusselt number. So, we placed thermocouples only on crest surface for the next pipe tested which has 34.5 mm in diameter and 1.96 m long.

4.5.2. Corrugated Pipe with The Diameter of 34.5 mm and 1.96 m Long

In Section 3.5, we discussed about placement of thermocouples on the surface of the corrugated pipe. In Figure 4.36, we present the heat loss with respect to pipe surface temperature relative to infinite temperature as we did before for the pipe at the previous section. The readings of temperature were recorded while no air is let through the corrugated pipe.
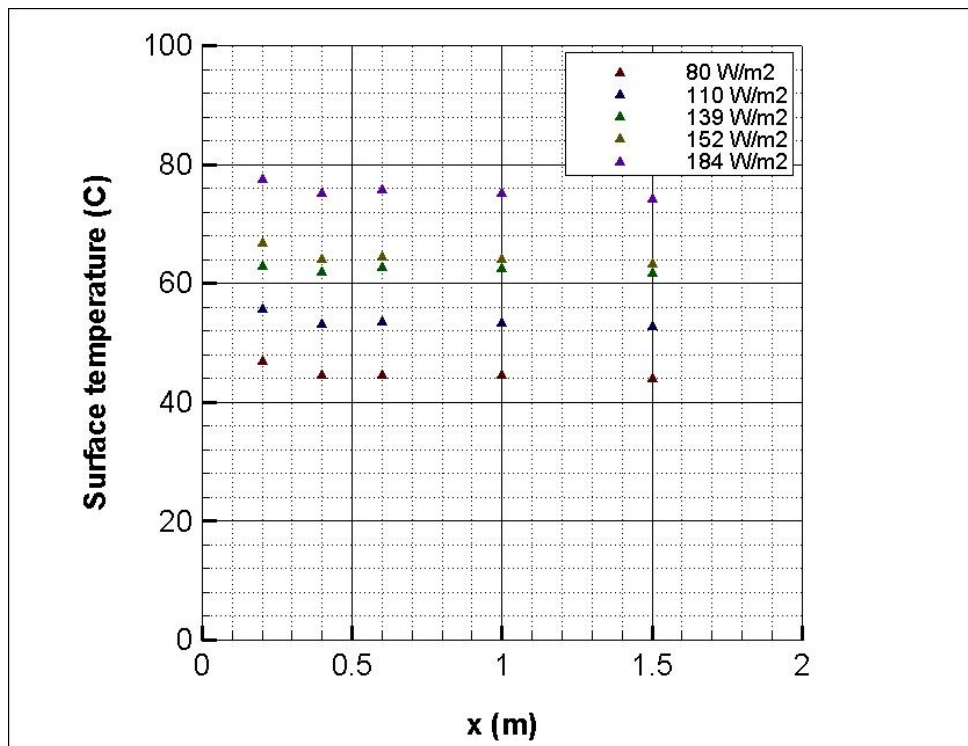

Figure 4.36. Local surface temperature for heat loss values for corrugated pipe 34.5 mm in diameter

As appear in the figure above, temperature readings at defined positions are consistent enough. This indicates that the method (the one without glue) used to place thermocouples for the corrugated pipe with 34.5 mm in diameter is better than the one at the previous

section. Therefore, we expected to have more consistent trend for heat transfer coefficient therefore, Nusselt number.

We carried on predicting the heat loss with respect to pipe wall temperature relative to infinite temperature. In Figure 4.37, we fitted variables for the heat loss in terms of surface temperature relative to outer temperature (infinite temperature).
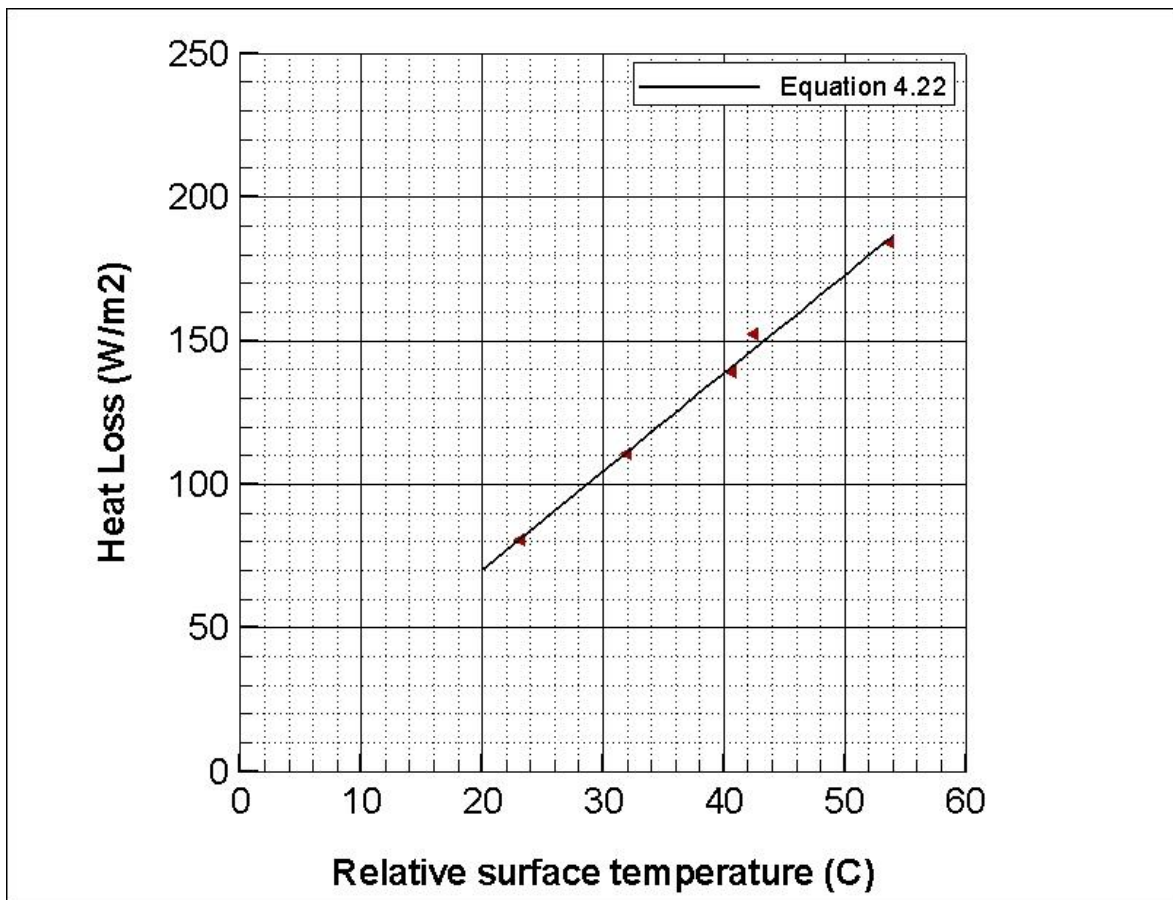

Figure 4.37. Heat loss fitted with respect to surface temperature relative to infinite temperature for corrugated pipe 34.5 mm in diameter

The linear fitted data above express that higher temperature, more heat loss.

$$\delta_{loss}(T_s) = \frac{P_{loss}(T_s)}{A_{p,cs}} = 3.4\Delta T_S - 1.6 \tag{4.22}$$

where $\Delta T_S = T_s - T_\infty$

We applied Equation 4.22 to calculate net heat flux to the corrugated pipe for forced convection test. As it was done in Section 3.5, Equation 3.11 (derived for local heat supplied by transformer due to change of electrical resistance) is utilized in order to determine net heat flux and local mean temperature through the corrugated pipe. We derived Equation 3.10 for local supplied heat due to variation of electrical resistance. In Figure 4.38, we displayed the change local wall surface temperature for forced convection test at Re=4700;
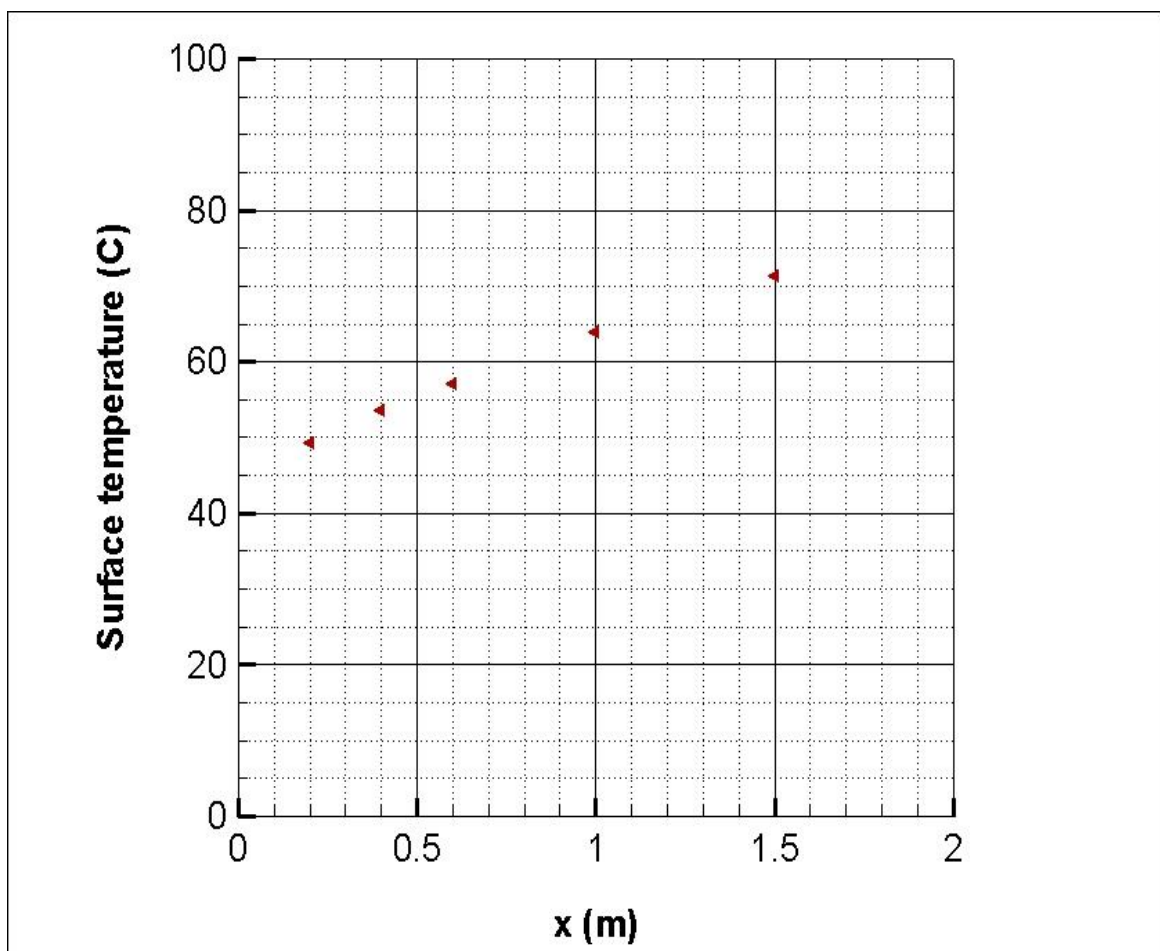

Figure 4.38. Local surface temperature at Re=4700 for forced convection heat transfer test for corrugated pipe 34.5 mm in diameter

Local wall temperature of the corrugated pipe differs for each position on the surface of the pipe and escalates as air is flowing steadily through the pipe. Thus, we predicted the local

heat loss with Equation 4.22 and we benefited Equation 4.22 to transform to the function of x as we did for the corrugated pipe with 20.4 mm in diameter in the previous section.

Table 4.4. Local surface temperature and heat loss for corrugated pipe 34.5 mm in diameter

x	T_s	δ_{loss}
0.2	93.39	49.2
0.4	108.45	53.6
0.6	120.11	57.0
1.0	143.81	63.9
1.5	169.21	71.4

According to Table 4.4, the heat loss can be defined as a function of x. We already mentioned at previous section thermocouples are only placed on crest surfaces so we have only heat loss thus, net heat flux measurements on those surfaces due to identical temperature results for hollow and crest surface. As always, we estimated the net heat flux with Equation 4.23 which is derived by Equation 4.12. Net heat flux for Re=4700 is illustrated in Figure 4.39;
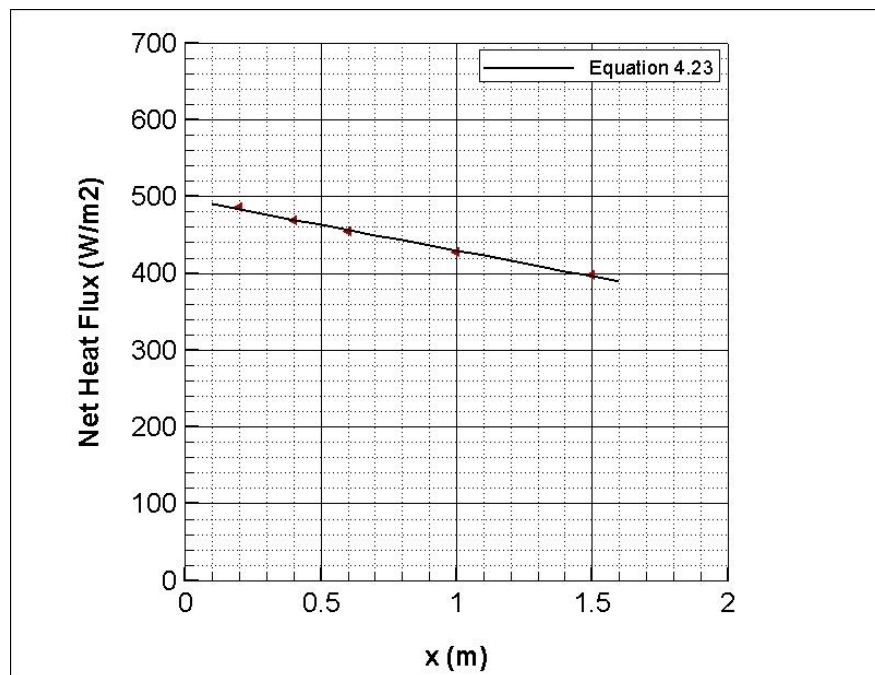

Figure 4.39. Local Heat flux at Re=4700 for corrugated pipe 34.5 mm in diameter

According to Figure 4.39, the net heat flux is a function of position over the pipe surface and falls linearly as x increases. The heat loss trend is close to one for the previous pipe tested. The data is fitted with linear approximation to derive the equation below;

$$\delta_{net}(x) = -66.9x + 496.6 \tag{4.23}$$

We estimated the local mean temperature through the corrugated pipe by deriving equations with same way at the previous section. (Equation 4.14 - 4.17)

$$T_m(x) = T_0 + \frac{\pi D_i}{m C_p}(-33.5x^2 + 496.6x) \tag{4.24}$$

Table 4.5. Local surface and mean temperature for corrugated pipe 34.5 mm in diameter

	x (m)	Surface Temperature	Mean Temperature
inlet	0	22.44	22.44
Pipe Surface	0.2	49.24	26.71
	0.4	53.64	30.86
	0.6	57.05	34.89
	1.0	63.97	42.61
	1.5	71.38	51.60
outlet	2.01	65.26	60.02

According to Table 4.5, we predict the outlet temperature with Equation 4.24 7.7 % deviating from the measured one. This is higher than deviation than the deviation for outlet temperature of corrugated pipe with 20.4 mm in diameter. We used orifice plate with diameter of 30.02 mm for the test in this section whereas; we used 20.17 mm for the other corrugated pipe. Thus, mass flow rate measured by those orifice plates might be deviating from each around 4 - 5 %.

We indicated the local wall temperature and local mean temperature to investigate if the relative temperature of each local surface temperature and mean temperature is constant in the fully developed region in the figure below.
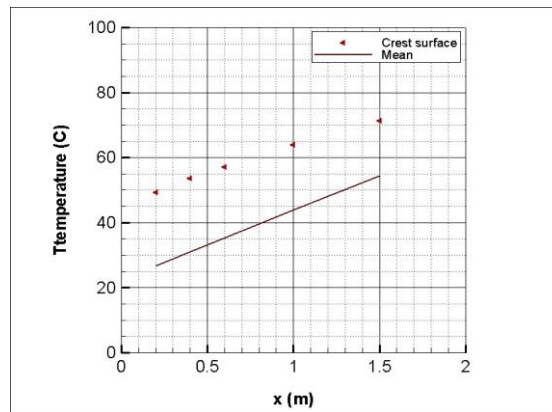
Figure 4.40. Local temperature values at Re = 4700 for corrugated pipe 34.5 mm

As appears in Figure 4.40, the fully developed region is observed to be in 1 m for Re=4700. Having said that though, the relative temperature drops as the position x is getting near the outlet of the pipe. For the test set up in this section, the heat loss is not constant for forced convection test but relative temperature is almost stable through the pipe. However, we still take the heat loss into account again due to dissipation in Figure 4.37. Therefore, we now expected the local heat transfer coefficient and local Nusselt number would remain almost the same in fully developed region.

As per Equation 4.18 and Equation 4.20 (equations previous section), we present the local heat transfer coefficient and witnessed the our prediction becoming real in Figure 4.41;

Figure 4.41. Local heat transfer coefficient at Re=4700 for corrugated pipe 34.5 mm in diameter

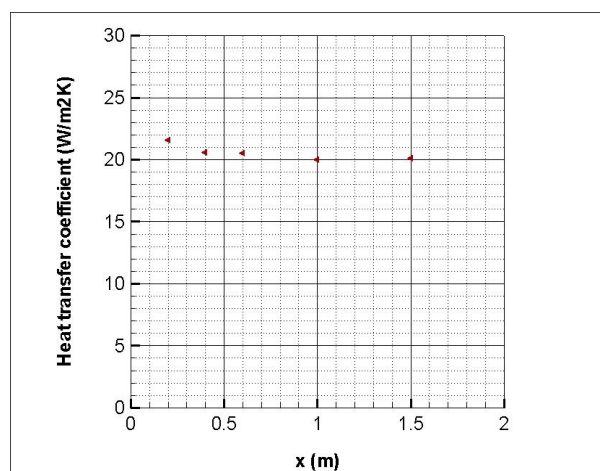According to Equation 4.20, local Nusselt number is also function of x as shown in Figure 4.42;
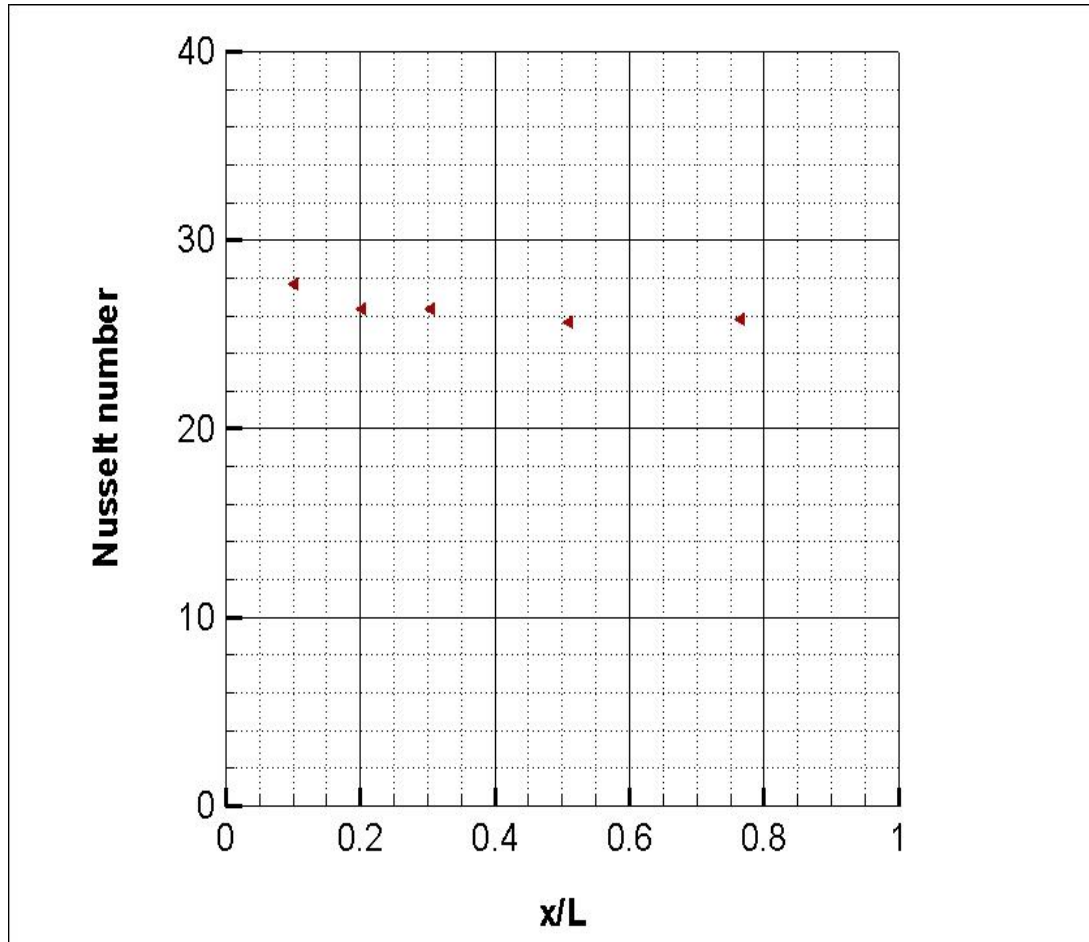
Figure 4.42. Local Nusselt number at Re=4700 for corrugated pipe 34.5 mm in diameter

Regarding Figure 4.42, Nusselt number should be around about 25. The local Nusselt number is larger close to the inlet section and falls along the corrugated pipe with diameter of 34.5 mm at Re=4700. The local Nusselt number converges to approximately 25 which is average Nusselt number when the local length is around 1 m. This indicates the fully developed region is reached nearly or just before 1 m away from inlet section of the corrugated pipe. As mentioned before, we already expected the local heat transfer coefficients thus; Nusselt numbers would be consistent due to consistency in temperature readings along the pipe for heat loss measurements and also the procedure for the placement of thermocouples. As a result, we can surely say average Nussselt number is roughly 25 at Re=4700 with a high precision of determination of local Nusselt number.

We applied the same method for the measurement of average Nusselt number for a wide variety of Reynolds number. We illustrated average Nusselt number with respect to Reynolds number in Figure 4.43.
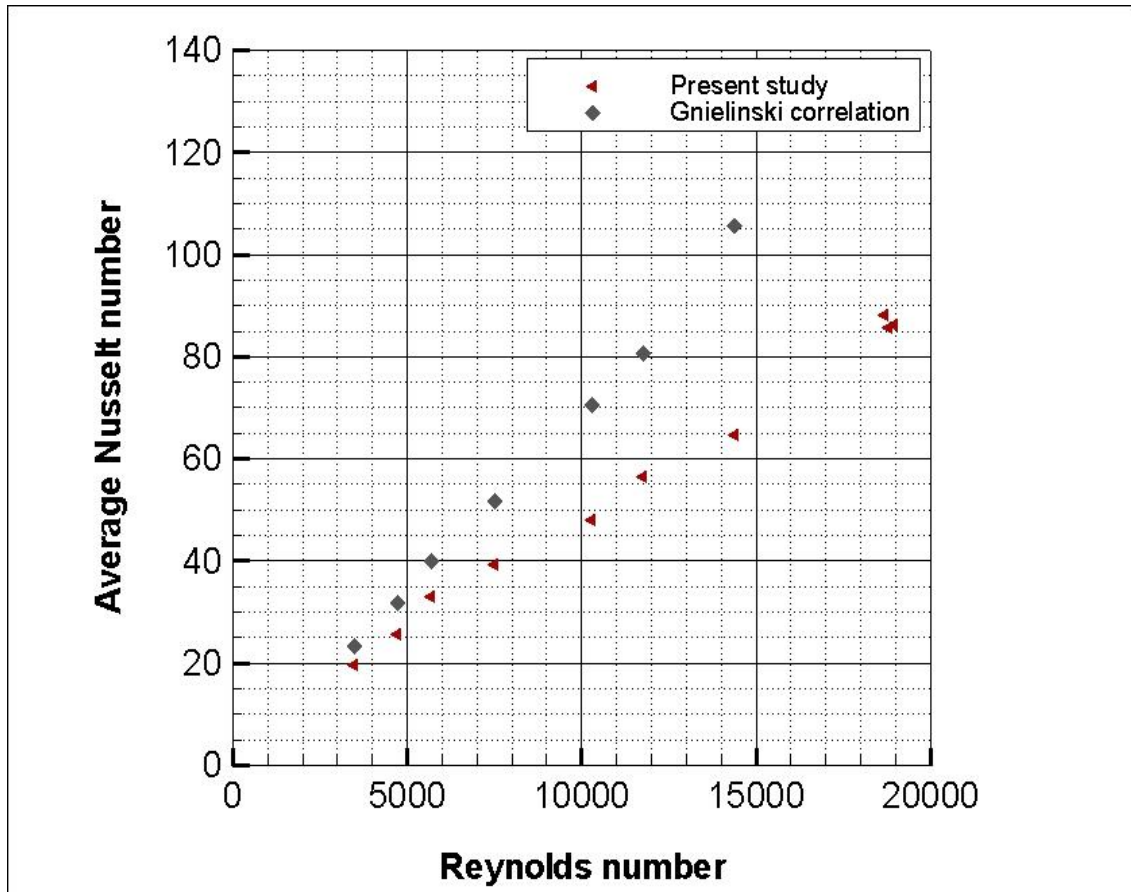
Figure 4.43. Nusselt number with respect to Reynolds number for corrugated pipe 34.5 mm in diameter

As per Gnileski's correlation, Nusselt number continues to increase steadily whereas our test results of Nusselt number seem to rise with lower slope until Reynolds number is tested around 18800 at the Nusselt number around 88.

4.5.3. Comparison of Corrugated pipes with Diameter of 20.4 mm and 34.5 mm

We compared the test results of average Nusselt number values for both pipe in Figure 4.44. We observed the average Nusselt number values are almost same with respect to Reynolds number despite their diameters and corrugation dimensions are different.
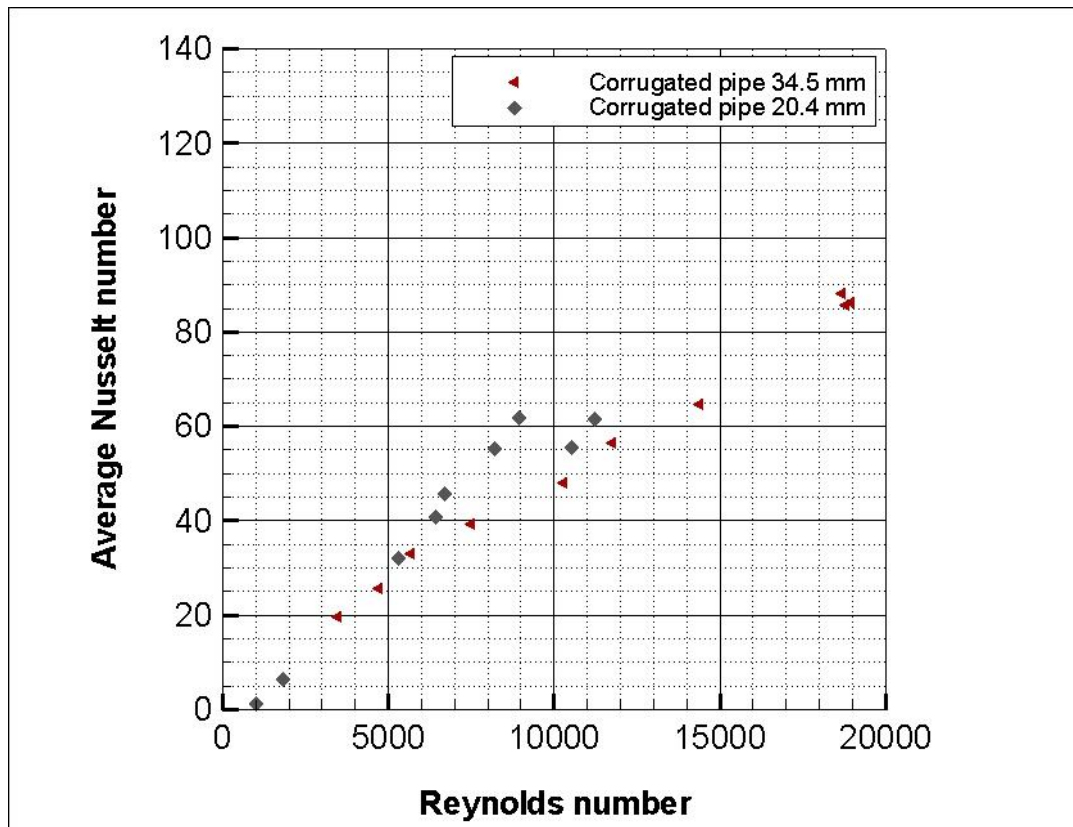
Figure 4.44. Nusselt number with respect to Reynolds number for corrugated pipe 20.4 mm and 34.5 mm in diameter

We discussed the possible error rate in hydrodynamic and acoustic test for corrugated pipes. We explained that the possible error rate includes determination of orifice diameter and discharge coefficient. However, we also have to take the thermocouple into consideration while estimating possible errors in measurements of Nusselt number. For instance, the thermocouple readings might be ± 3 °C for corrugated pipe 20.4 mm in diameter due to heat loss tests. Therefore, we estimate the total error rate is around 33 % for corrugated pipe 20.4 mm while it is roughly 15 % for corrugated pipe 34.5 mm in diameter. Experimental error of latter is less than the former because the thermocouple readings for surface temperature of the pipe 34.5 mm were much better. Due to the fact that, we noticed no decrease in surface temperature in fully developed region for the corrugated pipe 34.5 mm whereas; temperature were falling slightly in fully developed region for the pipe 20.4 mm. However, Nusselt number increases constantly while Reynolds number is escalating in turbulent region as Vicente et al [12] suggested.

5. CONCLUSION

Friction factor and acoustics for the stainless-steel corrugated pipes with different diameters and corrugation dimensions have been experimentally investigated. The critical Reynolds numbers of different corrugated pipes are found to be 1500 to 1700, depending on the pipe diameters and corrugation sizes. The critical Reynolds number becomes lower for the higher ratio of the hollow width to pipe diameter. The reason for this is that the larger hollow width causes vortices in the cavities to be less stable, and the unstable vortices in the cavities are more easily ejected to the bulk, generating disturbance in the bulk flow and prompting earlier transition from laminar to turbulent regions. Turbulent region begins at around Re = 2000 to 3000 for all corrugated pipes tested in the present experiment. For turbulent flow, in general, higher friction factors are observed as the ratio of the crest width to pipe diameter increases. It is noted that the friction factor in turbulent region is a function of W_c/D_i rather than of W_h/D_i while the critical Reynolds number is a function of W_h/D_i rather than of W_c/D_i,

The onset velocity appears to correspond to the Reynolds numbers at which turbulent region begins. Furthermore, the onset velocity is found to be independent of the pipe length.

The Strouhal number based on the crest width is observed to lie within the narrow band of 0.16 to 0.3 over the wide range of Reynolds number for all pipe sizes. More detailed observation shows that the Strouhal number does not change with the pipe length but with the corrugation sizes. On the other hand, the peak-whistling Strouhal number is found to decrease as the ratio of the diameter to the crest width increases.

The friction factor is also found to be an increasing function of the peak-whistling Strouhal number. Therefore, the corrugation geometry, friction factor and Strouhal number are found to be all closely related to one another. That is, the higher ratio of the crest width to pipe diameter, the higher peak-whistling Strouhal number, and the higher friction factor. We observe that the method of thermocouple installation is crucial in measuring temperature accurately. The average Nusselt numbers for two pipes with the diameters of

20.4 and 34.5 mm are found to be close each other though we are not certain of the results due to possible measurement errors. The Nusselt number for crest and hollow surface are almost identical for clear temperature readings due to pulsating and circulating flow.

REFERENCES

1. N. Kruse, S. Kuhn and P. R. V. Rohr. Wavy Wall Effects on Turbulence Production and Large-Scale Modes. *Journal of Turbulence*, 10.1080/14685240600602911, 2006.

2. S. Nakagawa, and T. J. Hanratty. Particle Image Velocimetry Measurements of Flow Over a Wavy Wall. *Physics of Fluids*, 10.1063/1.1399291, 2001.

3. M. Breuer, N. Peller, C. Rapp, and M. Manhart. Flow Over Periodic Hills – Numerical and Experimental Study in a Wide Range of Reynolds Numbers. *Computers and Fluids,* 2008.05.002, 2009.

4. J. D. Hudson, L. Dykhno, and T. J. Hanratty. Turbulence Production in Flow Over a Wavy Wall. *Experiments in Fluids*, 20, pp. 257-265, 1996.

5. A. E. Perry, W. H. Schofield and P. N. Joubert. Rough Wall Turbulent Boundary Layers. *Journal of Fluid Mechanics,* 10.1017/S0022112069000619, 1969.

6. L. Djenidi, F. Anselmet, and R. A Antonia. LDA Measurements in a Turbulent Boundary Layer Over a d-Type Rough Wall. *Experiments in Fluids*, 323–329, 1994.

7. J. Jiménez. Turbulent Flows Over Rough Walls. *Annual Review of Fluid Mechanics*, 2004.

8. H. Stel, R. E. M. Morales, A. T. Franco, S. L. M. Junqueira, R. H. Erthal and M. A. L. Gonçalves. Numerical and Experimental Analysis of Turbulent Flow in Corrugated Pipes. *Journal of Fluids Engineering*, 10.1115/1.4002035, 2010.

9. E. Unal, H. Ahn, E. Sorguven, and Z. Gul. Experimental Investigation of Vortex Structure in the Corrugated Channel. *International Mechanical Engineering Congress & Exposition (IMECE), 2013 ASME,* San Diego, 2013-66063.

10. E. Unal, H. Ahn, and E. Sorguven. Experimental Investigation on Flows in a Corrugated Channel, to be submitted, 2015.

11. H. Ahn and I. Uslu. Experimental Investigation on Pressure Drop in Corrugated Pipes. *International Mechanical Engineering Congress & Exposition (IMECE), 2013 ASME,* San Diego, 2013-66061.

12. P. G. Vicente, A. Garcia, and A. Viedma. Mixed Convection Heat Transfer and Isothermal Pressure Drop in Corrugated Tubes for Laminar and Transition Flow. *International Communications in Heat and Mass Transfer*, S0735-1933(04)00052-1, 2004.

13. P. R. Nyarko. Heat Load and Its Effects on Fluid Friction Factor in Corrugated Pipes. *American Journal of Scientific and Industrial Research*, 10.5251, 2153-649X, 2012.

14. M. Popescu, S. T. Johansen, and W. Shyy. Flow-Induced Acoustics in Corrugated Pipes. *Communications in Computational Physics*, 10.4208/cicp.301209.230710a, 2011

15. G. Nakiboglu, S. P. C. Belfroid, J. Golliard and A. Hirschberg. On the Whistling of Corrugated Pipes: Effect of Pipe Length and Flow Profile. *Journal of Fluid Mechanics*, 10.1017/S0022112010005884, 2011

16. G. Nakiboglu, H. B. M. Manders and A. Hirschberg. Aeroacoustic Power Generated by a Compact Axisymmetric Cavity: Prediction of Self-Sustained Oscillation and Influence of the Depth. *Journal of Fluid Mechanics*, 10.1017/jfm.2012.203, 2012

17. J. W. Elliot. Corrugated Pipe Flow. In: M. C. M Wright, editor, *Lecture Notes on Mathematics of Acoustics*, pages 207 220. Imperial College Press, London, 2005.

18. O. Rudenko, G. Nakiboğlu, A. Holten and A. Hirschberg. On whistling of pipes with a corrugated segment: Experiment and theory. *Journal of Sound and Vibration*, 332, 7226-7242, 2013

19. V. Debut, J. Antunes and M. Moreira. Experimental Study of the Flow-Excited Acoustical Lock-in in a Corrugated Pipe. *14th International Congress on Sound & Vibration (ICSV14)*, *2007,* Cairns, 2007-2473.

20. WEBTECH.http://www.webtech.buffalo.edu/student/m3_digimusic/02_documents/sound_wave/MusicInstruments_OpenEndAirColumns.htm [retrieved 15 May 2015]

21. F. M. White. *Fluid Mechanics*, McGraw Hill, 2013.

22. J. Nikuradse. Stromungsgesetze in rauhen Rohren. *Forschungsheft 361. VDI Verlag, 1933 Forschung auf dem Gebiete des Ingenieurwesens*, Berlin, (in German). (English translation: Laws of flow in rough pipes, NACA TM 1292, 1950)

23. Wikipedia, "Orifice Plate", https://en.wikipedia.org/wiki/Orifice_plate [retrieved 15 May 2015].

24. T. L. Bergman, A. S. Lavine, F. P. Incropera and D. P. Dewitt. *Fundamentals of Heat and Mass Transfer*, John Wiley & Sons, 2011.

APPENDIX A: ACQUISITION AND EVALUATION OF VORTEX SHEDDING FREQUENCY AND SOUND PRESSURE LEVEL

Algorithm A.1. Script for the recoding and evaluating

```matlab
clc
clear all

%%%%%%%SOUND RECORDING%%%%%%%%%%
fs=88200;
bits=16;
recObj = audiorecorder(fs,bits,1);
prompt='press 1 for starting...';
x=input(prompt);
if x==1
disp('Start speaking.')
recordblocking(recObj, 10);
disp('End of Recording.');
% Store data in a array.
myRecording = getaudiodata(recObj);
else
end
prompt='wav için dosya adi giriniz:';
z = input(prompt,'s');
wavwrite(myRecording,fs,bits,z);

%%%%FAST FOURRİER TRANSFORM (FFT)%%%%%%%%
pressure=myRecording(88200:end,1);
average=mean(pressure);
pressure=pressure-average;
Fs=88200;
L=size(pressure,1);
time=0:(10/(L-1)):10;
figure
plot(time,pressure);
title([int2str(i),' Standing wave pressure versus time'])
xlabel('Time')
ylabel('Standing wave pressure')
grid on
prompt='.dat dosyasi için dosya adi giriniz:';
y = input(prompt,'s');
frdata=[time.' pressure];
csvwrite(y,frdata);
prompt='.jpeg dosyasi için dosya adi giriniz:';
k=input(prompt,'s');
```

```matlab
saveas(gcf,k,'jpeg')
NFFT = 2^nextpow2(L); % Next power of 2 from length of y
Y = fft(pressure,NFFT)/L;
f = Fs/2*linspace(0,1,NFFT/2+1);
ftr=f.';
Yt=2*abs(Y(1:NFFT/2+1));
figure
plot(f,2*abs(Y(1:NFFT/2+1)),'.-b')
title([int2str(i),' Standing wave Amplitude Spectrum'])
xlabel('Frequency (Hz)')
ylabel('|Y(f)|')
xlim([0 2500])
grid on
prompt='.jpeg dosyasi için dosya adi giriniz:';
j=input(prompt,'s');
saveas(gcf,j,'jpeg')
prompt='.dat dosyasi için dosya adi giriniz:';
k = input(prompt,'s');
alldata=[Yt ftr];
csvwrite(k,alldata);

%%%%%%Display the peak whistling frequency%%%%%
[X,Y]=max(alldata);
m=alldata(Y(1),2);
fprintf('the frequency of the data set is %6.2f %12.8f\n',m)
```

Algorithm A.2. Transforming the data from Algorithm A.1 to Decibel log scale

```matlab
clear all, clc
%%%%%READING DATA%%%%%%%%%
data=input('write your folder....');
C=csvread(data); % reading main data

%%%%%%%plotting%%%%%%%%%%
Yt=C(:,1);
f=C(:,2);
db=convertdBSPL(Yt);
figure
plot(f,db,'.-b')
xlabel('Frequency (Hz)')
ylabel('Sound Pressure Level (dB SPL)')
xlim([0 2500])
ylim([-50 120])
grid on
alldata=[db f];
```

```
%%%%%%Display the peak whistling frequency%%%%%
[X,Y]=max(alldata);
m=alldata(Y(1),2);
n=alldata(Y(1));
fprintf('the frequency of the data set is %6.2f %12.8f\n',m)
fprintf(' and the power of the data set is %6.2f
%12.8f\n',n)

%%%%%%%% Save the figure %%%%%%%%%%%%%%%%
prompt='.jpeg dosyasi için dosya adi giriniz:';
j=input(prompt,'s');
saveas(gcf,j,'jpeg')
```

Algorithm A.3. Function for Decibel log scale

```
function [ dB ] = convertdBSPL( V )
%CONVERTDB2 Summary of this function goes here

mic_sens=0.2512;

dB=20*log10((V/mic_sens)/20e-6);

end
```